THE KINETICS OF INCONGRUENT REDUCTION BETWEEN SAPPHIRE AND MG-AL MELTS

A Thesis Presented to
The Academic Faculty

by

Yajun Liu

In Partial Fulfillment
of the Requirements for the Degree
Doctor in the
School of Materials Science and Engineering

Georgia Institute of Technology
May 2006

THE KINETICS OF INCONGRUENT REDUCTION BETWEEN SAPPHIRE AND MG-AL MELTS

Approved by:

Dr. Kenneth H. Sandhage, Advisor
School of Materials Science and Engineering
Georgia Institute of Technology

Dr. Robert F. Speyer
School of Materials Science and Engineering
Georgia Institute of Technology

Dr. Robert L. Snyder, Advisor
School of Materials Science and Engineering
Georgia Institute of Technology

Dr. Preet Singh
School of Materials Science and Engineering
Georgia Institute of Technology

Dr. G. Paul Neitzel
School of Mechanical Engineering
Georgia Institute of Technology

Date Approved: April 3, 2006

ACKNOWLEDGEMENTS

Over the years, I owe many people a debt of gratitude. It is beyond my words to give my sincere gratitude to these who help me directly and indirectly to the completion of this thesis.

First and foremost, I would like to express my appreciation to my thesis advisor, Dr. Kenneth H. Sandhage and Dr. Robert L. Snyder, for providing kind help, intellectual support and excellent guidance during my graduate studies and thesis research. Without their advice, I would not have achieved what I have.

Besides my advisors, I would like to express my sincere thanks and respect to other members of my thesis committee, Dr. Robert F. Speyer, Dr. Joe K. Cochran, and Dr. G. Paul Neitzel, for providing invaluable assistance in their own areas of expertise.

In addition, I would also like to thank all the students in Dr. Sandhage's research group. I especially acknowledge Dr. Ye Cai for the TEM characterization of my samples, and Dr. Yunshu Zhang for his valuable comments on the first draft of this thesis. This research would not have been possible without the help from Yolande Berta for SEM and Dr. W. Brent Carter for XPS.

Finally, I would like to thank my parents for their great support and understanding during my graduate studies.

TABLE OF CONTENTS

LIST OF TABLES

LIST OF FIGURES

LIST OF SYMBOLS

Va	vacancy
I	nucleation rate
v	growth rate of a particle
X_e	the volue fraction that has transformed after time t
X	transformed volume fraction
N_0	nucleation site per unit volume at the beginning
υ	the rate at which an individual site becomes a nucleus
n	Avrami exponent constant
k_A	temperature-dependent factor
λ	positive impingement factor
η	exponent factor defined as $1/(\lambda - 1)$
n_s	parameter akin to the Avrami exponent
$\tilde{D}$	interdiffusion coefficient
x	compound layer thickness
k_{diff}	diffusion constant
k_{reac}	reaction constant
Q	activation energy
k_0	frequency constant
$C_{Al}^{spinel-MgO}$	the Al concentration in spinel at the $MgAl_2O_4$-MgO interface
$\Delta C_{Al}^{spinel} / \Delta x$	the slope of composional profile of Al in spinel
D_{eff}	effect diffusion coefficient

D_l	diffusion coefficient in lattice
D_b	diffusion coefficient along grain boundary
δ_b	width of grain boundary
ω	grain size
k	parabolic constant
R	gas constant
T	absolute temperature
t	time
$\dot{R}$	dissolution rate of a compound
C_s	saturation concentration
ν	kinematical viscosity
g	gravitational acceleration constant
ρ_0	initial melt density
$\Delta\rho$	melt density change upon reaction
J	flux
C	volume concentration
δ	boundary layer thickness
y	spatial variable defined as a distance from a sample top
p	number of sites on the cation sublattice in the ionic liquid model
q	number of sites on the anion sublattice in the ionic liquid model
k_w	parabolic constant obtained from weight change measurement
ΔW	sample weight change
n_{total}	molar amount of oxygen-controlled alloys used for each run

$n_{MgAl_2O_4}$ molar amount of dissolved $MgAl_2O_4$

x_O oxygen molar fraction in the Mg-Al melt equilibrated with MgO and $MgAl_2O_4$ at the incongruent reaction temperature

x_O^* oxygen molar fraction in the oxygen-controlled alloy

$W_{Al_2O_3}$ molecular weight of $MgAl_2O_4$

$\rho_{MgAl_2O_4}$ $MgAl_2O_4$ density

l length of a sapphire wafer

w width of a sapphire wafer

h thickness change of a reacted sample caused by dissolution

$\vec{u}$ velocity vector of fluid

c Mg molar fraction in the melt

ρ melt density

V_m molar volume of Mg-Al melts

x_{Mg} Mg molar fraction

μ_{Al} viscosity of the Mg-Al melt

D diffusion coefficient of Mg in the Mg-Al melt

D_{ij} diffusion tensor

J_{Mg}^{spinel} Mg flux in spinel

$J_{Mg}^{sapphire}$ Mg flux in sapphire

$\dot{x}$ growth rate of spinel

C_{Mg}^2 the Mg concentration of spinel at the $MgAl_2O_4$-Al_2O_3 interface

C_{Mg}^3 the Mg concentration of sapphire at the $MgAl_2O_4$-Al_2O_3 interface

SUMMARY

The kinetics of incongruent reduction between sapphire and oxygen-controlled Mg-Al melts were studied by measuring spinel-layer thickness, sample-weight change and sample-thickness change as a function of time at various temperatures.

To eliminate the crucible contamination caused by impurities in commercial MgO crucibles, high-purity MgO crucibles were synthesized by gelcasting, which is an attractive ceramic-forming technique for preparing high-purity ceramic parts. The oxygen-controlled alloys were obtained by the three-phase-equilibrium experiments at various temperatures. To avoid MgO formation, the oxygen-controlled alloys prepared at lower temperatures were used for incongruent reaction experiments at higher temperatures. That is to say, the oxygen-controlled alloys prepared at 900°C, 1000°C, and 1100°C were used for spinel formation experiments at 1000°C, 1100°C, and 1200°C, respectively.

The experiments were conducted in a vertical furnace, and sapphire wafers were hung vertically in high-purity MgO crucibles so that the natural convection induced by the density change in the melt could be investigated. Experimental results obtained at 1000°C, 1100°C, and 1200°C revealed that the spinel layer thickness on two orientations of sapphire wafers, namely $\{0001\}$ and $\{01\bar{1}2\}$, followed orientation-independent parabolic kinetics, indicating the diffusion in spinel was one of the rate-limiting steps. In addition, the spinel layer thickness was not a function of position. The results of sample-thickness-change measurements also indicated that the effect of natural convection could be neglected. XPS, XRD, and TEM were also employed to characterize some samples in

this study. Based on a simple model where the diffusion in spinel was the only rate-limiting step, the governing partial differential equations for diffusion and fluid dynamics were solved by the finite element method. The calculated theoretical parabolic constants at various temperatures were compared with these experimental results, and a good agreement was obtained.

Some preliminary studies were also made on the morphologies of spinel particles at the nucleation stage. It was found that the triangular {111} faces of spinel particles were parallel to the surface of {0001} sapphire substrate. The product shape was consistent with a tetrahedron composed of {111} faces. The morphology of spinel particles on a $\{01\bar{1}2\}$ sapphire substrate was more complicated in that the triangular {111} faces of spinel had to be inclined at a certain angle to the substrate in order to maintain the orientation relationship.

CHAPTER I

INTRODUCTION

A solid oxide may experience a chemical reaction and thereby yield a fluid product and a new solid product with different compositions. This kind of reaction is termed as an incongruent reaction [1]. Three general kinds of incongruent reactions have been discussed in the literature:

- Incongruent vaporization

  Incongruent vaporization refers to the case where a new solid forms on the surface of a liquid that is undergoing reactive evaporation [2-4].

  Example: the conversion of solid Co into $CoCl_2$ in an O_2-Cl_2-Ar atmosphere with the formation of CoO as a product phase at the Co-gas interface.

- Incongruent dissolution

  Incongruent dissolution is defined by the formation of a new solid on the surface of a solid that is dissolving into a liquid [5-6].

  Example: the dissolution of solid Al_2O_3 into MgO-bearing silicate melts with the formation of $MgAl_2O_4$ at the Al_2O_3-melt interface [7].

- Incongruent reduction

  A displacement reaction between a solid oxide and a molten metal is considered to be incongruent if a new solid oxide with different composition forms at the solid-liquid interface.

  Example: The reduction of Al_2O_3 in a Mg-Al melt with the formation of $MgAl_2O_4$ at the Al_2O_3-melt interface.

Ceramic-metal composites can exhibit desirable combinations of high specific modulus, high toughness, thermal stability and good heat-resistance needed for a wide range of potential applications [8-10]. However, their commercial uses are limited so far in part because of the high cost. Furthermore, for some applications, the ceramic content still remains at a relatively low level.

In order to overcome these difficulties, several incongruent reduction based methods, such as Co-Continuous Ceramic Composite (C^4) [11], Reactive Metal Penetration (RMP) [12] and Displacive Compensation of Porosity (DCP) [13-15], have recently been developed to produce near net-shape composites with tailored microstructure and unique properties. Unlike the other methods, the DCP method involves the use of a volume-increasing effect induced by incongruent reduction. For example, molten Mg was allowed to infiltrate and react with shaped porous Al_2O_3 preforms to produce MgO. Because the volume of 3 moles of MgO is 31% larger than the volume of 1 mole of Al_2O_3, MgO/Mg-Al composites with MgO contents as high as 86% were produced [16].

In addition, incongruent reduction has also been demonstrated as an effective low-temperature route for the syntheses of metal-ceramic composites for high temperature applications. One of its advantages is that the handling of liquids of heavy metals, which do not have good infiltration ability at relatively low temperatures, can be avoided [17]. For example, a porous WC preform was infiltrated and reacted with Zr_2Cu liquid incongruently at 1300°C to yield solid ZrC and W. Because Cu has nearly no chemical reaction with ZrC, W or WC, and therefore it can be extruded back into the bulk liquid during the reaction, dense ZrC/W composites with little residual Cu were

successfully produced by DCP [18-19].

Although the kinetics and mechanisms for incongruent dissolution and incongruent vaporization have been well investigated, such information for incongruent reduction is still rare in the literature. Therefore, the application of incongruent reduction in composite fabrication has still been hampered by the lack of relevant kinetic data, which are needed to predict how the processing parameters will affect the composite microstructure, and consequently the composite properties.

A fundamental understanding of the kinetics of incongruent reduction and microstructure evolution can aid the design and development of attractive composites. Information on the rate-limiting steps will be of great significance in predicting microstructure evolution and tailoring mechanical properties.

In this work, the fundamental kinetics and mechanisms of incongruent reduction between sapphire and Mg-Al melts have been investigated. This reaction system is particularly attractive for study because:

- The excess Gibbs free energy of mixing of Mg-Al melts has been extensively determined by many investigators, and all these data show slightly negative deviations from ideal behavior.
- The solid-state diffusion process in spinel has already been determined. Oxygen is nearly immobile in the spinel formation process. As a consequence, Mg^{2+} and Al^{3+} diffuse in opposite directions to retain the state of electroneutrality.
- The Mg-Al-O ternary system contains only two binary oxides (MgO and Al_2O_3) and one ternary oxide ($MgAl_2O_4$) at ambient pressure. Mg-Al melts can react with Al_2O_3 incongruently to form MgO and $MgAl_2O_4$, depending on the Mg

concentration and temperature. By tailoring the composition and temperature properly, the spinel can be the only phase formed. In this way, the process of incongruent reduction can be carefully investigated.

- The transformation mechanism from sapphire to the spinel has been addressed by several authors, and the atomic structures of spinel-sapphire interfaces have been well studied. The spinel has been reported to form epitaxially on sapphire with the alignment of close-packed planes and close-packed directions of spinel and sapphire.

As a good understanding of the rate-limiting steps and the process of incongruent reduction of an oxide is needed, the objective of this research was to investigate the rate-limiting steps and the microstructure evolution upon incongruent reduction of Al_2O_3 by Mg-Al melts at high temperatures. This work was focused mainly on the investigation of the rate-limiting steps for the case where a continuous $MgAl_2O_4$ layer is formed on sapphire, though some experiments were also conducted to evaluate the early stages of spinel nucleation and growth. More specifically, the technical objectives were:

- To determine the rate-limiting steps for the steady-state incongruent reduction between Mg-Al melts and sapphire.
- To investigate how the following key parameters influence the reaction kinetics
  - Temperature
  - Mg concentration in Mg-Al melts
  - Sapphire orientation
  - Natural convection in Mg-Al melts

CHAPTER II

BACKGROUND

2.1 Crystallography

2.1.1 The Crystal Structure of $MgAl_2O_4$

Spinels form a large class of inorganic crystals with the general formula AB_2O_4. There are two factors that determine the combinations of atoms to form a spinel-type structure: the total cation charge and the relative cation sizes. There are eight negative charges to be balanced for the AB_2O_4 structure, which can be achieved by the following three combinations of cation charges: (A^{2+}+$2B^{3+}$), (A^{4+}+$2B^{2+}$) and (A^{6+}+$2B^{+}$) [20]. These three kinds are sometimes referred to as 2-3, 4-2 and 6-1 spinels, respectively. The 2-3 spinels are by far the most common and account for 80 percent of the known cases, among which $MgAl_2O_4$ has been extensively investigated. Crystals that belong to 4-2 spinels include $TiMg_2O_4$ and $PbFe_2O_4$. The least common charge combination is 6-1, and $MoNa_2O_4$ is an example for this category.

$MgAl_2O_4$ possesses the space group $Fd\bar{3}m$ [21]. Its unit cell contains 32 oxygen ions in an almost perfect cubic close-packed array, corresponding to the formula $Mg_8Al_{16}O_{32}$. In the normal spinel structure, the eight Mg ions occupy the tetrahedral sites in the face-centered-cubic oxide lattice and the sixteen Al ions occupy the octahedral sites. The structure of $MgAl_2O_4$ can be considered as octants of alternating MgO_4 tetrahedra and Al_4O_4 cubes as shown in Fig. 2.1. The four O in each MgO_4 tetrahedron and Al_4O_4 cube have the same orientation in all the eight octants, constructing a face-centered cubic lattice

with 32 oxygen ions which coordinate Mg tetrahedrally and Al octahedrally. The A-type octants shown in Fig. 2.1 contain four Mg ions, and the B-type octants contain sixteen Al ions. The stacking symbol for the {111} planes can be written as [22]:

$$...A\gamma Bc\alpha bC\beta Ab\gamma aB\alpha C\alpha\beta cA\gamma B...$$

where the capital letters represent the complete close-packed oxygen layers, the small Latin letters indicate the tetrahedral ions, and the Greek letters denote the octahedral ones. A view of the crystal structure perpendicular to the {111} closed-packed planes is presented in Fig. 2.2, where the octahedral cations are in yellow and green, and the tetrahedral cations are in purple.

In the inverse spinel structure, half of the Al cations occupy the tetrahedral sites while the other half of the Al cations and all the Mg cations are distributed on the octahedral sites. In fact, the normal and inverse spinels are limiting cases, while various degrees of inversion are commonly observed.

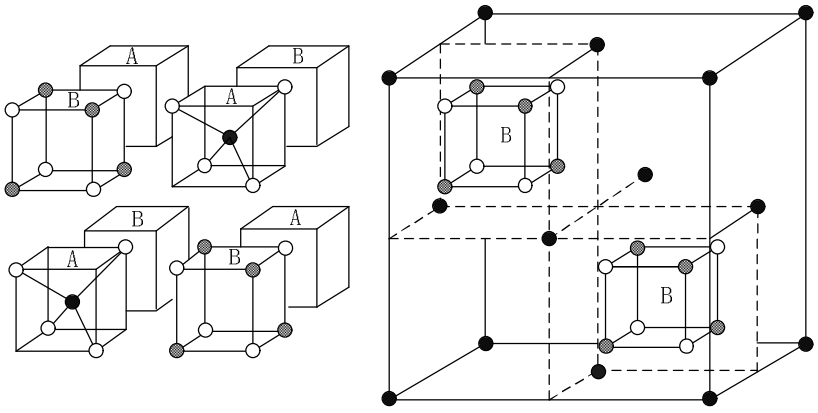

Fig. 2.1 The crystal structure of $MgAl_2O_4$

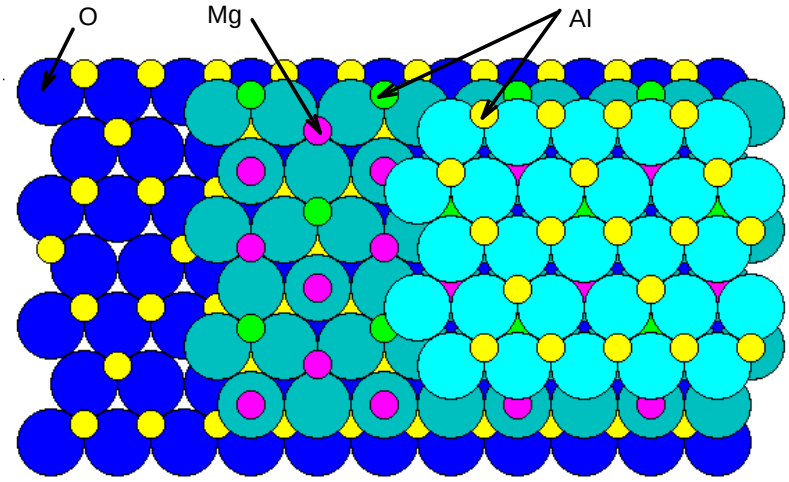

Fig. 2.2 A view of the $MgAl_2O_4$ crystal structure perpendicular to the {111} plane

2.1.2 The Crystal Structure of Sapphire

Sapphire possesses the space group $R\bar{3}c$ and has a large unit cell with the oxygen ions in a hexagonal closed-packed arrangement and aluminum ions occupying the octahedral sites. As the formula is Al_2O_3, only two-thirds of these sites are filled. The structure can be easily described by locating the octahedral sites that are not occupied by the aluminum ions, as shown in Fig. 2.3.

If all the atomic positions are projected onto the (0001) of the hexagonal unit cell, the stacking sequence of sapphire structure can be written as [23]:

$$...A\gamma_1 B\gamma_2 A\gamma_3 B\gamma_1 A\gamma_2 B\gamma_3 A\gamma_1...$$

where the capital letters denote the oxygen ion positions, and the Greek letters represent the positions of missing aluminum ions.

The hexagonal unit cell is six oxygen layers high, and contains six formula units of Al_2O_3. The crystal structure of sapphire can also be described as rhombohedra structure, which contains two formula units of Al_2O_3.

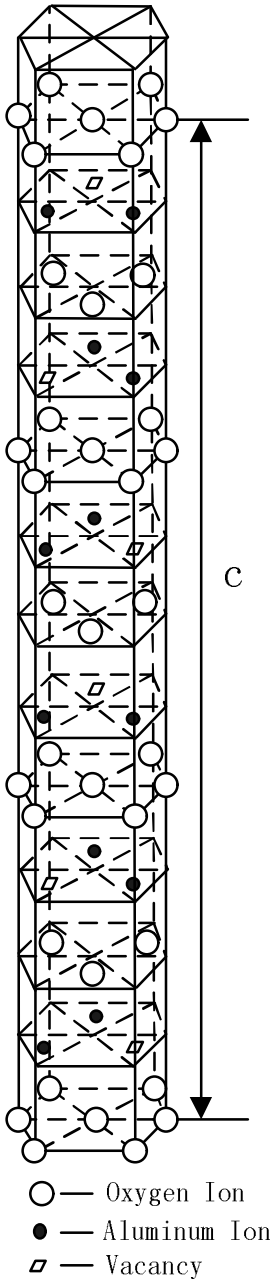

Fig. 2.3 The crystal structure of sapphire

2.1.3 The Atomistic Mechanism of Spinel Formation

Spinels are formed by the counter-diffusion of cations in the fixed oxygen sublattice. In order to maintain electroneutrality, two kinds of cations diffuse in opposite directions at a fixed ratio. This mechanism was proposed by C. Wagner and then verified by several authors [24-27]. When spinel grows on sapphire, there usually exist several preferred orientations, among which the most common situation is [28-29]:

$$\{0001\}_{sapphire} // \{111\}_{spinel}$$

$$<10\bar{1}0>_{sapphire} // <1\bar{1}0>_{spinel}$$

Or alternately,

$$\{10\bar{1}0\}_{sapphire} // \{110\}_{spinel}$$

$$<0001>_{sapphire} // <1\bar{1}1>_{spinel}$$

The atomistic configuration of the reaction front can exert a significant influence on the reaction provided that the kinetics is interface-reaction controlled. Spinel has an oxygen sublattice with an fcc structure, and sapphire possesses an oxygen sublattice with the hcp structure. As a consequence, the growth mechanism of spinel into sapphire across the interface involves not only changing the stacking sequence of the oxygen close-packed planes from ABABAB to ABCABC, but also redistribution of cations. The schematic drawing to illustrate such a process is presented in Fig. 2.4.

As the diffusion of oxygen ions is quite slow compared with that of cations, and the growth of spinel into alumina typically maintains the close-packed planes and the close-packed directions of both phases, the transformation must be governed by a certain mechanism other than simple diffusion.

Two different mechanisms have been proposed to explain the spinel growth on

sapphire, one of which is associated with the movement of Shockley partial dislocations, while the other relies on the ledges of phase boundaries.

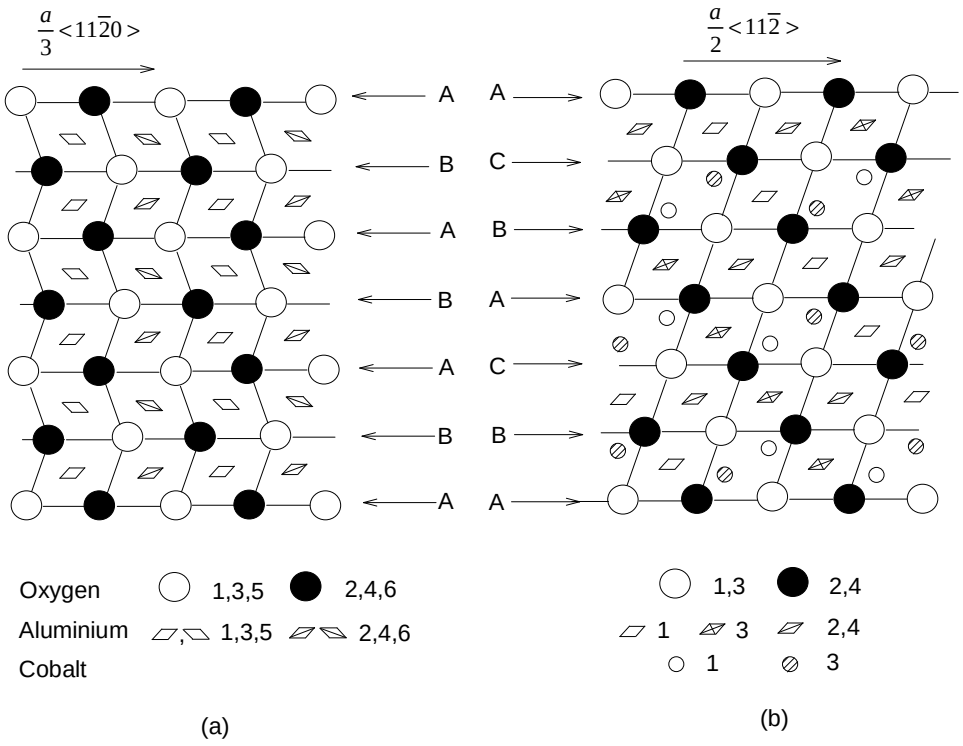

Fig. 2.4 A schematic plot to illustrate the crystal structure change before and after reaction

2.1.3.1 The Model Associated with Shockley Partial Dislocations

This model assumes that a single partial dislocation moves on alternate planes of sapphire and all the shear is in the same direction [28-29], which quickly leads to shear stress in the system. However, it can be released by the same motion of partial dislocations with opposite Burgers vector. One possible case to eliminate the shear stress is shown in Fig. 2.5, which makes bundles of Shockley partial dislocations produce no overall shear and no overall Burgers vector in the material. These Shockley partial dislocations mentioned above correspond to a/6<112> partial dislocations in spinel or a/3<10$\bar{1}$0> partial dislocations in sapphire.

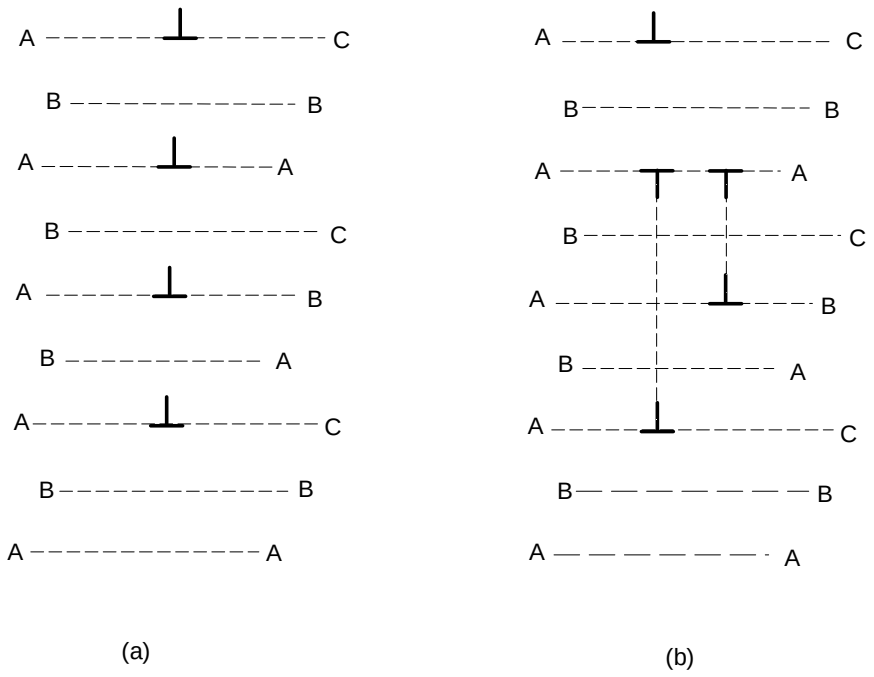

Fig. 2.5 The Shockley partial dislocation model

Although this model can be used to explain the transformation of anions, Shockley partial dislocations are rarely observed in sapphire. In addition, there are no direct observations in the literature which can provide any proof of this transformation mechanism [29].

2.1.3.2 The Model Associated with Interface Ledge

The schematic drawing for the situation where a rotation exactly accommodates the misfit at the interface is presented in Fig. 2.6. This model removes the necessity of partial dislocations to shear the oxygen sublattice.

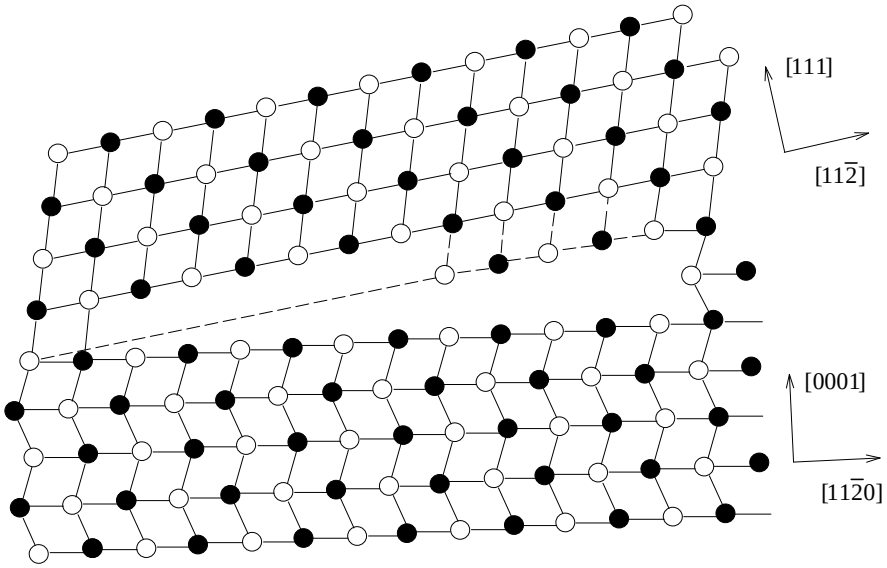

Fig. 2.6 The interface ledge model

C. Carter [29] observed that the growth of $CoAl_2O_4$ into (0001) sapphire wafers did not result in the exact parallel relationship which was often assumed to occur between {111} and {0001} planes. The experimental result was that the close-packed plane of spinel was usually rotated about an axis close to the close-packed direction <110> with respect to the (0001) plane of sapphire at an angle from 0 to 5.05°.

Y. Kouh [30] studied the formation of $NiAl_2O_4$ spinel between NiO vapor and sapphire substrates at 1400°C. It was found there was an 8° rotation between the {111} plane of spinel and the (0001) plane of alumina.

The great benefit of this small rotation is that the movement of the steps along the interface between sapphire and spinel accomplishes the phase transformation without the need of Shockley partial dislocations. Therefore, it is proposed that spinel formation occurs by the movement of ledges or steps which lead to a relative rotation of the closed-packed planes. D. Li [31] pointed out that if spinel formation did proceed by the ledge mechanism, the ledge would have a dislocation character with the same Burgers vector as a/6<112> partial dislocations which were difficult to find in spinel crystals.

2.2 Thermodynamics

2.2.1 The Mg-O Binary System

The Mg-O phase diagram was recently calculated by B. Hallstedt [32] based on the available literature data, and a set of parameters describing the Gibbs energies of individual phases were obtained. Apart from the data for pure Mg, MgO and O, there are no experimental data for other phases or for the solubility of O in liquid Mg. However, using K. Fitzner's [33] correlation method between the enthalpy and entropy of the dissolution of O in liquid metals, B. Hallstedt was able to derive the O solubility in Mg-O melts as a function of temperature. These data were then used to construct the Mg-O binary phase diagram.

The liquid phase was treated with the ionic liquid model developed by M. Hillert [34]. In this model, it is assumed that cations and anions form two different sublattices. In order to describe the metallic liquids, vacancies may be introduced on the anionic sublattice. Accordingly, the model can be written in the following simple form:

$$(Mg^{2+})_2(O^{2-},Va^{2-})_2$$

where liquid Mg is represented by the case where there are only vacancies on the second sublattice and the liquid MgO where there exist only oxygen anions.

The Gibbs energy of the liquid phase is given by:

$$G_m = y_{Va^{2-}} \cdot G^0_{Mg_2Va_2} + y_{O^{2-}} \cdot G^0_{Mg_2O_2} + 2RT(y_{Va^{2-}} \ln y_{Va^{2-}} + y_{O^{2-}} \ln y_{O^{2-}}) + y_{Va^{2-}} \cdot y_{O^{2-}} L_{Mg^{2+}:O^{2-},Va^{2-}} \quad (2\text{-}1)$$

where y_i is the site fraction of species i on the cationic or anionic sublattice, $G^0_{Mg_2Va_2}$ is the Gibbs energy of two moles of liquid Mg, $G^0_{Mg_2O_2}$ is the Gibbs energy of two moles of

liquid MgO, R is the gas constant, T is temperature, and $L_{Mg^{2+}:O^{2-},Va^{2-}}$ is the interaction parameters for the liquid phase. The thermodynamic parameters for the liquid phase are listed in Table 2.1, and the calculated Mg-O binary phase diagram is presented in Fig. 2.7.

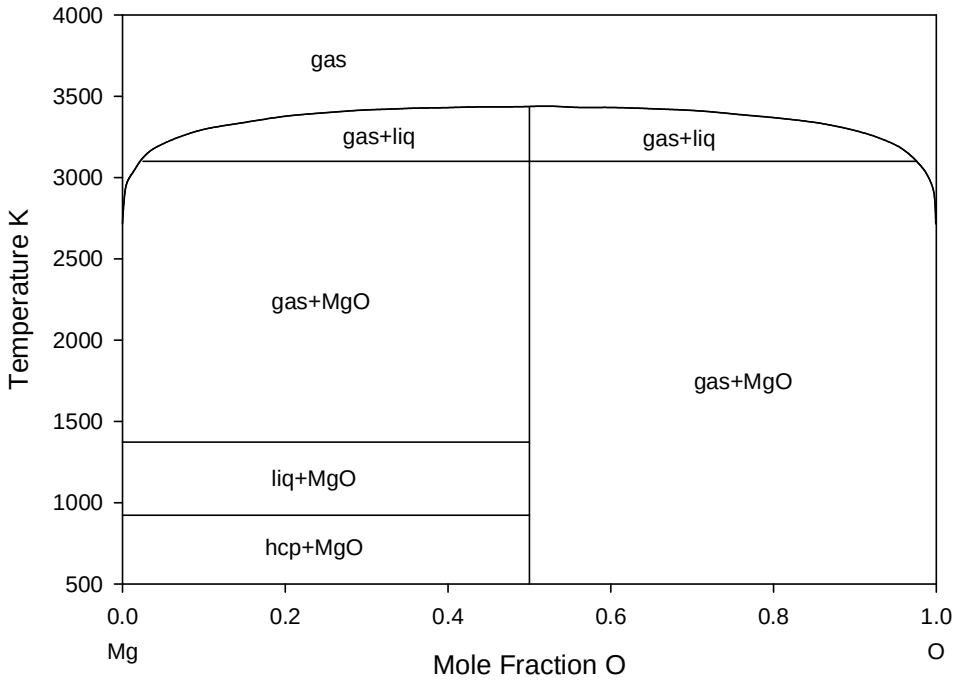

Fig. 2.7 The Mg-O binary phase diagram [32]

Table 2.1 Thermodynamic parameters for the liquid phase in Mg-O binary system [32]

GLIQMGO=
(298.15<T<1700)
-549098.33+275.72463T-47.4817Tln(T)-0.00232681T^2+4.5043E-8T^3+516900T^(-1)
GLIQMG=
(923<T<3000)
-5439.869+195.324057T-34.3088Tln(T)
$G^0_{Mg_1Va_1} = 2\text{GLIQMG}$
$G^0_{Mg_2O_2} = 2\text{GLIQMGO}$
$L_{Mg^{2+}:O^{2-},Va} = 182000 + 26.8 \cdot T$

2.2.2 The Al-O Binary System

The Al-O binary system was calculated by J. Taylor [35] to derive a set of thermodynamic data to represent all the known experimental values. In the literature, there are almost no experimental data for the solubility of oxygen in liquid Al. Based on the solubility of O in liquid Al summarized by M. Hansen [36] and the estimation method suggested by S. Ostuka [37], J. Taylor calculated the solubility of oxygen. These data were then used to construct the Al-O binary system.

The liquid phase is treated with the ionic liquid model which assumes the existence of two sublattices with aluminum cations on one and oxygen anions and vacancies on the other. If the compositions richer in oxygen than Al_2O_3 are ignored, the liquid may be conventionally represented as:

$$(Al^{3+})_2(O^{2-},Va^{3-})_3$$

The Gibbs energy of the liquid phase is thus given by:

$$G_m = y_{Va^{3-}} \cdot G^0_{Al_2Va_3} + y_{O^{2-}} \cdot G^0_{Al_2O_3} + 3RT(y_{Va^{3-}} \ln y_{Va^{3-}} + y_{O^{2-}} \ln y_{O^{2-}}) + y_{Va^{3-}} \cdot y_{O^{2-}} L_{Al^{3+}:O^{2-},Va^{3-}} \quad (2\text{-}2)$$

where y_i is the site fraction of species i on the anionic sublattice, $G^0_{Al_2Va_3}$ is the Gibbs energy of two moles of liquid Al, $G^0_{Al_2O_3}$ is the Gibbs energy of one mole of liquid Al_2O_3, R is the gas constant, T is temperature, and $L_{Al^{3+}:O^{2-},Va^{3-}}$ is the interaction parameter between oxygen ions and vacancies. All the data necessary to describe the liquid phase are listed in Table 2.2, and the calculated Al-O binary phase diagram is presented in Fig. 2.8.

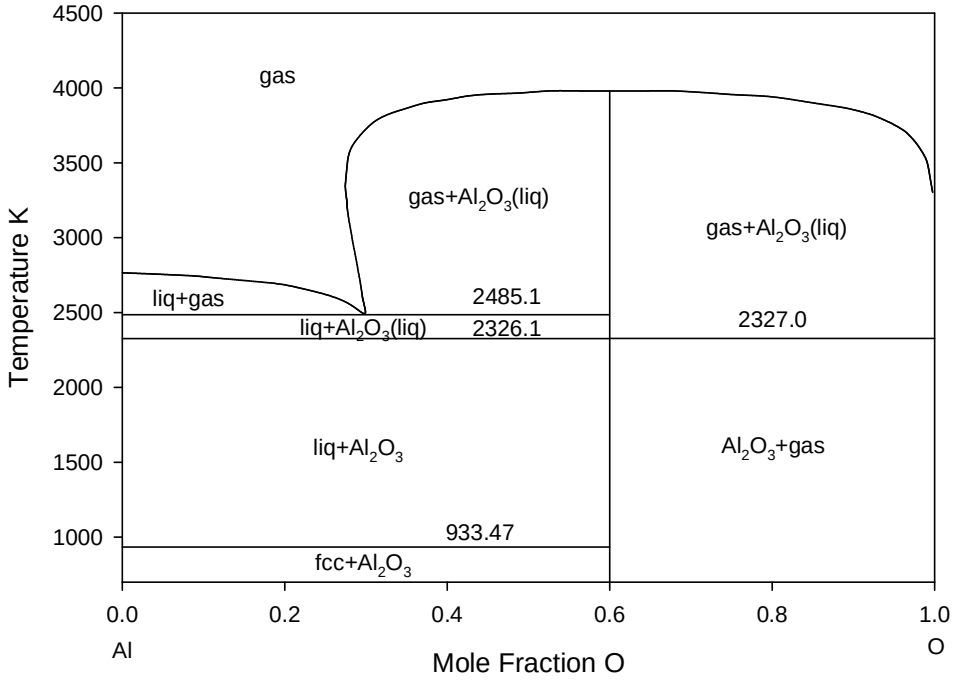

Fig. 2.8 The Al-O binary phase diagram [35]

Table 2.2 Thermodynamic parameters for the liquid phase in Al-O binary system [35]

GLIQAL2O3=

(600<T<15000)

-1625385.57+712.394972*T-116.258Tln(T)-.0072257T^2+2.78532E-07T^3+2120700T^(-1)

GLIQAL=

(933.47<T<2900)

-795.996+177.430178T-31.748192Tln(T)

$G^0_{Al_2Va_3} = 2\text{GLIQAL}$

$G^0_{Al_2Va_3} = 2\text{GLIQAL2O3}$

$L_{Al^{3+}:O^{2-},Va^{3-}} = 171042 + 106 \cdot T$

2.2.3 The Al-Mg Binary System

The Al-Mg system is of particular importance to the aluminum industry, and has been the subject of extensive studies. The Gibbs energy of the liquid phase is usually treated with a substitutional solution model which can be described by the following equitation:

$$G_m = x_{Al}G^0_{Al} + x_{Mg}G^0_{Mg} + RT(x_{Al}\ln x_{Al} + x_{Mg}\ln x_{Mg}) + x_{Al}x_{Mg}\sum_{i=0}^{n} L^i_{Al,Mg}\cdot(x_{Al} - x_{Mg})^i \quad (2\text{-}3)$$

where G^0_{Al} and G^0_{Mg} are the Gibbs energy of the two components, R is the gas constant, T is the absolute temperature, x_{Al} and x_{Mg} are the mole fractions of the two components, and $L^i_{Al,Mg}$ is the interaction parameters which are linear functions of temperature.

J. Murray [38] reviewed the thermodynamics and phase equilibrium of the Al-Mg system available in the literature. In his work, the liquid phase was treated as a substitutional solution model. The parameters for the excess Gibbs free energy of the liquid phase described by the Redlich-Kister polynomial are listed in Table 2.3.

D. Ludecke [39] reviewed the available experimental information and derived a set of thermodynamic parameters to construct the Al-Mg binary phase. The excess Gibbs free energy of the liquid phase was described by the Redlich-Kister polynomial, and the interaction parameters are listed in Table 2.3.

N. Saunders [40] reviewed the Al-Mg binary system based on the experimental data for this system. A comparison between the calculated and measured enthalpy of mixing and activity in the liquid phase was made. The liquid phase was treated with the

substitutional model, and the results for the interaction parameters are listed in Table 2.3.

Y. Zuo [41] presented a thermodynamic description for various phases in the Al-Mg binary system by an optimization of the thermodynamic and phase equilibrium data in the literature. The calculated phase diagram of the Al-Mg using these thermodynamic descriptions was in excellent agreement with experimental phase equilibrium data. The interaction parameters provided by Y. Zuo are also included in Table 2.3.

Z. Moser [42] realized that extensive thermodynamic data were available in the literature for the Mg-Al melts and all these data showed small negative deviations from the ideal behavior, but the absolute values from different techniques were not in good agreement. Accordingly, only small heat effects were obtained in calorimetric studies, and the measurements were less accurate. Z. Moser's work was to determine thermodynamic data further for the liquid phase and to optimize the Al-Mg binary phase diagram using his results and the selected information from various references. Experimental studies of the Mg-Al melts were performed by four methods, including Galvanic Cell with liquid electrolytes, Galvanic cells with solid electrolytes, vapor pressure studies and calorimetric measurements. The mutual consistency of these four sets of data was analyzed. These results and some selected thermodynamic information from the literature [43-45] were optimized to describe the liquid phase with the Redlich-Kister equations. The final results provided by Z. Moser are given in Table 2.3.

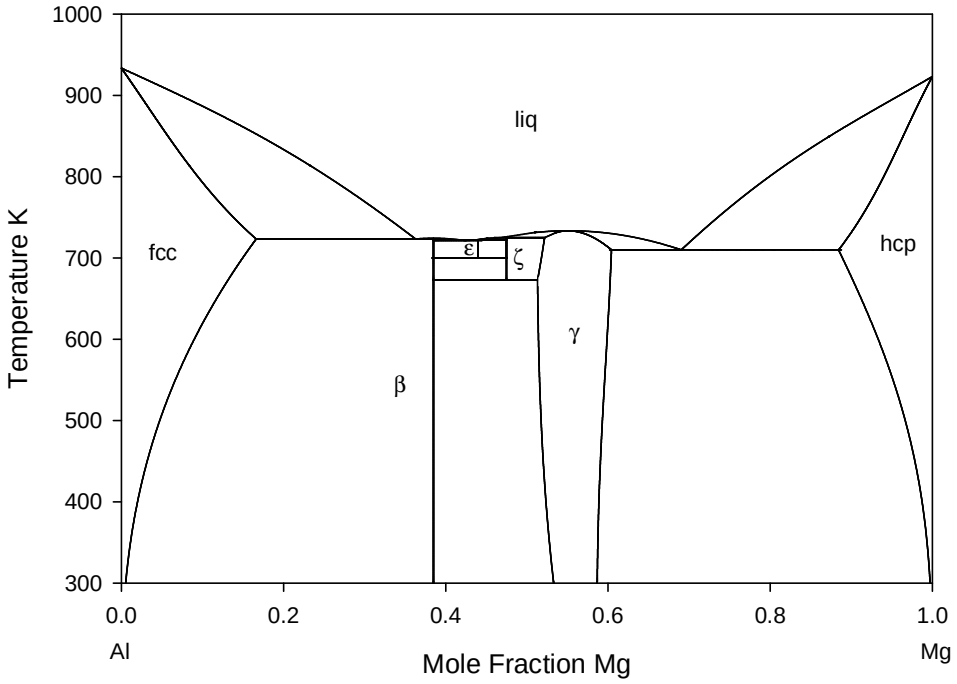

Fig. 2.9 The Al-Mg binary phase diagram [42]

Table 2.3 Thermodynamic parameters for the liquid phase in Al-Mg binary system

Interaction Parameters	Reference
$L^0_{Al,Mg} = -9500 + 6.210 \cdot T$	J. Murry [38]
$L^1_{Al,Mg} = 187$	
$L^0_{Al,Mg} = \text{-}10243.4 + 4.9446 \cdot T$	D. Ludecke [39]
$L^1_{Al,Mg} = 7328.6\text{-}9.0146 \cdot T$	
$L^2_{Al,Mg} = 2412.2\text{-}0.251 \cdot T$	
$L^0_{Al,Mg} = -12000 + 8.566 \cdot T$	N. Saunders [40]
$L^1_{Al,Mg} = 1894 - 3 \cdot T$	
$L^2_{Al,Mg} = 2000$	
$L^0_{Al,Mg} = -11200 + 9.578 \cdot T$	Y. Zuo [41]
$L^0_{Al,Mg} = -12002.58 + 8.60253 \cdot T$	Z. Moser [42]
$L^1_{Al,Mg} = 319.66 + 0.87286 \cdot T$	
$L^2_{Al,Mg} = 0.05$	

2.2.4 The MgO-Al_2O_3 Binary System

B. Hallstedt [46] assessed the MgO-Al_2O_3 binary system. The available experimental data mainly concerned phase boundaries, such as liquidi, solidi and solid solubilities, and there were no data on the mixing properties of the liquid phase.

Al_2O_3 is very soluble in spinel at high temperatures. When excess Al^{3+} is introduced into spinel, cation vacancies are also formed to maintain electroneutrality. These vacancies form on either tetrahedral or octahedral sites, or both. MgO is moderately soluble in spinel. For each Al^{3+} removed, 1.5 Mg^{2+} must be introduced, and it is assumed that the extra 0.5 Mg^{2+} goes into octahedral sites that are not normally occupied. With the above information, the formula for spinel with the possibility to dissolve MgO and Al_2O_3 can be written as:

$$(Al^{3+}, Mg^{2+})_1 (Al^{3+}, Mg^{2+}, Va)_2 (Va, Mg^{2+})_2 (O^{2-})_4$$

The Gibbs energy of spinel is then given by the following expression:

$$\begin{aligned} G_m = {} & y_M^T y_M^O y_V^I G_{MMV}^0 + y_M^T y_M^O y_M^I G_{MMM}^0 + y_M^T y_A^O y_V^I G_{MAV}^0 \\ & + y_M^T y_A^O y_M^I G_{MAM}^0 + y_M^T y_V^O y_V^I G_{MVV}^0 + y_M^T y_V^O y_M^I G_{MVM}^0 \\ & + y_A^T y_M^O y_V^I G_{AMV}^0 + y_A^T y_M^O y_M^I G_{AMM}^0 + y_A^T y_A^O y_V^I G_{AAV}^0 \\ & + y_A^T y_A^O y_M^I G_{AAM}^0 + y_A^T y_V^O y_V^I G_{AVV}^0 + y_A^T y_V^O y_M^I G_{AAV}^0 \\ & + RT[y_M^T \ln y_M^T + y_A^T \ln y_A^T + 2(y_M^O \ln y_M^O + y_A^O \ln y_A^O \\ & + y_V^O \ln y_V^O + y_V^I \ln y_V^I + y_M^I \ln y_M^I)] \end{aligned} \tag{2-4}$$

where the superscript T denotes the tetrahedral sublattice, O the octahedral sublattice, and I the interstitial sublattice. G_{MMV}^0, G_{MMM}^0, G_{MAV}^0, G_{AMV}^0, G_{AMM}^0, G_{AAV}^0, G_{AAM}^0, G_{AVV}^0

and G^0_{AAV} represent the Gibbs energies of the real or hypothetical compounds used as references to express the Gibbs energy of the spinel phase. y_i^j denotes the site fraction of species i in sublattice j. T is temperature and R is the gas constant. The thermodynamic parameters corresponding to the spinel phase are listed in Table 2.4, and the phase diagram calculated with these parameters is presented in Fig. 2.10.

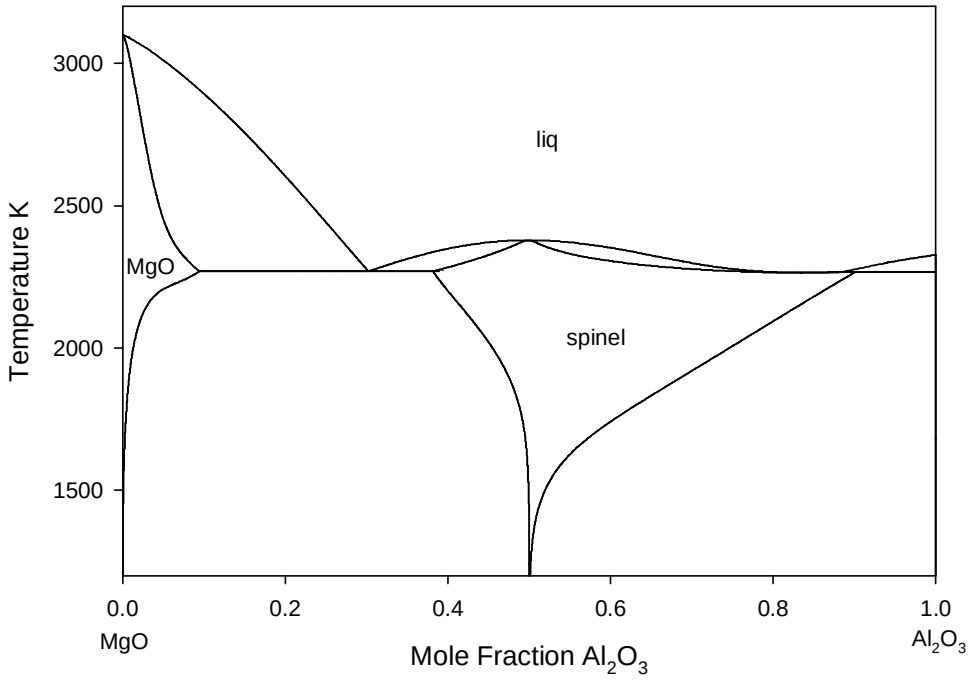

Fig. 2.10 The MgO-Al_2O_3 binary phase diagram [46]

Table 2.4 Thermodynamic parameters for spinel in Al_2O_3-MgO binary system [46]

GGAMMA =

(600<T<1500)

-1708389.72+791.591946T-121.754Tln(T)-0.0075467T^2+2.89573E-7T^3+2222750T^(-1)

GPERICLA=

(298.15<T<1700)

-619428.502+298.253571T-47.4817Tln(T)-0.00232681T^2+4.5043E-8T^3+516900T^(-1)

GCORUND=

(600<T<1500)

-1724886.06+754.856573T-116.258Tln(T)-0.0072257T^2+2.78532E-07T^3+2120700T^(-1)

NSPINEL=

(298.15<T<3000)

GPERICLA+GCORUND-27600-62T+9Tln(T)

MSPINEL=

(298.15<T<3000)

GPERICLA+58000-18T

ISPINEL=

(298.15<T<3000)

NSPINEL+51600-39T

$G^0_{MAV} = \text{NSPINEL}$

$G^0_{AMV} = 2\text{ISPINEL}+23.05130263670154\text{T}$

$G^0_{AVV} = 8\text{GGAMMA}+44.95159068617350\text{T}$

$G^0_{MVV} = 8\text{GGAMMA}+\text{NSPINEL}+44.95159068617350\text{T}+108000$

$G^0_{MMV} = \text{NSPINEL}+2\text{ISPINEL}+23.05130263670154\text{T}$

$G^0_{MMM} = 8\text{MSPINEL}-\text{NSPINEL}-2\text{ISPINEL}$

$G^0_{MAM} = 8\text{MSPINEL}-\text{NSPINEL}-4\text{ISPINEL}-23.05130263670154\text{T}$

$G^0_{MVM} = 8\text{GGAMMA}+8\text{MSPINEL}-\text{NSPINEL}-4\text{ISPINEL}+21.90028804947196\text{T}+108000$

$G^0_{AAM} = 8\text{MSPINEL}-2\text{NSPINEL}-4\text{ISPINEL}-23.05130263670154\text{T}$

$G^0_{AVM} = 8\text{GGAMMA}+8\text{MSPINEL}-2\text{NSPINEL}-4\text{ISPINEL}+21.90028804947196\text{T}$

$G^0_{AMM} = 8\text{MSPINEL}-2\text{NSPINEL}-2\text{ISPINEL}$

2.3 Kinetics

2.3.1 Nucleation and Growth Models

Many transformations involve the nucleation followed by the growth of a new phase. Nucleation starts with the formation of small embryo clusters. Some embryos shrink, while others eventually grow to reach a critical size beyond which the nuclei become stable. The transformation is then characterized by the growth of stable nuclei. The growth stage may be either interface-controlled, when the parent-product interface propagation is governed by the atomic processes on the interface, or diffusion-controlled, when the growth rate is determined entirely by the diffusion conditions. Once the product particles grow to a considerable size, impingement starts, raising mutual interference between the growth of independent particles.

2.3.1.1 The JMAK Model (Interface-Controlled Growth)

The concept of extended volume [47-49] was introduced to describe the transformation kinetics with the mutual interference between particles being present. To derive the JMAK equation, we define X_e as the volume fraction that has transformed after time t. dX_e is then the volume fraction which has transformed after time t due to the particles that nucleated between τ and $\tau+d\tau$. Also I is defined as the nucleation rate and v as the growth rate.

Assuming the particles would grow at the same rate in all directions, one can have [50]:

$$dX_e = \frac{4\pi}{3} v^3 (t-\tau)^3 I d\tau \tag{2-5}$$

Integrating Equation (2-5) with the initial condition at t=0 and $X_e=0$ results in:

$$X_e = \frac{4\pi}{3} v^3 \int_0^t (t-\tau)^3 I d\tau \tag{2-6}$$

In Equation (2-6), the volume fraction transformed becomes infinite with time. The growth of the new phase can only proceed into the untransformed volume. Of the new volume which makes up dX_e, a fraction 1-X on the average will lie in the previously untransformed material. Therefore, we can write:

$$\frac{dX}{dX_e} = (1-X) \tag{2-7}$$

So that:

$$X = 1 - \exp(-X_e) \tag{2-8}$$

Inserting the value of X_e from Equation (2-6) to Equation (2-8) gives the transformed volume fraction as a function of time [51]:

$$X = 1 - \exp[-\frac{4\pi}{3} v^3 \int_0^t (t-\tau)^3 I d\tau] \tag{2-9}$$

If there are N_0 sites per unit volume at the beginning and these are consumed as time proceeds, then the nucleation rate decreases with time and can be written as.

$$N = N_0 \exp(-\upsilon t) \tag{2-10}$$

where the frequency υ denotes the rate at which an individual site becomes a nucleus. According to Equation (2-10), the nucleation rate per unit volume is given by:

$$I = -\frac{dN}{dt} = N_0 \upsilon \exp(-\upsilon t) \tag{2-11}$$

Substituting Equation (2-11) into Equation (2-9) and integrating by parts gives [52]:

$$X = 1 - \exp\{-\frac{8\pi N_0 v^3}{\upsilon^3}[\exp(-\upsilon t) - 1 + \upsilon t - \frac{\upsilon^2 t^2}{2} + \frac{\upsilon^3 t^3}{6}]\} \tag{2-12}$$

Two extreme cases of the nucleation rate are the case of instantaneous nucleation

(also called the site-saturation nucleation) and the case of continuous nucleation (also called the constant-rate nucleation) [53]. Instantaneous nucleation refers to the case where the nucleation sites are consumed in a very short period at the beginning of a transformation, so that the subsequent volume increase of the product phase is purely due to nuclei growth with no more new nuclei formed. For continuous nucleation, the space contains no nuclei initially, and nuclei appear uniformly in space and time on uncovered space. Of course, there is an intermediate condition where the nucleation rate decays with time. A schematic drawing to illustrate these three kinds of scenario is presented in Fig. 2.11.

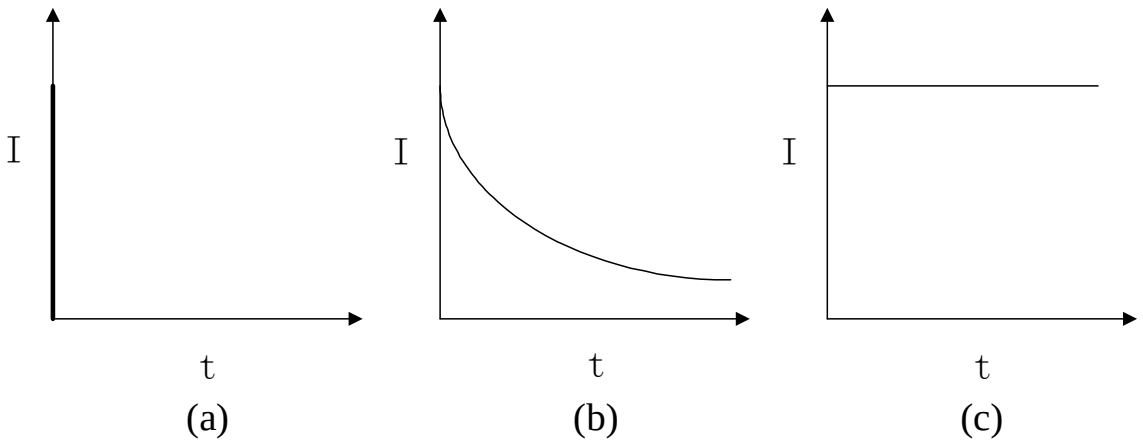

Fig. 2.11 A schematic drawing to illustrate: a:) Instantaneous nucleation, b:) Decaying nucleation and c:) Constant nucleation

We now present exact solutions for the above three cases.

(1) Instantaneous nucleation

For large υ, the number of nucleation sites decreases rapidly and the t^3 term in the bracket of Equation (2-12) dominates, which leads to [54]:

$$X = 1 - \exp\{-\frac{4\pi}{3} N_0 v^3 t^3\} \tag{2-13}$$

(2) Constant nucleation

For small υ, the number of nucleation sites is given approximately by:

$$N \approx N_0(1 - \upsilon t) \tag{2-14}$$

and the nucleation rate can be written as:

$$I = -\frac{dN}{dt} = N_0 \upsilon \tag{2-15}$$

For small υ, the exponential in Equation (2-12) can be expanded as:

$$\exp(-\upsilon t) = 1 - \upsilon t + \frac{\upsilon^2 t^2}{2} - \frac{\upsilon^3 t^3}{6} + \frac{\upsilon^4 t^4}{24} - ... \tag{2-16}$$

The first four terms in this expression cancel out other terms in Equation (2-12) and the first remaining term in the bracket of Equation (2-12) is t^4, which leads to [55]:

$$X = 1 - \exp\{-\frac{8\pi N_0 v^3}{\upsilon^3} \cdot \frac{\upsilon^4 t^4}{24}\} = 1 - \exp\{-\frac{\pi}{3} I v^3 t^4\} \tag{2-17}$$

(3) Decaying nucleation

For intermediate value of υ, Equation (2-12) can be directly used to describe such a condition [56]. In general, the JMAK equation gives the transformed fraction X as a function of time t, which can be expressed as [57-62]:

$$X = 1 - \exp[-(k_A t)^n] \tag{2-18}$$

where n is a constant often referred to as the Avrami exponent, k_A is a temperature-dependent factor which depends on the nucleation rate and the growth rate.

2.3.1.2 The AR Model (Diffusion-Controlled Growth)

The JMAK equation has been applied to many types of reactions with nucleation and growth, but deviations from JMAK kinetics have been noticed and reported. The assumption of constant growth rate is appropriate when the interface propagates into a region of constant composition, making the growth rate not depend on the interface position and time.

However, the assumption of constant growth rate is not valid when precipitate particles nucleate and grow into a solid solution with non-uniform composition, which requires diffusion around precipitates. Diffusion is then the rate-limiting step, and particles grow as fast as diffusion allows. The impingement concerned in the interface-controlled transformation is only hard impingement, but for the diffusion-controlled growth, soft impingement, impingement of growing depleted or enriched zones, should also be taken into consideration. For the diffusion-controlled growth, the impingement of diffusion fields around randomly distributed products is an extremely complex mathematical problem.

Similar to the JMAK model, the AR model is also described with the extended volume. If the impingement is taken into consideration by [63-64]:

$$\frac{dX}{dX_e} = (1 - X)^{\lambda} \tag{2-19}$$

where λ is a positive impingement parameter. The general solution of Equation (2-19) is:

$$X = 1 - \{\frac{X_e}{\eta} + 1\}^{-\eta} \tag{2-20}$$

where $\eta = 1/(\lambda - 1)$.

As can be seen, Equation (2-20) incorporates the JMAK equation when $\eta \to \infty$, which represents the ideal case. For the diffusion-controlled growth, the radius of a particle with isotropic growth can be expressed as:

$$r(T,t) = a(T)\sqrt{\tilde{D}t} \tag{2-21}$$

where $\tilde{D}$ is the diffusion coefficient, a(T) is a function of temperature. The volume of a particle can be expressed:

$$V = \frac{4\pi}{3} a^3 \tilde{D}^{3/2} (t - \tau)^{3/2} \tag{2-22}$$

The corresponding extended volume can be written as:

$$X_e = \frac{4\pi}{3} \int_0^t a^3 \tilde{D}^{3/2} I (t - \tau)^{3/2} d\tau \tag{2-23}$$

Inserting the expression of nucleation rate I described in Equation (2-11) and Equation (2-23) into Equation (2-19), one can get the equation to deal with the diffusion-controlled growth.

In general, the following equation is used for the diffusion-controlled case [65-67]:

$$X = 1 - \{\frac{(kt)^{n_s}}{\eta} + 1\}^{-\eta} \tag{2-24}$$

where n_s is a parameter akin to the Avrami exponent in Equation (2-18).

2.3.2 Steady-state Growth of a Product Layer

In this section, we consider the growth of a compound as a continuous layer on a planar substrate. For the reaction to continue, the reactant species have to diffuse across the product layer. At the initial stage, the rate of compound formation is controlled by the interfacial process at the reaction front as long as the product phase is thin enough. With increasing time, the resistance to diffusion in the product layer increases in comparison with the resistance to the phase boundary movement. Finally, if the phase boundary movement resistance can be neglected with comparison to the diffusion resistance, then local thermodynamic equilibrium will be attained at the interface, and the rate is limited by diffusion in the compound layer [68].

2.3.2.1 Solid-Solid Reaction

The kinetic equation that can express the growth rate of a compound layer as a result of diffusion in the product phase and the subsequent reaction on the interface can be written as [69-70]:

$$\frac{dx}{dt} = \frac{1}{(\frac{x}{k_{diff}} + \frac{1}{k_{reac}})} \tag{2-25}$$

where x is the compound layer thickness, k_{diff} and k_{reac} denote the diffusion constant and the reaction constant, respectively. Equation (2-25) can be simplified, depending on different conditions.

2.3.2.1.1 Interface-Controlled Kinetics

If x is very small, then Equation (2-25) can be simplified to:

$$\frac{dx}{dt} = k_{reac} \tag{2-26}$$

With the initial condition at x=0 and t=0, Equation (2-26) can be integrated into:

$$x = k_{reac} \cdot t \tag{2-27}$$

which is the well-known linear kinetics. k_{reac} is a parameter related to the structure of the interface, which acts as a barrier for ions or atoms to jump across it. The temperature dependence of k_{reac} can be described by the Arrhenius equation as:

$$k_{reac} = k_0 \exp(\frac{-Q}{RT}) \tag{2-28}$$

where k_0 is a frequency constant, and Q is the activation energy.

A linear rate of spinel formation is observed if the product layer is thin enough. P. G. Kotula [71] studied the NiO-Al_2O_3 reaction couple. In order to avoid the nucleation step, a 20 nm buffer layer of $NiAl_2O_4$ was first grown on the sapphire substrate by pulsed-layer deposition followed by 400 nm of NiO. Two kinds of sapphire wafers were chosen for this study, namely $\{0001\}$ and $\{1\bar{1}02\}$. The diffusion couples were annealed at 1100°C, and the relevant results were presented by a plot of spinel layer thickness against time, as shown in Fig. 2.12. The linear relationship indicates the spinel formation is rate-limited by the interface reaction. For the $\{0001\}$ reaction couple, the reaction rate is nearly two orders of magnitude smaller than that for the $\{1\bar{1}02\}$ reaction couple, which shows the interfacial reaction is dependent on the crystal orientation.

Y. Simpson [72] also investigated the NiO-Al_2O_3 reaction couple. The NiO layer was prepared by evaporating Ni onto the alumina substrate and subsequently oxidizing it in air at 700°C. Four kinds of sapphire wafers were used for his research, namely $\{0001\}$, $\{11\bar{2}0\}$, $\{1\bar{1}00\}$, and $\{1\bar{1}02\}$. The samples were annealed at 1020°C in air and then characterized by the Rutherford back-scattering spectroscopy. The results showed that the

rate of $NiAl_2O_4$ formation was dependent on crystal orientation, and the rate was found to decrease in the following order:

$$\{1\bar{1}02\} > \{1\bar{1}00\} > \{11\bar{2}0\} > (0001)$$

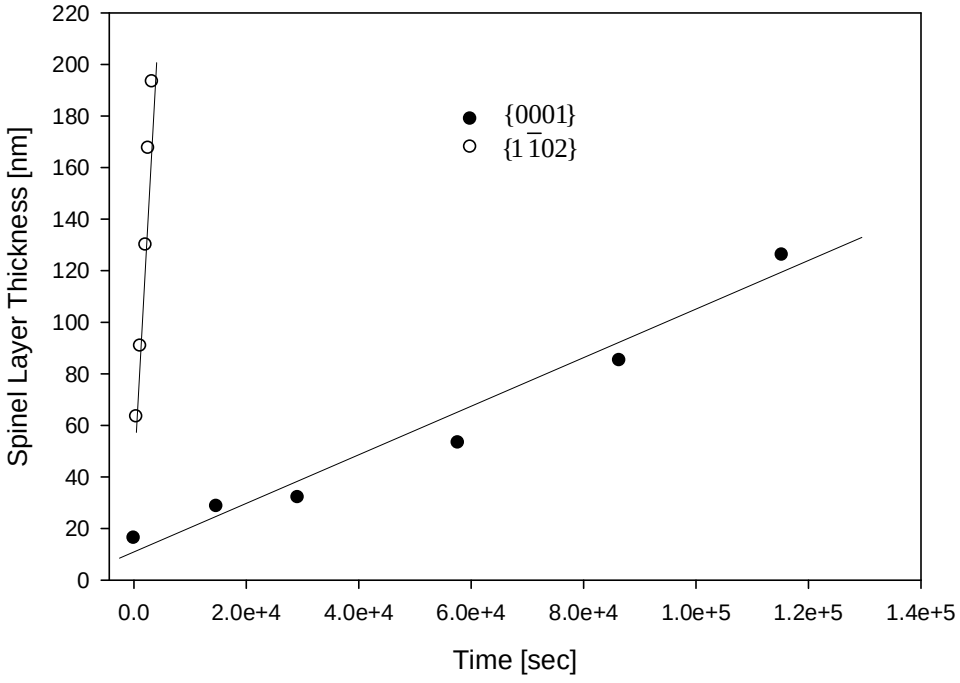

Fig. 2.12 A Plot of spinel layer thickness against time for {0001} and $\{1\bar{1}02\}$ Sapphire-bearing reaction couples [72]

2.3.2.1.2 Diffusion-Controlled Kinetics

If x is relatively large, then Equation (2-25) can be simplified to:

$$\frac{dx}{dt} = \frac{k_{diff}}{x} \tag{2-29}$$

With the initial condition at x=0 and t=0, Equation (2-29) can be integrated into:

$$x^2 = 2k_{diff}t \tag{2-30}$$

It must be noted that k_{diff} is the diffusion constant rather than the interdiffusion coefficient $\tilde{D}$. However, these two parameters can be related by one equation. The formation of $MgAl_2O_4$ in a MgO-Al_2O_3 diffusion couple provides a good example, where one can obtain [26]:

$$\tilde{D} = -C_{Al}^{spinel-MgO} \cdot \frac{\sqrt{2}}{8} \sqrt{\frac{k_{diff}}{t}} \left(\frac{\Delta C_{Al}^{spinel}}{\Delta x}\right)^{-1} \tag{2-31}$$

where $C_{Al}^{spinel\text{-}MgO}$ is the Al concentration in spinel at the $MgAl_2O_4$-MgO interface, and $\Delta C_{Al}^{spinel}/\Delta x$ is the slope of compositional profile of Al in spinel.

As the grain boundaries in the product layer can act as effective nucleation sites and fast diffusion paths, the effective diffusion coefficient may be used, which is defined by [73]:

$$D_{eff} = D_l + \frac{\delta_b}{2\omega} D_b \tag{2-32}$$

where δ_b is the width of grain boundary, ω is the size of grain, D_l and D_b are the diffusion coefficients in the lattice and on the grain boundary, respectively.

F. Pettit [74] examined NiO-Al_2O_3 diffusion couples between 1200°C and 1500°C for up to 300 hours with both oxides being polycrystalline. Parabolic kinetics were observed, and the temperature dependence of the diffusion constant followed the Arrhenius equation, with an activation energy of 115 kcal/mol. The Ni and Al concentration profiles in $NiAl_2O_4$ obtained at 1500°C were found to be linear with position by the electron microbe analysis.

W. Minford [75] investigated the kinetics of $NiAl_2O_4$ formation with a diffusion couple of {001} NiO /{0001} Al_2O_3. The samples were annealed at 1437°C, 1540°C

and 1630°C for 20 hours, 15.5 hours and 8 hours, respectively. Parabolic kinetics were observed, and the obtained parabolic constant as a function of temperature was found to be:

$$k = 1.4\times10^{4}\exp(\frac{-108000}{R\cdot T}) \quad \text{cm}^2/\text{s} \tag{2-33}$$

Compared with the work of F. Pettit, this result showed that the activation energy for spinel formation with the single crystal diffusion couple was nearly the same as that for the polycrystal diffusion couple.

L. Navias [76] studied the reaction between MgO vapor and sapphire to form $MgAl_2O_4$ in a hydrogen atmosphere in a temperature range of 1500°C and 1900°C for a time period of 1 to 50 hours. The rate of spinel formation was proved to obey parabolic kinetics, and the activation energy was calculated to be about 100 kcal/mol.

E. Bruce [26] investigated the kinetics of $MgAl_2O_4$ formation with the MgO-Al_2O_3 reaction (both in single crystal state) from 1200°C to 2000°C, and parabolic kinetics were obtained. The activation energy was determined to be 410 kJ/mol. The Al and Mg concentration profiles were found to be a linear function of position. The diffusion constant included a kinetic component related to diffusion through the product layer and a thermodynamic component associated with the product composition. Consequently, the activation energy calculated was not the activation energy for the diffusion process.

The effect of sapphire orientation on the kinetics of spinel formation was systematically studied by R. Rossi [72]. Five groups of diffusion couples were used with the combinations of different crystal orientations:

$$(100)_{MgO} \sim (0001)_{sapphire}$$

$$(100)_{MgO} \sim (10\bar{1}0)_{sapphire}$$

$$(100)_{MgO} \sim (11\bar{2}0)_{sapphire}$$

$$(111)_{MgO} \sim (0001)_{sapphire}$$

$$(111)_{MgO} \sim (22\bar{4}3)_{sapphire}$$

The annealing was conducted at 1560°C in air for 250 hours and the average thicknesses of spinel layers were measured to be 0.934, 0.920, 0.922, 0.920 and 0.927 mm, respectively. It was concluded that sapphire orientation had no effect on the spinel formation kinetics.

2.3.2.1.3 Mix-Controlled Kinetics

If x has an intermediate value, then the rate is limited by both the interface reaction and the diffusion process. Integration of Equation (2-25) with the initial condition at t=0 and x=0 yields:

$$t = \frac{x^2}{4k_{diff}} + \frac{x}{2k_{reac}} \tag{2-34}$$

Dividing Equation (2-34) by x on both sides and rearranging leads to:

$$x = 4k_{diff}\frac{t}{x} - \frac{2k_{diff}}{k_{reac}} \tag{2-35}$$

From Equation (2-35), a plot of x with respect to t/x yields a straight line, whose slope and intercept can be used to determine k_{diff} and k_{reac}.

P. Kotula and C. Carter [78] investigated the $NiAl_2O_4$ formation at 1000°C, 1050°C and 1100°C in air by thin-film reaction couples. A $NiAl_2O_4$ buffer layer with the thickness of 20 nm was grown on sapphire by pulsed-laser deposition followed by a NiO layer of 400 nm. A plot of x with respect to t/x is shown in Fig. 2.13. The straight lines

fitted to the data at 1000°C indicated that the rate was limited by diffusion and interface reaction, and that the intercepts of the straight lines at 1000°C for both sapphire orientations had negative values. However, the reaction at 1050°C and 1100°C for both sapphire orientations had parabolic kinetics, i.e. the intercepts of these straight lines had a zero value.

For the $\{1\bar{1}00\}$ reaction couple, the activation energy for diffusion was 461 kJ/mol and that for the interface reaction was 574 kJ/mol. For the $\{1\bar{1}02\}$ reaction couple, the activation energy for the diffusion was 464 kJ/mol, which was consistent with that for the $\{1\bar{1}00\}$ reaction couple. But the activation energy for the interface reaction was 366 kJ/mol. The results showed that the diffusion process was not dependent on the crystal orientation, while the chemical reaction was.

If the activation energy of interface reaction is larger than that for the diffusion process, a decrease in temperature will make the rate of interfacial reaction decrease far more rapidly than the diffusion rate. Therefore, at low temperatures, the rate of interface reaction at the phase boundary would limit the rate of compound formation, which is the case for the $\{1\bar{1}00\}$ reaction couple. Naturally, at lower temperatures, the growth rate of a compound is slow, but the linear kinetic regime becomes longer and therefore the compound growth can be studied more easily by experiments. As can be seen in Fig. 2.13, the intercepts are nearly equal to zero at high temperatures, while they are negative at low temperatures.

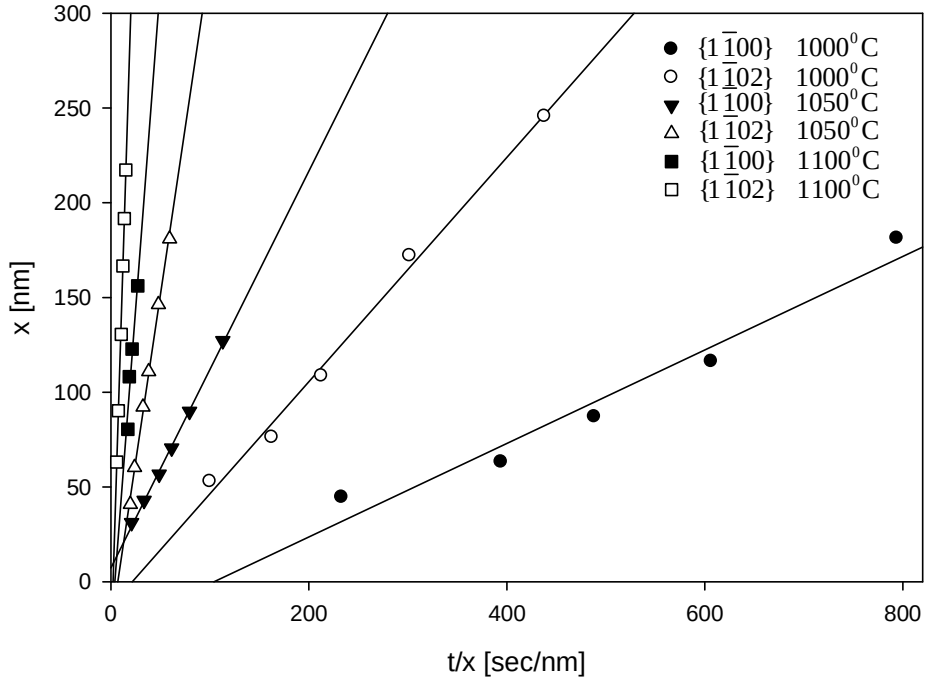

Fig. 2.13 A plot of spinel reaction-layer thickness versus time for $\{1\bar{1}00\}$ and $\{1\bar{1}02\}$ Sapphire-bearing reaction couples [78]

2.3.2.2 Solid-Liquid Reaction

Two processes can take place simultaneously during solid-liquid reactions: chemical compound formation and its dissolution. The equation describing the growth of a compound layer should involve a term related to the dissolution process. As a result, Equation (2-25) should be modified [79]:

$$\frac{dx}{dt} = \frac{1}{(\frac{x}{k_{diff}} + \frac{1}{k_{reac}})} - \dot{R} \qquad (2\text{-}36)$$

where $\dot{R}$ denotes the dissolution rate of the compound in the melt.

2.3.2.2.1 Dissolution Kinetics in Saturated Melts

Consider the growth of a compound layer in the melt which is pre-saturated with the dissolving species. If the observed layer thickness is relatively large, it is possible that the formation is rate-limited by the diffusion in the product. The dissolution term in Equation (2-36) can be ignored, and thus one can have [80]:

$$\frac{dx}{dt} = \frac{k_{diff}}{x} \tag{2-37}$$

This indicates that the formation of a compound still obeys the parabolic law.

N. Tunca [81] studied the growth kinetics of Al_3Nb with solid Nb and molten Al which was pre-saturated with Nb at temperatures ranging from 700°C to 1100°C. The disk samples were horizontally immersed into the melt and the thickness of Al_3Nb was plotted against square root of time, as seen in Fig. 2.14.

It was found the Al_3Nb layer grew a little faster on the sample bottom than on the sample top. The author ascribed the difference to the presence of natural convection brought about by the Nb concentration gradient in the melt without any further explanation. It was also found that the activation energy calculated from the diffusion constant was higher for the sample top (207.73 kJ/mol) than for the sample bottom (185.80 kJ/mol).

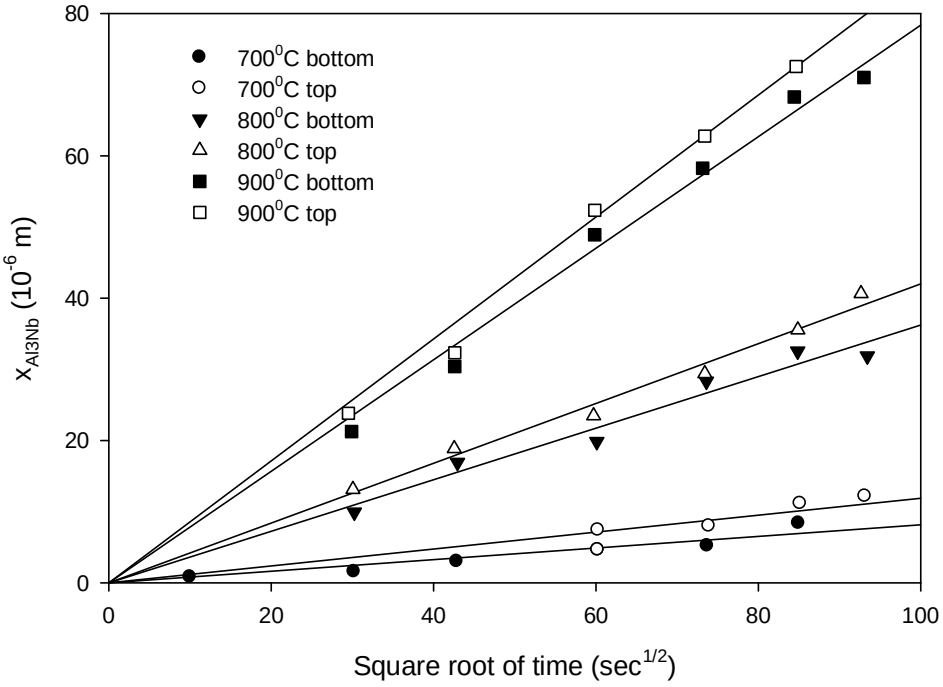

Fig. 2.14 A plot of Al_3Nb layer thickness as a function of square root of time [81]

2.3.2.2.2 Dissolution Kinetics in Unsaturated Melts without Natural or Forced Convection

The dissolution of a compound into a melt usually involves two steps: dissociation of the compound into ions or atoms and the subsequent diffusion of these ions or atoms into the melt. Consequently, the dissolution kinetics may be rate-limited by the interface dissociation, the diffusion in the melt, or both of them.

1) The Dissociation-Controlled Dissolution:

For the case where the dissolution is rate-limited by the dissociation process, the diffusion of these ions or atoms in the melt is so fast that no concentration boundary layer will develop. Under this condition, the dissolution rate is independent of time [82-83].

$$\dot{R} = \text{constant} \tag{2-38}$$

The dissolution rate may be a function of crystal orientation and temperature.

2) The Diffusion-Controlled Dissolution:

For the case where the dissolution is rate-limited by the diffusion process, a concentration boundary layer will develop whose thickness is proportional to the square root of time. Under this condition, the dissolution rate is inversely proportional to the square root of time [84-85]:

$$\dot{R} = \frac{k_{diss}}{\sqrt{t}} \tag{2-39}$$

where k_{diss} is the dissolution constant. It may be a function of crystal orientation and temperature. Inserting Equation (2-39) into Equation (2-36) and integrating with the initial condition at t=0 and x=0 yields [86]:

$$x^2 = \{-k_{diss} + \sqrt{k_{diss}^2 + 2k_{diff}}\}^2 t \tag{2-40}$$

where the expression in {} is termed an effective parabolic constant.

From Equation (2-40), the formation of a compound layer still obeys the parabolic law in the presence of diffusion-controlled dissolution, but the parabolic constant deviates negatively from that for the case where dissolution is absent. It was found that the incongruent dissolution of sapphire into CaO-MgO-Al_2O_3-SiO_2 melts in the static condition followed this equation [86].

3) The Dissociation-Diffusion Controlled Dissolution:

For the case where the dissolution is rate-limited by both the dissociation and the diffusion in the melt, the concentration boundary layer will again develop and thicken with time. However, the dissolution is no longer governed by Equation (2-40). Y. Zhang

[84] related the dissociation rate with the diffusion in the melt through the saturation degree at the solid-liquid interface and then derived a differential equation which could describe the dissolution kinetics. Unfortunately, this equation can only be solved numerically.

The most convenient way to distinguish whether the dissolution is rate-limited by the pure diffusion process in the melt or the combination of dissociation and diffusion is to examine the composition of the melt adjacent to the interface. If the process is solely controlled by the diffusion process, the melt in contact with the compound should have the equilibrium composition which, in principle, could be obtained from thermodynamic and kinetic calculations.

K. Bouche [87] investigated the growth of a Fe_2Al_5 layer on solid iron rods that were vertically immersed in molten Al at 800°C for up to one hour. It was observed that the interface between Fe and Fe_2Al_5 appeared highly irregular. The average thickness was plotted against the square root of time, and the linear relationship indicated parabolic behavior. However, the straight line had a positive intercept, which implied that there should exist a faster reaction mechanism at the initial stage other than for parabolic kinetics.

H. Shahverdi [88] conducted the similar experiments, using rectangular iron coupons at 700°C, 800°C, and 900°C. The results are presented in Fig. 2.15. As can be seen, the curve has a maximum value at about 400 seconds at 900°C, indicating the importance of the dissolution process at this temperature. After about 400 seconds at 900°C, the rate of compound formation is smaller than the rate of dissolution. Consequently, the layer thickness decreases with time.

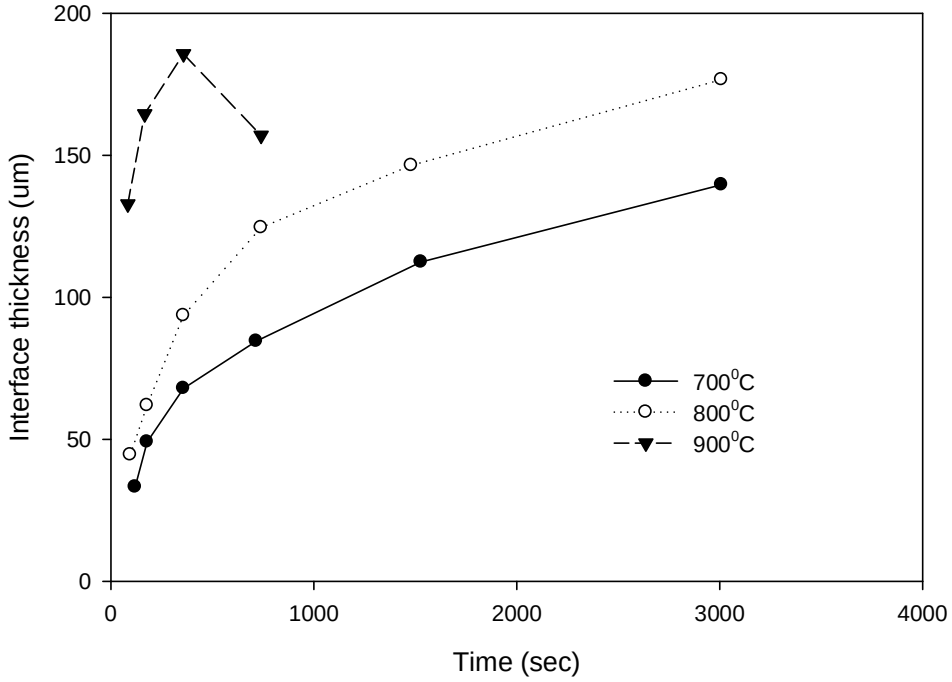

Fig. 2.15 A plot of Fe_2Al_5 thickness as a function of time at different temperatures [88]

2.3.2.2.3 Dissolution Kinetics in Unsaturated Melts with Natural Convection

When the normal of the solid-liquid interface is not parallel to the gravitational direction, the concentration gradient near the solid-liquid interface will result in natural convection [89-95]. Mathematically, the flow is intimately coupled to the concentration fields [96].

By analogy with the well-studied natural convection formed by heat transfer near a vertical plate, C. Wagner [97] derived an equation for the dissolution rate of a vertical plate for the case of natural convection:

$$\dot{R} = 0.545\tilde{D} \cdot C_s (\frac{g}{\nu \cdot y \cdot D} \cdot \frac{\Delta\rho}{\rho_0})^{\frac{1}{4}} \quad (2\text{-}41)$$

where y is defined as the distance from the upper sample edge where the flow starts, $\tilde{D}$ is the diffusion coefficient, C_s is the saturation concentration, ν is the kinematic viscosity, g is the gravitational acceleration constant, $\Delta\rho / \rho_0$ is the relative density change. This equation was successfully applied by C. Wagner to evaluate the dissolution rate of sodium chloride into water.

When steady-state natural convection is reached, the boundary layer does not vary with time but does vary with position. A typical steady-state natural convection boundary layer is schematically shown in Fig. 2.16 [98-99]. Because the motion of the melt decreases gradually to zero at the solid-liquid interface, mass transport at the interface still obeys Fick's first law [98]:

$$J = -\tilde{D} \cdot (\frac{\partial C}{\partial x})_{x=0} \quad (2\text{-}42)$$

By Equation (2-41) and Equation (2-42) and with δ defined by:

$$\delta = \frac{C_0 - C_\infty}{\left(\frac{\partial C}{\partial x}\right)_{x=0}} \quad (2\text{-}43)$$

an equation expressing the boundary layer thickness at steady state can be obtained:

$$\delta = 1.8\left(\frac{D \cdot \nu}{g}\right)^{\frac{1}{4}} (\frac{\Delta\rho}{\rho_0})^{-\frac{1}{4}} y^{\frac{1}{4}} \quad (2\text{-}44)$$

Inserting Equation (2-41) into Equation (2-36), a mathematical expression describing the formation and dissolution of a compound layer in the presence of natural convection can be obtained:

$$\frac{dx}{dt} = \frac{1}{(\frac{x}{k_{diff}} + \frac{1}{k_{reac}})} - 0.545D \cdot C_s (\frac{g}{\nu \cdot y \cdot D} \cdot \frac{\Delta\rho}{\rho_0})^{\frac{1}{4}} \qquad (2\text{-}45)$$

Integration of this equation with the initial condition at t=0 and x=0 will yield the relationship between x and t. With the constants obtained from the literature, the relationship between x and t can be calculated and compared with experimental results. As can be seen from Fig. 2.16, the dissolution rate at the sample top is much faster than that at the sample bottom. If a plate with two parallel surfaces is immersed in the melt, the plate will be dissolved into a wedge. Likewise, if the solid plate is initially coated with a layer of dissolvable compound with a uniform thickness, the sample top will be free of that compound after some time [100].

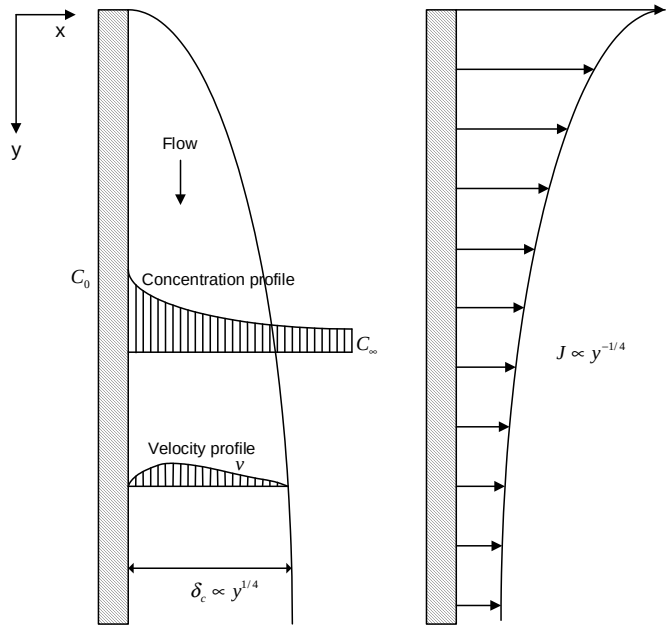

Fig. 2.16 A schematic drawing of the flow pattern for natural convection induced by the concentration gradient in the melt

2.3.3 Prior Work on Incongruent Reduction

Understanding the kinetics and mechanisms of incongruent reduction can aid process development for commercial applications. However, relevant information is not only extremely limited, but conflicting in the literature.

H. Jynge [101] studied the reaction between molten Mg and dense sintered alumina. The alumina, in the form of disks, was placed vertically in a graphite crucible filled with molten magnesium. Instead of using thickness and weight change measurements to characterize the kinetics, the author measured the Al content in the melt produced by the reaction. The data were plotted against time, but no useful quantitative kinetic information was obtained except that the reaction rate slowed down with time. XRD analysis reviewed the presence of MgO and $MgAl_2O_4$ on the alumina surface. As a result, the kinetic data reported by the author was, in fact, an indirect estimation of the average growth rate of MgO and spinel. EPMA was also conducted for the concentration profile of Mg and Al, but this analysis was not helpful for the identification of the overall rate-limiting step. Furthermore, the author failed to realize the possible importance of the dissolution process and therefore simply made an assumption of a diffusion-controlled process without direct any proof.

B. Hallstedt [102] examined the reaction rate between alumina fibers and liquid magnesium theoretically as well as experimentally at 1000K. In this case, both $MgAl_2O_4$ and MgO were formed on alumina surfaces. Assuming the diffusion-controlled growth of these two layers and using the counter diffusion of Mg^{2+} and Al^{3+} as the basis for his model, the author calculated two parabolic constants for the growth of spinel and MgO with the consideration of enhanced diffusion along grain boundaries. The result was then

applied to predict the presence of MgO and spinel in the fabrication of composites. The author came to the conclusion that the estimated amounts of the formed spinel and MgO amounts were so small that they were unlikely to appear at the temperature of 1000K within 10 minutes. The author did not realize that, at the initial stage of reaction, the compound layer formation could obey linear kinetics instead of a parabolic law. Again, the author did not consider the influence of dissolution of MgO on the overall kinetics.

E. Saiz [103] investigated the reaction between dense mullite and molten Al droplets at 1100°C. The reaction layer thickness was plotted against time and the result showed that a linear fit was valid for times up to 30 minutes. The concentration profile from the EPMA analyses could be fitted to an error function after 150 minutes, indicating a relatively slow diffusion process. The author thus drew the conclusion that the reaction was initially reaction-controlled and then limited by diffusion.

K. Brondyke [104] studied the penetration of silica by molten Al between 700°C and 900°C. Al reacted with silica to form alumina and the penetration rate of silica by molten Al decreased with time. Without any further data, the author tentatively concluded that the reaction was diffusion-controlled. A. Standage [105] conducted the reaction between a fused silica rod and molten Al. The rods were immersed in molten Al between 700°C and 800°C. The author reported, in nearly all the experiments, a linear relationship between penetration of reactants and time, which was opposite to the conclusion made by K. Brondike.

V. Gabis [106] investigated the corrosion of MgO, Al_2O_3 and $MgAl_2O_4$ by pure Al and 0.3 wt% Mg-Al alloys. Experiments were conducted in alumina crucibles. Pure sintered alumina, sliced electro-fused spinel and pure magnesia single crystal were totally

immersed in the melt at 800°C and 1000°C for 100 hours, respectively. For the case where alumina was immersed into 0.3% Mg-Al melts, discrete spinel particles were grown after 100 hours at 800°C, while for the case where spinel and MgO was immersed into the same melt, no reaction occurred. At a first glance, 0.3% Mg is just the composition for spinel, MgO and Mg-Al melt to be at equilibrium at that temperature. However, this equilibrium could not have been reached because alumina crucibles were used. It seems from his results that the equilibrium concentration of Mg should have been less than 0.3 wt%.

CHAPTER III

EXPERIMENTAL SETUP

All the high-temperature experiments were conducted with the apparatus shown schematically in Fig. 3.1, which contained three main parts:

1) A single-zone vertical furnace

The furnace used in this work was a vertical tube furnace (Model number: STF54453C, Volts: 208/240, Watts: 6.9 kW, Amps: 45, HZ: 50/60, Phase: 1, Max Temperature: 1500°C, Lindberg/Blue Inc.), that was heated by SiC rods that were symmetrically arranged. The current to the furnace was regulated by a digital 16 segment programmable controller, which was commercially attached to the vertical furnace.

2) A one-end-closed mullite tube

A one-end-closed mullite tube was used in this study, which was 3 inches in diameter, 58 inches in length, and 0.25 inches in thickness (commercially available from Coorstek Inc.). An Fe rod with a 6 mm diameter was used to suspend and adjust the sealed steel pipe (about 10 inches in length and 1.75 inches in diameter) with samples sealed inside. Steel was chosen as the canning material because it could sustain high temperatures in flowing argon, it could be easily sealed by welding, and, most importantly, Mg exhibits little reaction with Fe within the temperature range of experiments, as can be seen in Fig. 3.2.

3) A gas regulation system

All the experiments were conducted at high temperatures (above 900°C), and it is

imperative to prevent the steel can and the Mg-Al melts from oxidation. For this purpose, the reaction system shown in Fig. 3.1 contained a gas inlet and a gas outlet for argon gas. The flow rate of argon gas was controlled by a flowmeter (Model number: FM-1051A-HA, Matheson Inc.). A vacuum pump (Model number: 1402R, Sargent-Welch Scientific Inc.) was also attached to the gas-regulation system so that the mullite tube could be evacuated before high-purity argon gas was filled in the system for the experiments.

The temperature profiles in the vertical furnace were measured before any experiments were conducted. In this work, an S-type thermocouple (Platinum/10% rhodium vs. platinum, Omega Inc.) and a thermometer (Model number: HH506R, Omega Inc.) were used to calibrate the furnace controller. Measurements were performed at 900°C, 1000°C, 1100°C and 1200°C, respectively, and the temperature profiles are presented in Fig. 3.3. From Fig. 3.3, the temperature in the hot zone of the furnace was almost constant within the deviation of 2°C along a 3 inch length, which was sufficient to ensure a constant temperature for the experiments. For convenience, the temperature correlation between the furnace controller and the standard S-type thermocouple was recorded, as given in Fig. 3.4.

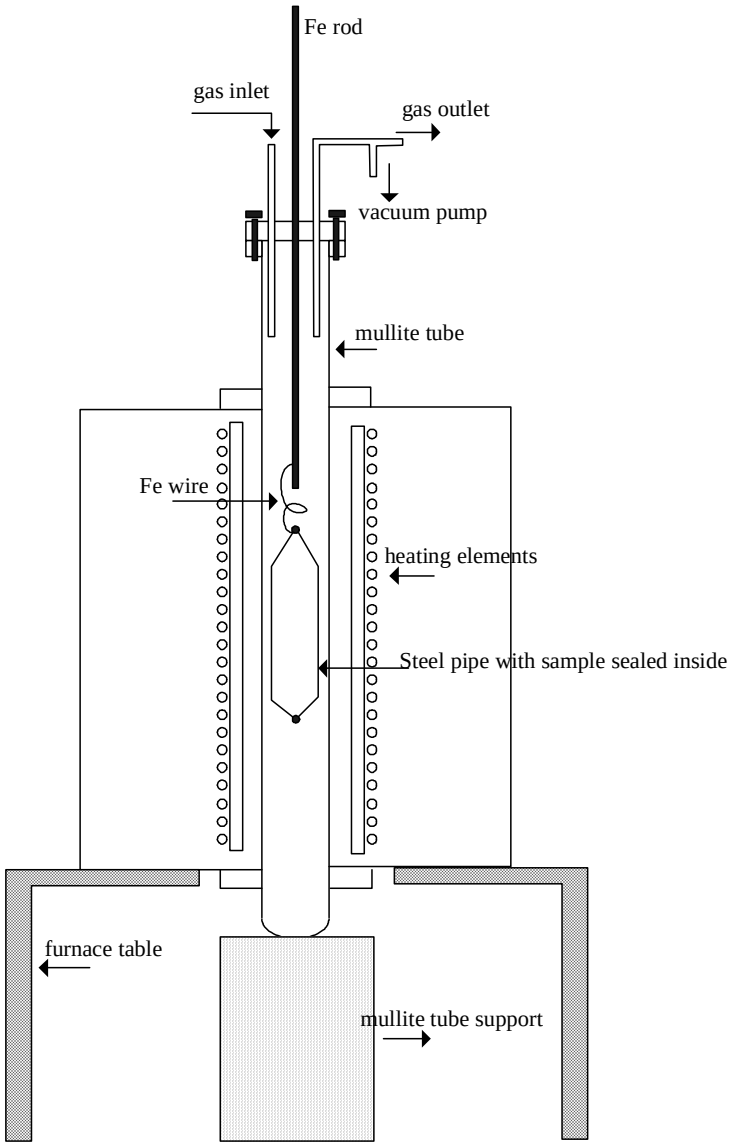

Fig. 3.1 The schematic drawing of furnace setup

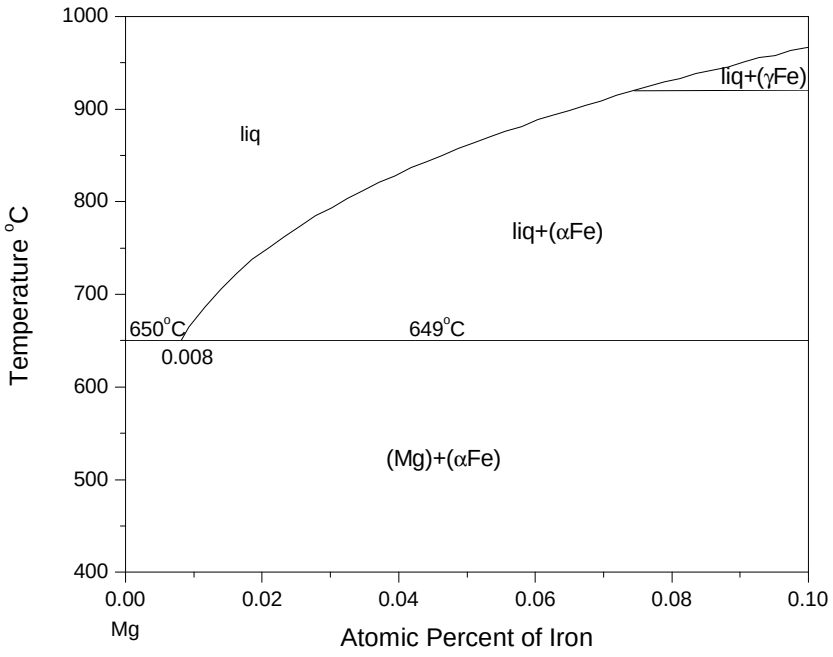

Fig. 3.2 The Fe-Mg binary phase diagram

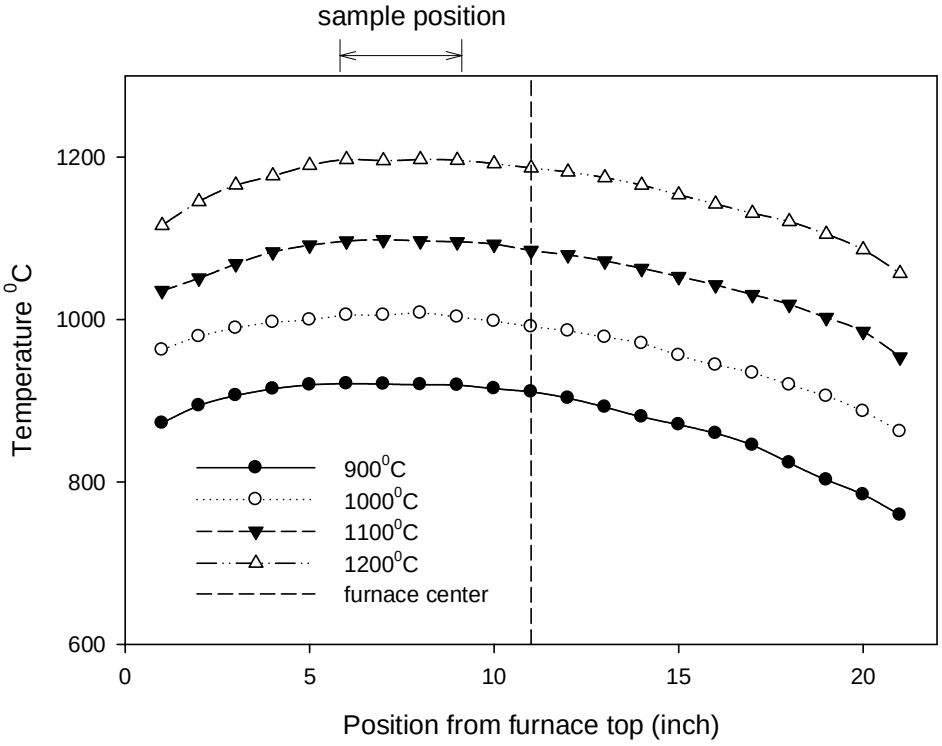

Fig. 3.3 The temperature profiles in the vertical furnace as a function of position

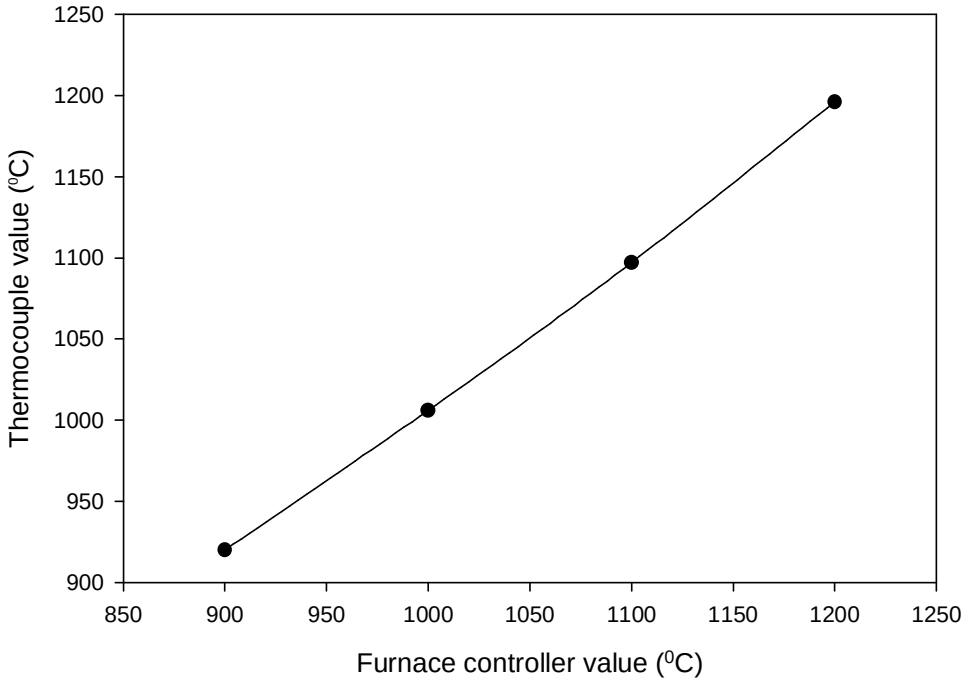

Fig. 3.4 The temperature correlation between the furnace controller and the standard S-type thermocouple

CHAPTER IV

OXYGEN-CONTROLLED ALLOY PREPARATION

4.1 Introduction

Mg-Al melts are known to be chemically reactive to some extent for most high temperature materials. Commercial MgO crucibles usually contain Y_2O_3 as a sintering agent and CaO as a main impurity, both of which can be reduced by and then enter Mg-Al melts at high temperatures. The presence of yttrium and calcium in the melt will change the activity of magnesium, which may alter the kinetic process.

Gelcasting is an attractive ceramic-forming technique for fabricating high-purity ceramic parts. It begins by combining ceramic powders, an organic monomer, a crosslinker and a dispersant to form a slurry. After the slurry is thoroughly mixed, a catalyst is then added. The slurry is poured into a heated mold for gelation. After the slurry has completely gelled, the product can then be removed from the mold and allowed to dry in a humidity-controlled atmosphere so that the product is dried slowly and does not crack. Once dried, the product can be subjected to binder burnout and sintering as for conventional ceramics. The processing additives are all organics that can be completely pyrolyzed so that no cation impurities are left behind in the fired crucibles.

Extensive studies on gelcasting have been reported in the literature, but those methods can not be directly applied to prepare high-purity MgO crucibles for the current research. The main problems are listed below:

1) Dispersants used by different authors are usually not commercially available. Although some are industrially available, their purities are not satisfactory.
2) Humidity control facilities for drying the gelled parts are not easy to obtain in the research lab.
3) The MgO powder has an intrinsic resistance to sintering relative to other ceramics, and there are no useful sintering parameters available for our purpose.
4) Mold release agents are not favored in the current research because of the high-purity requirement.

Although gelcasting was not a central component of this research, some preliminary gelcasting efforts were conducted to deal with the crucible contamination problem. In this chapter, a modified gelcasting method based on the work of S. Dhaera [107] is presented.

At an arbitrary fixed temperature and pressure, for a three-component system (Mg-Al-O) containing three phases (MgO, $MgAl_2O_4$, and Mg-Al-O melt) at equilibrium, the number of degrees of freedom predicted by the Gibbs phase rule is zero. A Mg-Al-O alloy obtained by such a three-phase-equilibrium experiment is called an oxygen-controlled alloy and was used for the chemical reaction to form spinel at other temperatures. The equilibrium concentrations of Mg in the Mg-Al-O melts in equilibrium with MgO and $MgAl_2O_4$ were experimentally investigated in the high-purity MgO crucibles prepared by the modified gelcasting method and theoretically calculated for different temperatures. These results are also presented in this chapter.

4.2 Experimental Procedure

Initial experimental results showed that S. Dhaera's [107] gelcasting method was not successful in the preparation of high-purity MgO crucibles. The material dried up and shrank on top of the open mold during polymerization, leaving many small cracks in the gelcasting parts. In addition, surface cracks were observed upon the removal of the parts from the molds, making the sintered crucibles more fragile.

With these defects prevalent, the gelcasting method had to be modified. In order to overcome the problems caused by water evaporation during the gelation process, a plastic ziploc bag was used so that the whole gelcasting process could be carried out within a constant water environment. The problem of surface cracks caused by the removal from molds was solved by directly casting the slurry into a commercial MgO crucible followed by the subsequent sintering of the whole assembly in the vertical furnace.

In this work, 15 grams of slurry made of 15 wt% aqueous monomer solution (Methacrylanmide, 99.99% purity, Sigma-Aldrich Inc.) and cross-linker (N,N'-methylene bisacrylamide, 99.99% purity, Sigma-Aldrich Inc.) mixed with a 6:1 weight ratio was used. 40 grams of magnesia powder (99.95% purity, Micro metals Inc.) and 5 grams of $MgAl_2O_4$ powder (99.985% purity, Alfa Aesar Inc.) were added in steps to attain the desired solid loading. 1 gram of 10 wt% ammonium persulfate (99.98% purity, Sigma-Aldrich Inc.) water solution was used as the catalyst. The gelation process was performed by casting the liquid mixture into a commercial MgO crucible and then heated at 80°C (water bath) for about 6 minutes in a plastic ziploc bag to eliminate surface cracks caused by water evaporation. Unlike traditional methods which require a

humidity-controlled atmosphere to dry the gelled parts, the products obtained in this work could be directly subjected to binder burnout without experiencing any drying process. The whole gelcasting process is schematically illustrated in Fig. 4.1. Binder burnout after gelcasting and sintering were conducted by hanging the commercial MgO crucible containing the gelcast liner as well as the gelation part in a vertical furnace and heating to 1400°C at a rate of 8°C/min and then holding of one hour.

For each equilibrium run, suitable amounts of Mg (99.9% purity, Alfa Aesar, MA), Al (99.999%, ALL-CHEMIE LTD, SC), MgO and $MgAl_2O_4$ particles with an average size of 5 mm in diameter (Table 4.1-4.3) were put into a MgO/$MgAl_2O_4$ crucible prepared by gelcasting and then sealed in a steel pipe with argon gas (99.998% purity, O_2<3ppm) protection to minimize the loss of Mg by evaporation at high temperatures. The steel pipe was then welded in Ar glove box. The whole assembly is schematically illustrated in Fig. 4.2. The crucible at the bottom was used for holding Mg-Al alloys and oxides. The porous crucible in the middle was used as a filter to let the liquid alloy flow through holes, with the oxides left behind. The crucible at the top was inversely positioned to receive the melt when the whole steel pipe assembly was inverted.

The sealed pipe was suspended in the isothermal zone of the vertical furnace with flowing argon gas protection, as mentioned in Chapter III. After a certain time at a certain temperature, the steel pipe was pulled out of the furnace, inverted quickly to allow the melt to flow out of the bottom crucible, and then quenched in water to preserve the equilibrium concentration. The whole process lasted for about 20 seconds. The quenched alloy was subjected to cutting, grinding and polishing so that its microstructure and composition could be characterized by SEM (LEO 1530 TFE-SEM, Georgia Tech) and

ICP analysis (Perkin-Elmer Elan 6000 ICP-MS, University of Georgia at Athens).

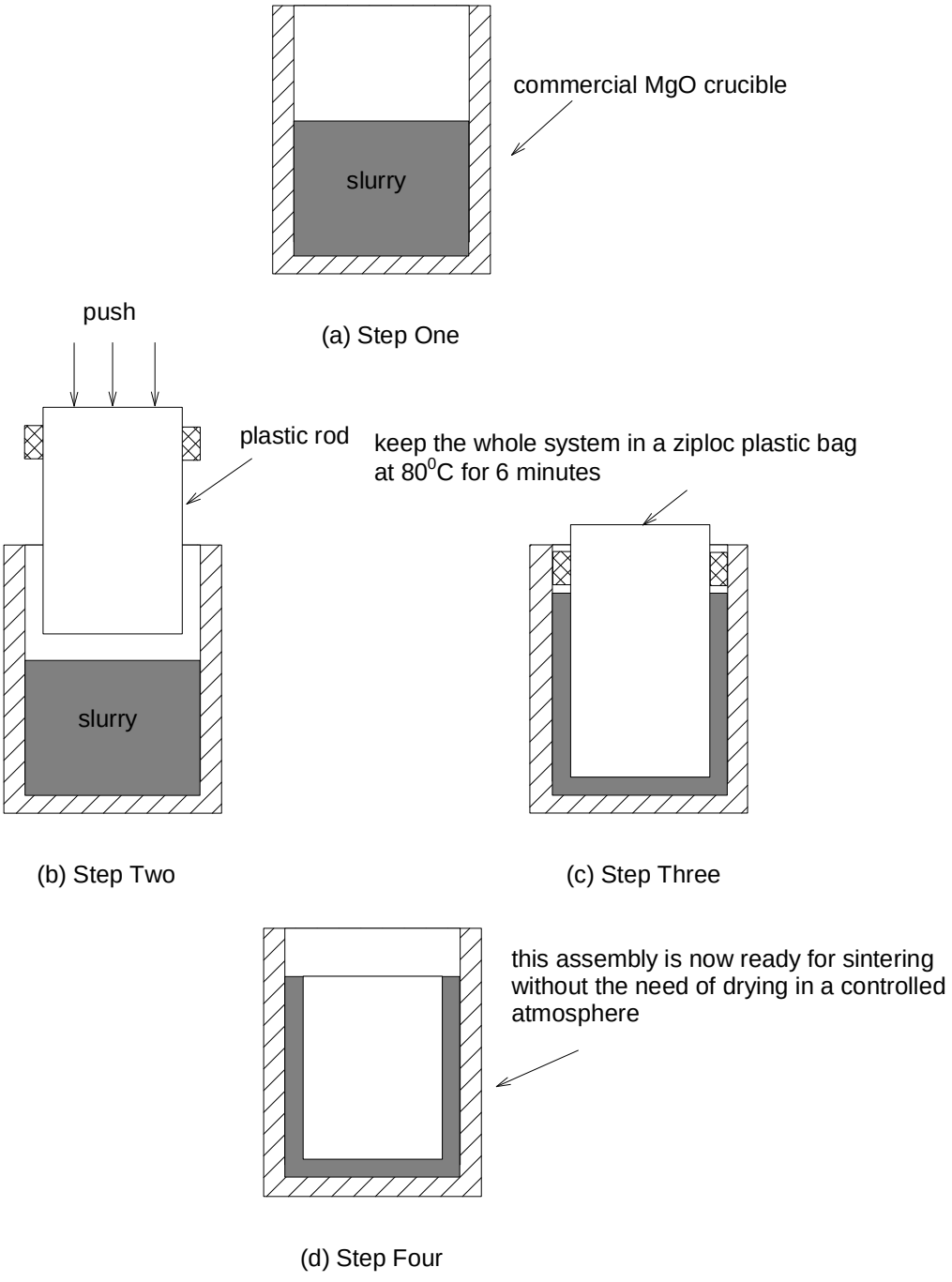

Fig. 4.1 Schematic drawing of the gelcasting process

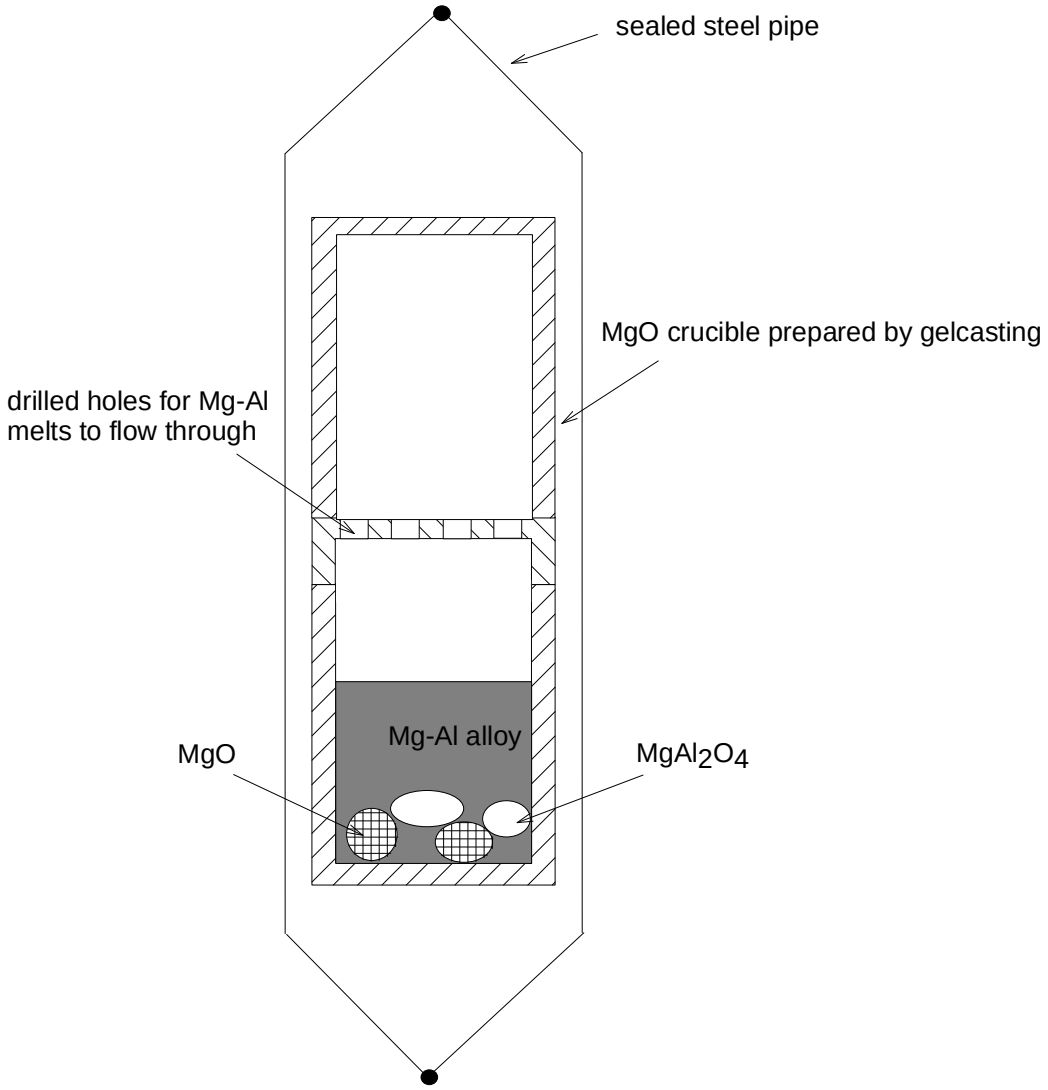

Fig. 4.2 The steel pipe assembly used for preparing oxygen-controlled alloys

4.3 Results

The top view and side view of a gelcast part in a commercial MgO crucible are shown in Fig. 4.3. The top view and side view of a sintered high-purity MgO crucible are presented in Fig. 4.4. It is seen that relatively dense and strong high-purity MgO crucibles were prepared by gelcasting for the current research.

The prepared high-purity MgO crucibles were used to contain Mg-Al alloys with 7 at% Mg at 1100°C for as long as three days to make sure the alloys prepared within the gelcast MgO crucibles were free of contamination. Similar experiments were also conducted in commercial MgO crucibles for comparison. The BSE images and the corresponding EDS results are presented in Fig. 4.5 and Fig.4.6, respectively. The BSE images and EDS results for the alloys prepared within high-purity MgO crucibles were free of impurity phases in the melts, indicating that high-purity Mg-Al alloys were obtained for further experiments. The BSE and EDS results for the alloys prepared within commercial MgO crucibles revealed a white second phase containing the impurities Y and Ca, which was indicative of chemical reactions between Mg, Y_2O_3 and CaO.

The oxygen-controlled alloys prepared in high-purity gelcast MgO/$MgAl_2O_4$ crucibles at different temperatures for different times were quenched in water to preserve the equilibrium concentrations and then examined by ICP analysis. The oxygen concentration in the Mg-Al melts was so low that it was not measured directly. However, when the initial Mg content was either higher or lower than the equilibrium value at a certain temperature, the Mg concentration would converge to the equilibrium value with time during the experiment. At the same time, the oxygen concentration would also approach its equilibrium value. Therefore, it was possible to verify the oxygen

concentration by measuring the Mg concentration.

The experimental data of Mg concentration as a function of time at 900℃, 1000℃ and 1100℃ are shown in Fig. 4.7, 4.8, and 4.9, respectively. The corresponding amounts of starting materials are also presented in Table 4.1, 4.2, and 4.3, respectively.

Fig. 4.3 The side view and top view of a dry $MgO/MgAl_2O_4$ preform casted inside a commercial MgO crucible before sintering

Fig. 4.4 The side view and top view of a sintered high-purity $MgO/MgAl_2O_4$ crucible prepared by gelcasting

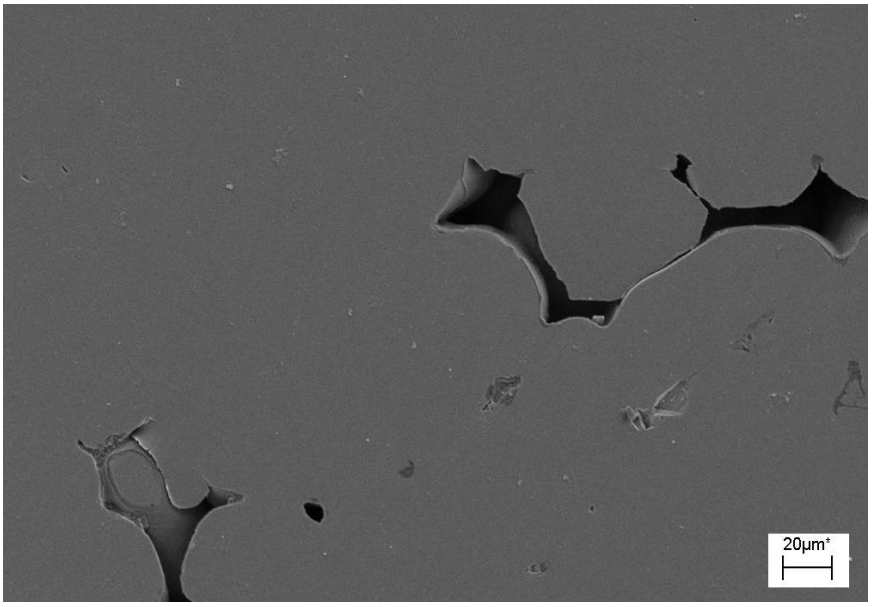

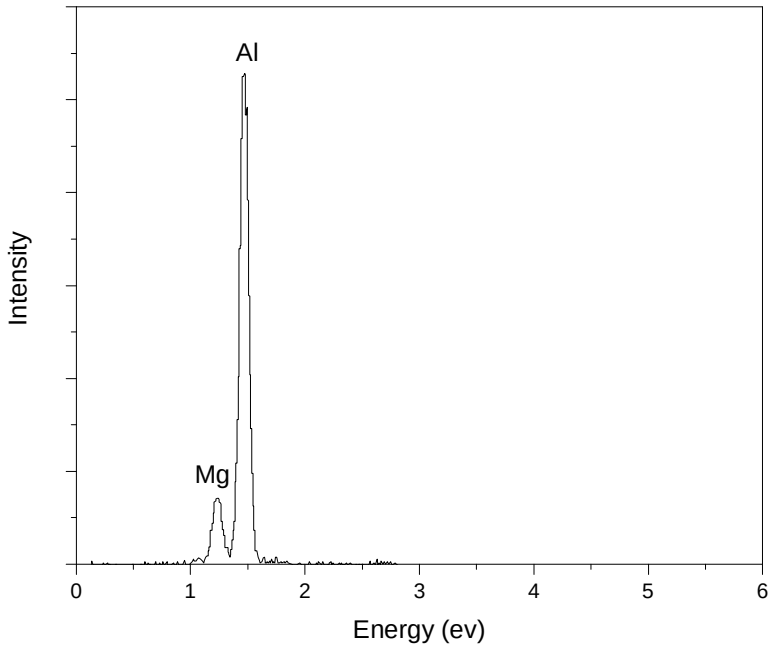

Fig. 4.5 The BSE image and EDS spectrum of the Mg-Al alloy with 7 at% Mg that was contained in a gelcasting $MgO/MgAl_2O_4$ crucible for 3 days at 1100°C

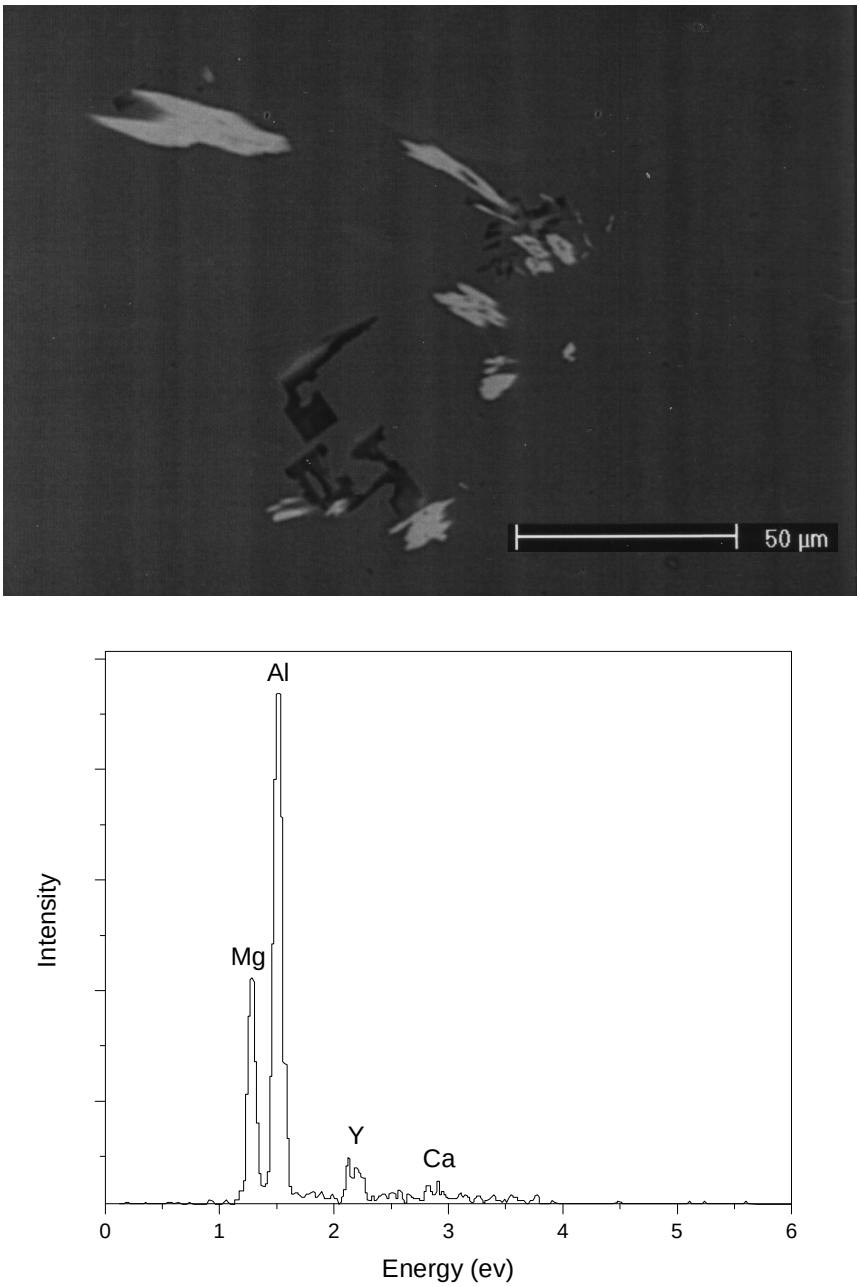

Fig. 4.6 The BSE image and EDS spectrum of the Mg-Al alloy with 7 at% Mg that was contained in a commercial MgO crucible for 3 days at 1100°C

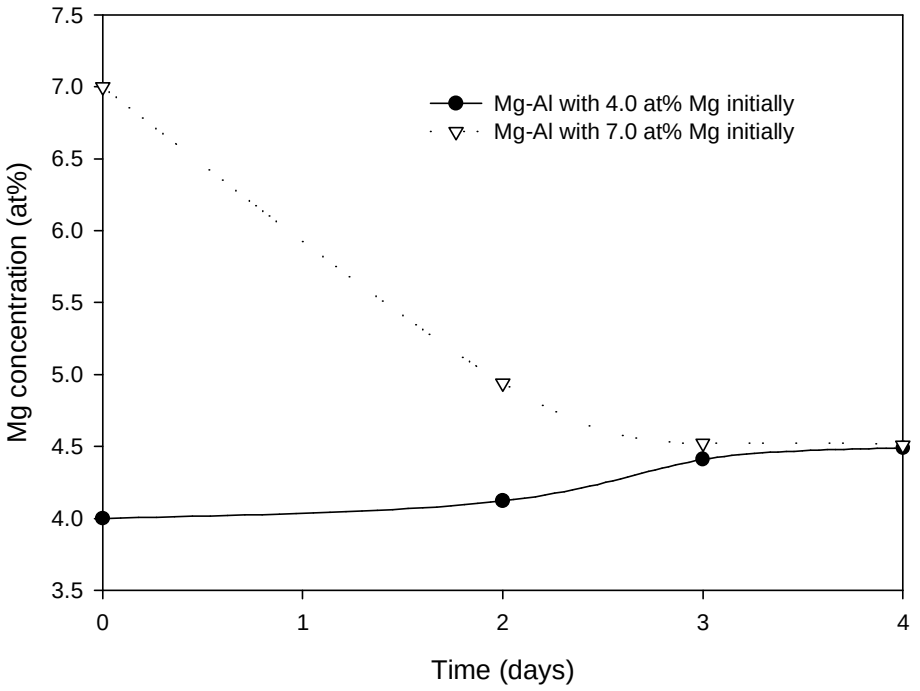

Fig. 4.7 A plot of Mg concentration in the Mg-Al-MgO-$MgAl_2O_4$ mixture as a function of time at 900°C

Table 4.1 The amount of materials used for each run at 900°C

Material	Amount (gram)	Amount (gram)
Mg	1.36	0.75
Al	20.02	20.01
MgO	1.01	1.32
$MgAl_2O_4$	1.92	1.01

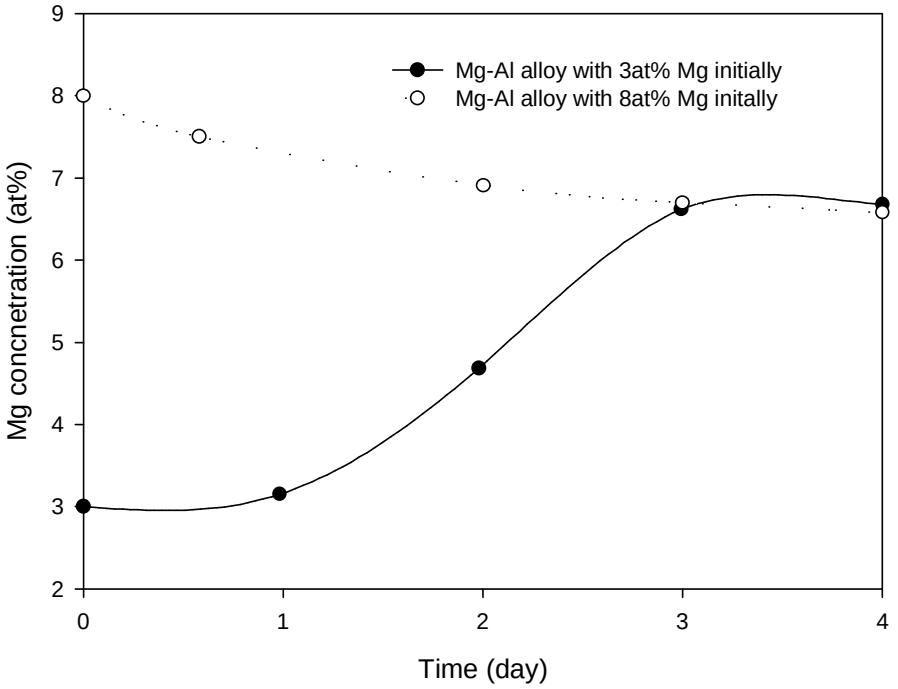

Fig. 4.8 A plot of Mg concentration in the Mg-Al-MgO-$MgAl_2O_4$ mixture as a function of time at 1000°C

Table 4.2 The amount of materials used for each run at 1000°C

Material	Amount (gram)	Amount (gram)
Mg	1.57	0.56
Al	20.03	20.05
MgO	1.01	3.20
$MgAl_2O_4$	1.32	1.04

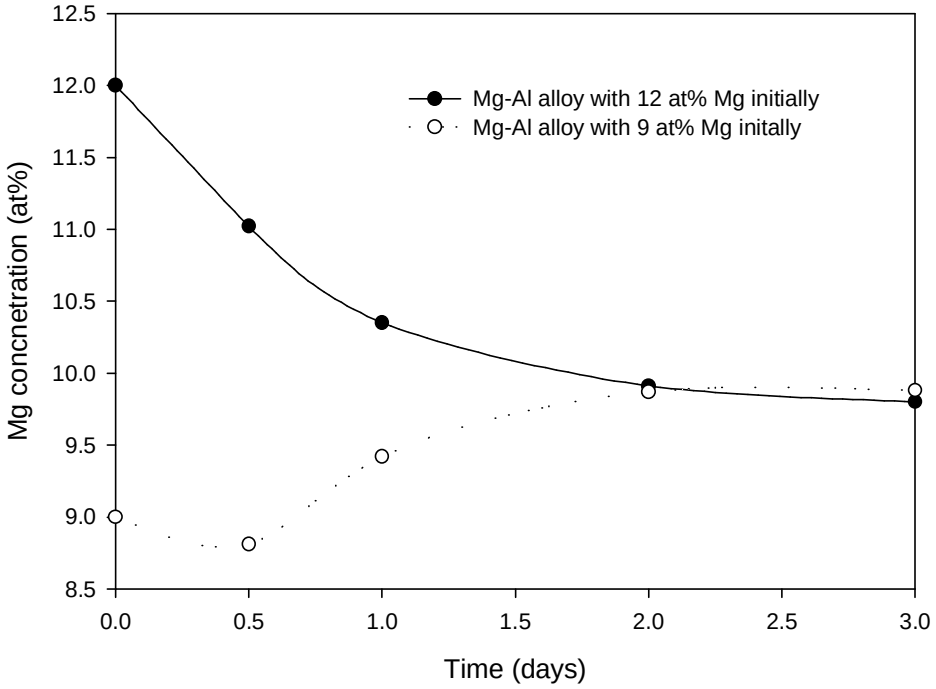

Fig. 4.9 A plot of Mg concentration in the Mg-Al-MgO-$MgAl_2O_4$ mixture as a function of time at 1100°C

Table 4.3 The amount of materials used for each run at 1100°C

Material	Amount (gram)	Amount (gram)
Mg	2.4564	1.7815
Al	20	20
MgO	1.0	2.7
$MgAl_2O_4$	3.3	1.0

4.4 Discussion

Oxygen can dissolve into Mg-Al melts to form Mg-Al-O ternary liquid solutions. There are concerns about the influence of such dissolved oxygen on the initial kinetics of spinel formation during the incongruent reduction of alumina. Traces of super-saturated oxygen in the melts may lead to the formation of MgO. Although this temporary MgO layer may be only about several atomic layers thick, it would affect the initial formation of spinel. In addition, even at a nanometric scale, it may set the activity of MgO at unity at the solid-liquid interface, thus making the diffusion driving force totally different at the nucleation stage [108].

In order to obtain a well-controlled nucleation and growth condition for spinel, it is necessary to control the oxygen concentration below a certain limit at a given temperature. Although experimental data for the exact values of oxygen solubility in Mg-Al melts are not available, the saturation concentrations of oxygen in the Mg-Al-O melts at different temperatures can be predicted from available thermodynamic data.

In this work, the liquid phase is treated by the two sublattice ionic model. One sublattice contains charged cations and the other oxygen ions and charged vacancies. The phase model can be represented as:

$$(Mg^{2+}, Al^{3+})_p (O^{2-}, Va)_q$$

where p and q are the numbers of sites on the respective sublattice, and vary with composition to maintain electroneutrality. The interaction parameters of vacancies with any other species present in the liquid phase are set to zero due to the lack of literature data. According to this assumption, the liquid phase of Mg-Al-O can be evaluated from the combination of the thermodynamic descriptions for the three binary systems: Mg-O

[32], Al-O [35] and Mg-Al [41], which were already assessed in the literature and their results were accepted in this study.

The spinel phase can be described by the compound energy model so that it can dissolve a certain amount of MgO and Al_2O_3. According to this model, the formula for spinel phase can be written as [46]:

$$(Al^{3+}, Mg^{2+})_1(Al^{3+}, Mg^{2+}, Va)_2(Va, Mg^{2+})_2(O^{2-})_4$$

All the data necessary for describing the spinel phase can be directly taken from the work of B. Hallstedt [46], who assessed the MgO-Al_2O_3 binary system.

Al_2O_3 and MgO are treated as stoichiometric phases in that their abilities to adopt other cation-to-anion ratios at the temperatures of interest are negligible. The gas phase, for simplicity, is modeled as an ideal gas that only contains O_2 species.

The calculated isothermal section of the Mg-Al-O ternary system from the thermodynamic parameters mentioned above at 1000°C is presented in Fig. 4.10. The Mg-Al side of the Mg-Al-O isothermal section at 1000°C is enlarged and shown in Fig. 4.11. From Fig. 4.11, the oxygen solubilities can be directly obtained in this plot at 1000°C. Such plots can also be constructed for other temperatures and are of great help in analyzing the chemical interactions between Al_2O_3 and Mg-Al melts.

Based on the thermodynamic data of Mg-Al melts from different authors and the published thermodynamic information on Mg-O, Al-O, and $MgAl_2O_3$, the equilibrium compositions of Mg and oxygen in the oxygen-controlled alloys at different temperatures are calculated and listed in Table 4.4. As can be seen, the results of the calculated oxygen concentrations are almost the same for the same temperature, but there are some deviations for the calculated Mg concentrations.

The experimental results illustrated in Fig 4.7, 4.8, and 4.9 show that the initial Mg concentrations were different, and the convergence of the curves led to a equilibrium state when the reaction time was long enough. A comparison of the calculated Mg concentrations and the experimental results at different temperatures are presented in Fig 4.12. The consistency of the data between the experimental results and those calculated from the available thermodynamic data also indicates that the equilibrium was established for each temperature of interest. The 900°C and 950°C experimental results are most consistent withY. Zuo's thermodynamic parameters, although the experimental results at 1100°C are closest to the calculated results from Z. Moser's thermodynamic data. As a consequence, Y. Zuo's thermodynamic parameters for the Mg-Al melts were used in the following calculations.

.

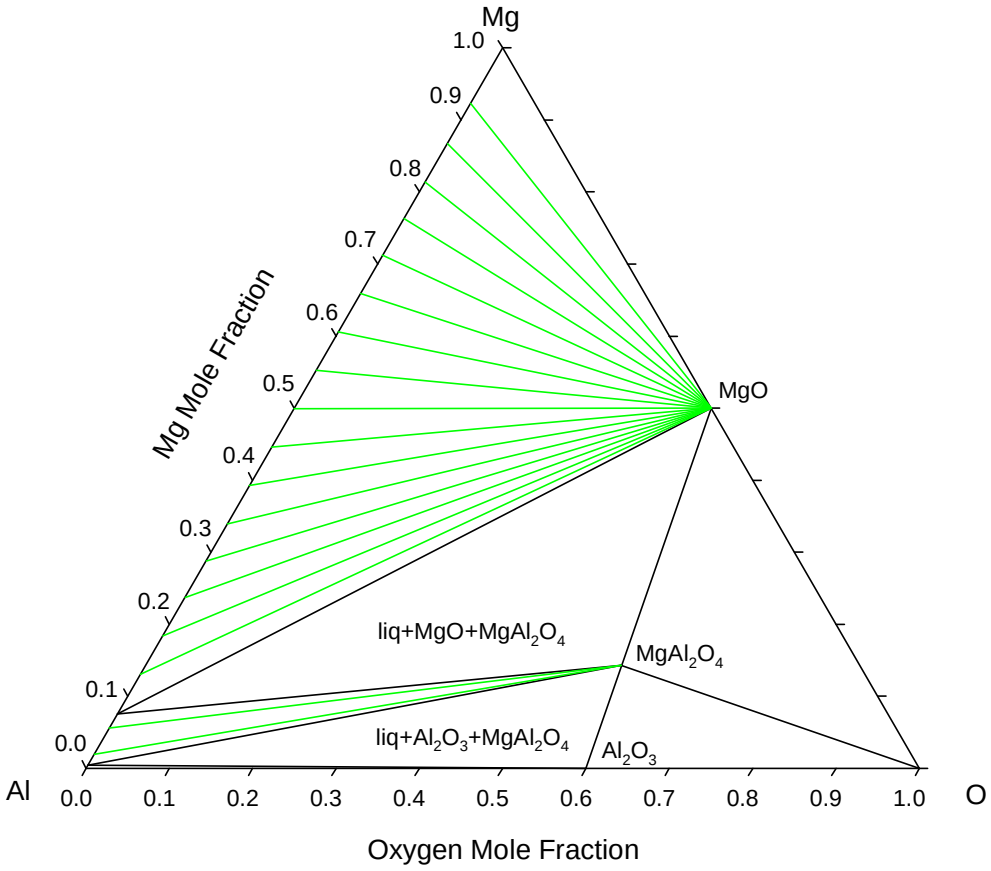

Fig. 4.10 The calculated isothermal section of the Mg-Al-O ternary system at 1000°C

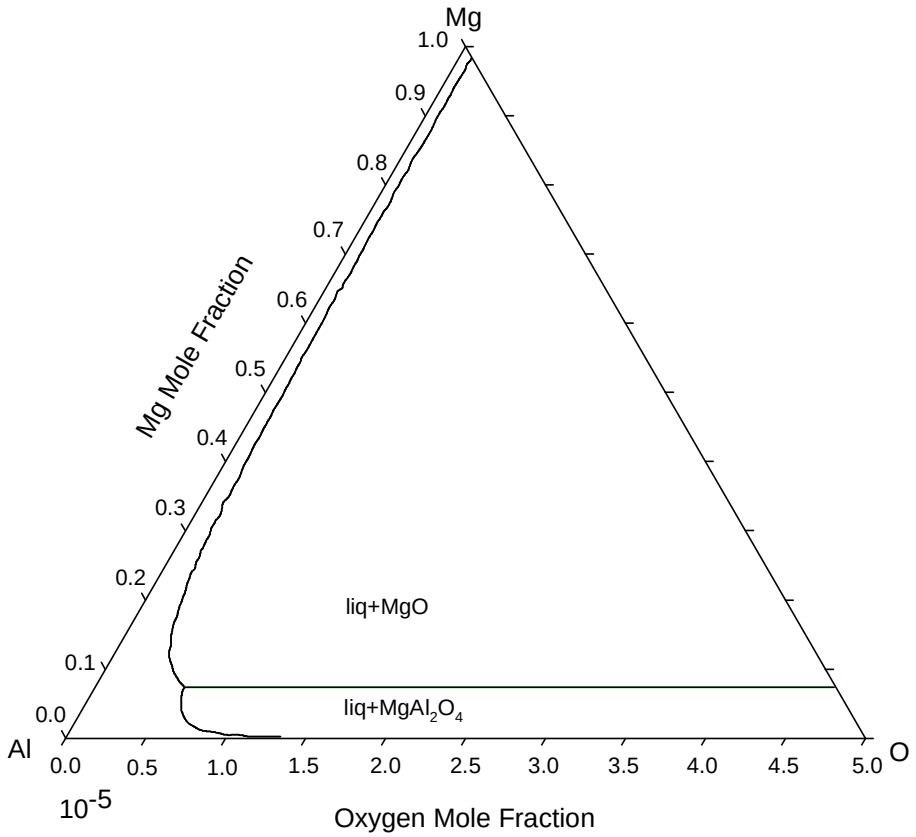

Fig. 4.11 The enlarged Al-Mg side of the isothermal section of the Mg-Al-O ternary system at 1000°C

Table 4.4 The theoretical Mg equilibrium concentrations calculated from thermodynamic parameters from various authors at different temperatures

Thermodynamic parameters	Temperature (°C)	x_{Mg}	x_O
J. Murry [38]	900	6.96E-2	2.44E-6
	1000	8.8E-2	5.47E-6
	1100	10.83E-2	1.10E-5
D. Ludecke [39]	900	9.21E-2	2.35E-6
	1000	11.61E-2	5.21E-6
	1100	13.99E-2	1.04E-6
N. Saunders [40]	900	6.99E-2	2.46E-5
	1000	8.87E-2	5.52E-6
	1100	10.89E-2	1.11E-5
Y. Zuo [41]	900	5.82E-2	2.46E-6
	1000	7.32E-2	5.53E-6
	1100	8.98E-2	1.11E-5
Z. Moser [42]	900	6.32E-2	2.47E-6
	1000	7.95E-2	5.56E-6
	1100	9.77E-2	1.12E-5

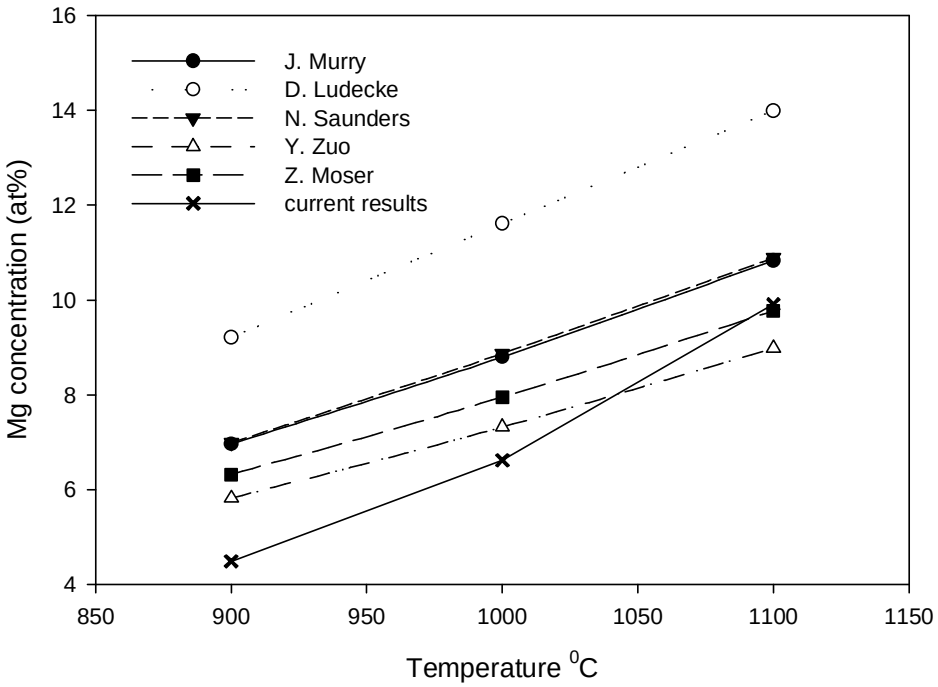

Fig. 4.12 A comparison of the experimental and theoretical Mg equilibrium concentrations at various temperatures

CHAPTER V

THE KINETICS OF SPINEL FORMATION

5.1 Introduction

The generation of spinel during the incongruent reduction of alumina involves two simultaneous processes: spinel formation and dissolution. These two parallel processes are independent of each other, and therefore whichever is faster will control the overall kinetics.

In principle, the spinel formation process can be viewed as a series of consecutive steps, involving the oxidation/reduction at the $MgAl_2O_4$-melt interface, the solid-state diffusion through the spinel layer and the subsequent chemical reaction at the Al_2O_3-$MgAl_2O_4$ interface. The electron exchange is so fast at high temperatures that the oxidation/reduction is not likely to be the rate-limiting step. Accordingly, the spinel formation may be rate-limited by the chemical reaction, by the diffusion in spinel, or even by a combination of the two.

The dissolution of a compound in a melt usually involves two consecutive steps: dissociation of the compound into ions or atoms at the solid-liquid interface and the subsequent diffusion of these ions or atoms away from the interface into the melt. As these are consecutive processes, the slower step will control the whole dissolution process. Consequently, the dissolution process may be rate-limited by the interface dissociation, by the diffusion in the melt, or even by a combination of the two.

The rate-limiting steps in the formation of spinel as a continuous layer on sapphire surfaces during incongruent reduction of sapphire in Mg-Al-based melts were investigated, and are presented in this chapter.

5.2 Experimental Procedure

When alumina is immersed into a Mg-Al melt, $MgAl_2O_4$ can be formed under an appropriate condition by the following reaction:

$$4Al_2O_3 + 3\{Mg\} = 3MgAl_2O_4 + 2\{Al\} \quad (5\text{-}1)$$

Because an Al-rich melt is heavier than a Mg-rich melt, natural convection may be induced by a density gradient in the melt. To have a well-controlled flow pattern, a configuration adopted to meet the above specification for the experiments is schematically illustrated in Fig. 5.1. A sapphire wafer was hung from a horizontal MgO rod, whose vertical position could be adjusted so that the sapphire wafer was completely immersed into the melt when the alloy became liquid. The whole assembly was placed inside a steel pipe which was then filled with argon and sealed by welding. The sealed steel tube was subjected to the subsequent reaction under a flowing argon atmosphere in a vertical furnace as shown in Fig. 3.1.

Much attention was taken in the preparation of sapphire wafers to ensure the obtainment of samples with a uniform thickness. Sapphire in the form of rods (Crystal System Inc, MA, (0001) and $(01\bar{1}2)$ orientation were purchased) was subjected to cutting, lapping and a series of polishing steps. The tool for lapping was diamond-embedded disks (His Glassworks Inc, NC) with particle sizes ranging from 110 microns to 30 microns. Both sides of each wafer were lapped to produce two relatively parallel surfaces with a maximum thickness deviation of about 15 microns across the whole

sapphire wafer surface. The lapped sapphire wafers were then polished to 0.5 micron finish by a series of diamond pastes, and a thickness deviation of about 2 microns was finally obtained. The detailed polishing procedure can be found in Appendix 1. A hole with a diameter of 0.80 mm was then drilled through the wafer to accommodate a 0.75 mm diameter MgO suspension rod.

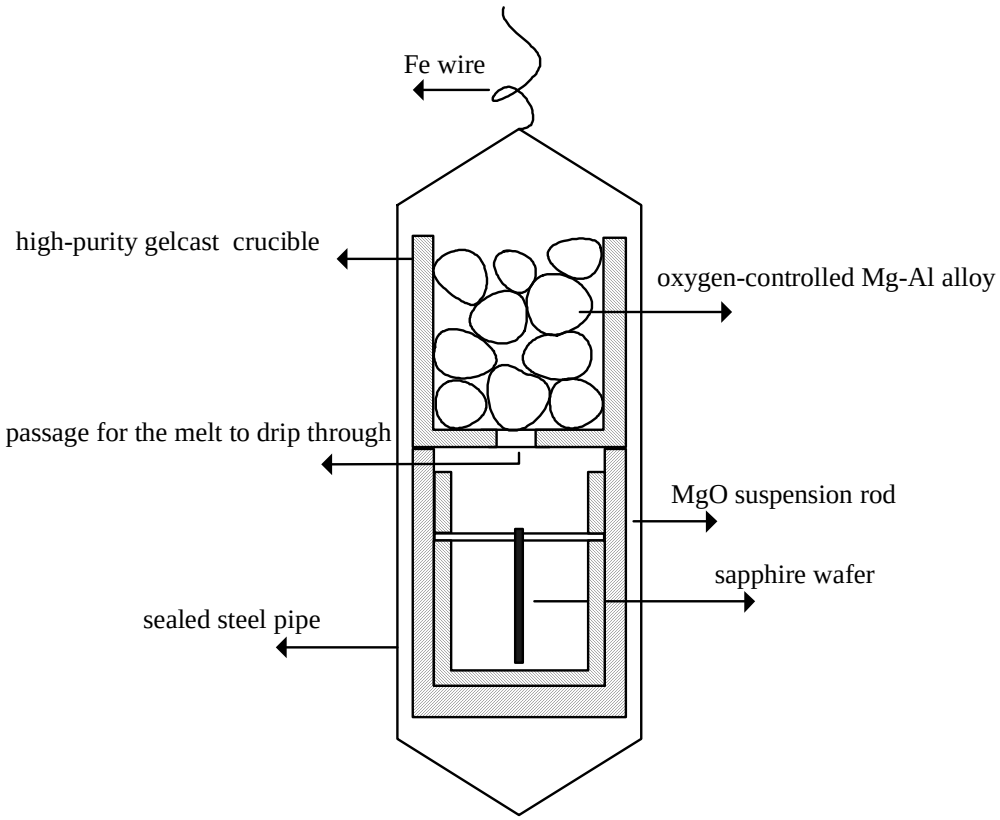

Fig. 5.1 Schematic drawing for the reaction setup

To avoid MgO formation, the oxygen-controlled alloys prepared at a lower temperature were used for incongruent reaction at a higher temperature. That is to say, oxygen-controlled alloys prepared at 900°C, 1000°C and 1100°C were used to form spinel at 1000°C, 1100°C and 1200°C, respectively.

Dissolution of the retained Mg-Al alloys on the surfaces of reacted sapphire samples was required to allow for high precision thickness change measurements. The ideal etchant has to exhibit a fast etching rate for Mg-Al alloys, but no attack of the MgO or $MgAl_2O_4$. A 10 wt% aqueous NaOH solution was found to be a good selective etchant for this purpose.

For some characterization methods, the whole reaction assembly was inverted at high temperatures so that the liquid alloy could flow out of the reaction chamber, leaving the sample sapphire surface almost free of solidification metals. The whole reaction assembly could also be quenched into water, allowing the liquid alloy to solidify around the sample so that the concentration gradient in the melt around the sample surface could be investigated.

The reacted sapphire wafers, with dimensions of about 10 mm long, 5 mm wide and 0.5 mm thick, were sectioned by a diamond blade, mounted in epoxy, and polished down to 0.5 microns with a series of SiC-embedded papers and diamond pastes. Polystyrene spheres with a mean size of 9.89 microns prepared under a gravity-free condition were used as SEM (Scanning Electron Microscopy) reference standards (ASTM certified, available from Electron Microscopy Sciences Company, PA) for measurement of spinel layer thickness. Ten measurements were made on each cross section, and four cross sections were used for each reacted sample. A micrometer with 1-

micron resolution (342-711-30, Mitutoyo, Japan) was used to characterize the sample-thickness change as a function of position before and after the experiments. TEM (Transmission Electron Microscopy) was used to investigate spinel microstructures. XPS (X-ray photoelectron spectroscopy) was employed in our study for concentration gradient measurements in spinel and Mg-Al alloys.

5.3 Results

5.3.1 Polished-Sample Characterization

Polished sapphire wafers, with dimensions of about 10 mm long, 5 mm wide and 0.5 mm thick, were examined by SEM prior to reaction with the Mg-Al melt to form spinel. SEM inspection was performed on a Au-coated sapphire wafer using a SEM (LEO1530, Leo Electron Microscopy Ltd, UK). The surface morphology of a polished sapphire wafers is presented in Fig. 5.2, and the image of its cross section is presented in Fig. 5.3.

5.3.2 Sample-Thickness-Change Measurement

To characterize sample thickness change as a function of position, the sapphire wafer surface was divided into a grid with the spacing of 1 mm between grid points, as illustrated in Fig. 5.4. The measurements on each grid point were performed by a micrometer, with 1-micron resolution, before and after the experiments. In this study, sample-thickness-change measurements were conducted for experiments at 1000°C, 1100°C, and 1200°C for 168 hours, 62 hours and 30 hours for two sapphire orientations, and the results are presented in Tables 5.1-5.6, respectively.

5.3.3. Phase Identification by XRD

The reacted sapphire wafers with two different orientations were subjected to XRD identification to verify the presence of $MgAl_2O_4$ and the absence of MgO, and the results for the samples reacted at 1100°C for 4.5 hours are presented in Fig. 5.5 and Fig. 5.6, respectively. As can be seen, the interface layer was composed of $MgAl_2O_4$ phase only.

5.3.4 Spinel-Layer-Thickness Measurement

The SEM image of polystyrene spheres used as the SEM standard is presented in Fig. 5.7. The BSE image of the cross section of a sample reacted at 1100°C for 62 hours is illustrated in Fig 5.8, where a continuous and uniform spinel layer was formed on the sapphire surface. In order to examine the spinel layer thickness more accurately, X-ray mapping and image analysis were used. Fig. 5.9 shows the X-ray map of the spinel layer on a $(01\bar{1}2)$ sapphire wafer reacted at 1100°C for 62 hours. Fig. 5.10 represents the surface morphology of two kinds of sapphire wafers reacted at 1100°C for 62 hours.

The square of average $MgAl_2O_4$ layer thickness and its error bar showing 95% confidence interval are plotted in Fig 5.11, 5.12 and 5.13 as a function of time for the incongruent reaction at 1000°C, 1100°C, and 1200°C, respectively. Parabolic kinetic behavior was seen at these three temperatures and the kinetics were independent of sapphire orientations. Least square regression analyses were used to analyze these data, and the parabolic constants for sapphire wafers with two different orientations at different temperatures are presented in Table 5.7. The logarithms of parabolic constants are then plotted against the inverse of temperature (1/T) to determine the activation energy, as shown in Fig. 5.14. From this plot, the activation energy was found to be 195 kJ/mol.

Weight-change measurements for the reacted samples were also conducted. The square of weight change per unit area is plotted as a function of time at 1000°C, 1100°C, and 1200°C in Fig. 5.15-5.17 for two kinds of sapphire orientations, respectively. Each data point in these three plots was the average value of the measured results for two kinds of sapphire orientations. The plot of k_w, which is defined as $\Delta W^2 / t$, as a function of 1/T is given in Fig. 5.18, and an activation energy of 230 kJ/mol was obtained from this plot.

To evaluate the spinel layer thickness as a function of position, ten SEM images were taken in sequence from the sample top to the sample bottom on one cross section, and the procedure was repeated on various cross sections for each sample. The results for the experiments conducted at 1000°C, 1100°C and 1200°C for 168 hours, 62 hours and 30 hours are presented in Fig. 5.19-5.24 for two kinds of sapphire wafers, respectively. From these figures, the spinel layer thickness was observed to be independent of position.

5.3.5 XPS Depth Profile

An argon sputter ion gun was used to gradually remove the spinel layer whose thickness was about 8 microns on the (0001) sapphire wafer reacted at 1000°C for 7 days. The Ar ion beam spot size was 400 microns, the etching time was 6 minutes for each cycle, and the applied voltage was 5 kV. The intensity of the Mg2s peak was used to characterize the relative amount of Mg as a function of depth. The distribution of Mg against the sputter etching time in the $MgAl_2O_4$ layer is shown in Fig. 5.25. As can be seen, the Mg2s peak remained almost constant with increasing sputter etching time. After 4320 seconds, the Mg2s peak gradually decreased due to the presence of the Al_2O_3-$MgAl_2O_4$ interface.

An Mg-Al alloy film was taken from the surface of a reacted sapphire wafer which was embedded in a quenched alloy, and was subjected to XPS depth profile measurements from the surface which corresponded to the $MgAl_2O_4$-melt interface in the quenched assembly. The characterization condition was the same as that mentioned above except the spot size which was 100 microns in this case. The result illustrating the intensity of Mg2s as a function of sputtering cycles is shown in Fig. 5.26. It is seen that the intensity remained essentially constant.

5.3.5 TEM results

The cross section of (0001) and $(01\bar{1}2)$ sapphire wafers reacted at 1000°C for 7 days were subjected to TEM characterization, and the corresponding results are presented in Fig. 5.27 and Fig. 5.28, respectively. The spinel layer on the (0001) sapphire wafer is dense and continuous, while the reaction product on the $(01\bar{1}2)$ sapphire wafer shows a three-layer microstructure.

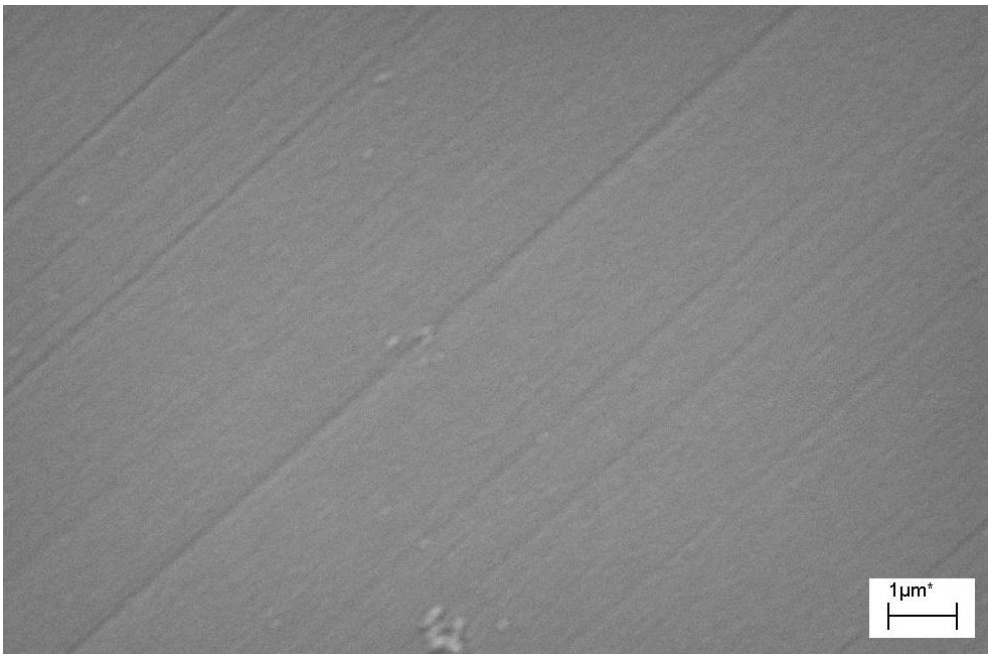

Fig. 5.2 The surface morphology of a polished sapphire wafer

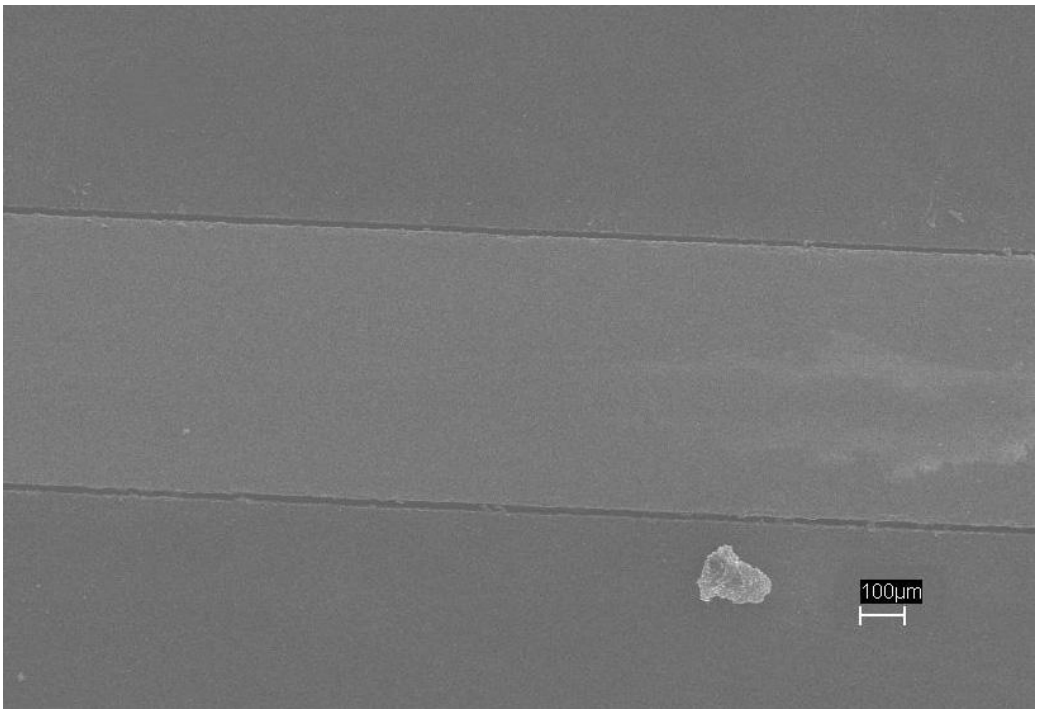

Fig. 5.3 The cross section of a polished sapphire wafer to show the uniform specimen thickness

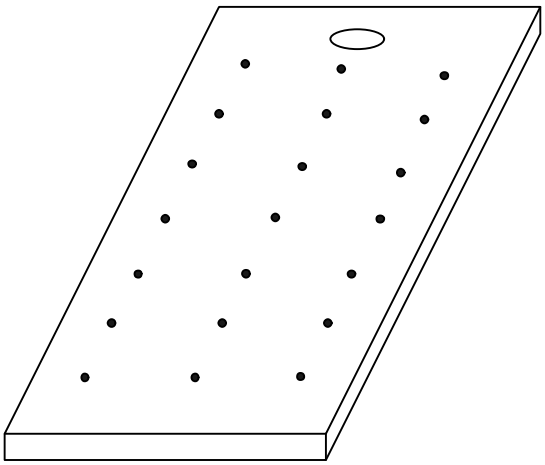

Fig. 5.4 The grid design for sample-thickness-change measurements

Table 5.1 The results of sample-thickness-change measurements by micrometer on the (0001) sapphire wafer reacted at 1000°C for 168 hours (the sample surface was divided into a grid with 7*3 uniformly-spaced nodes; the measurements were conducted on these nodes before and after the experiment)

Sample thickness on the nodes before experiment (mm)		
0.675	0.675	0.676
0.676	0.676	0.675
0.675	0.675	0.675
0.675	0.676	0.675
0.675	0.675	0.675
0.676	0.676	0.675
0.676	0.675	0.676

Sample thickness on the nodes after experiment (mm)		
0.679	0.680	0.680
0.680	0.680	0.679
0.679	0.679	0.679
0.679	0.680	0.679
0.679	0.680	0.680
0.680	0.680	0.680
0.679	0.679	0.680

Table 5.2 The results of sample-thickness-change measurements by micrometer on the $(01\bar{1}2)$ sapphire wafer reacted at 1000°C for 168 hours (the sample surface was divided into a grid with 7*3 uniformly-spaced nodes; the measurements were conducted on these nodes before and after the experiment)

Sample thickness on the nodes before experiment (mm)		
0.541	0.542	0.540
0.542	0.543	0.541
0.542	0.543	0.541
0.542	0.542	0.541
0.543	0.542	0.541
0.542	0.541	0.542
0.542	0.541	0.542

Sample thickness on the nodes after experiment (mm)		
0.545	0.545	0.544
0.546	0.547	0.545
0.545	0.546	0.545
0.546	0.545	0.545
0.545	0.545	0.545
0.546	0.545	0.546
0.546	0.546	0.546

Table 5.3 The results of sample-thickness-change measurements by micrometer on the (0001) sapphire wafer reacted at 1100°C for 62 hours (the sample surface was divided into a grid with 7*3 uniformly-spaced nodes; the measurements were conducted on these nodes before and after the experiment)

Sample thickness on the nodes before experiment (mm)		
0.614	0.614	0.615
0.614	0.615	0.614
0.614	0.614	0.614
0.614	0.615	0.615
0.616	0.615	0.614
0.615	0.615	0.614
0.616	0.614	0.614

Sample thickness on the nodes after experiment (mm)		
0.620	0.621	0.620
0.621	0.620	0.620
0.620	0.620	0.620
0.620	0.621	0.621
0.621	0.620	0.621
0.620	0.621	0.620
0.621	0.620	0.619

Table 5.4 The results of sample-thickness-change measurements by micrometer on the $(01\bar{1}2)$ sapphire wafer reacted at 1100°C for 62 hours (the sample surface was divided into a grid with 7*3 uniformly-spaced nodes; the measurements were conducted on these nodes before and after the experiment)

Sample thickness on the nodes before experiment (mm)		
0.452	0.453	0.452
0.453	0.452	0.453
0.453	0.453	0.454
0.453	0.453	0.452
0.452	0.452	0.453
0.452	0.452	0.452
0.452	0.452	0.453

Sample thickness on the nodes after experiment (mm)		
0.459	0.458	0.457
0.458	0.457	0.458
0.458	0.459	0.458
0.458	0.458	0.457
0.459	0.457	0.458
0.457	0.458	0.459
0.458	0.459	0.458

Table 5.5 The results of sample-thickness-change measurements by micrometer on the (0001) sapphire wafer reacted at 1200°C for 30 hours (the sample surface was divided into a grid with 7*3 uniformly-spaced nodes; the measurements were conducted on these nodes before and after the experiment)

Sample thickness on the nodes before experiment (mm)		
0.525	0.526	0.526
0.525	0.525	0.525
0.524	0.526	0.525
0.524	0.525	0.525
0.523	0.525	0.524
0.524	0.525	0.524
0.523	0.524	0.526

Sample thickness on the nodes after experiment (mm)		
0.530	0.531	0.531
0.530	0.530	0.531
0.529	0.531	0.530
0.529	0.530	0.530
0.529	0.530	0.530
0.529	0.530	0.529
0.528	0.529	0.531

Table 5.6 The results of sample-thickness-change measurements by micrometer on the $(01\bar{1}2)$ sapphire wafer reacted at 1200°C for 30 hours (the sample surface was divided into a grid with 7*3 uniformly-spaced nodes; the measurements were conducted on these nodes before and after the experiment)

Sample thickness on the nodes before experiment (mm)		
0.428	0.429	0.428
0.429	0.428	0.429
0.430	0.429	0.429
0.430	0.430	0.429
0.429	0.429	0.429
0.428	0.429	0.429
0.429	0.428	0.428

Sample thickness on the nodes after experiment (mm)		
0.433	0.434	0.435
0.434	0.434	0.434
0.434	0.434	0.434
0.435	0.435	0.435
0.434	0.434	0.434
0.424	0.434	0.434
0.434	0.435	0.433

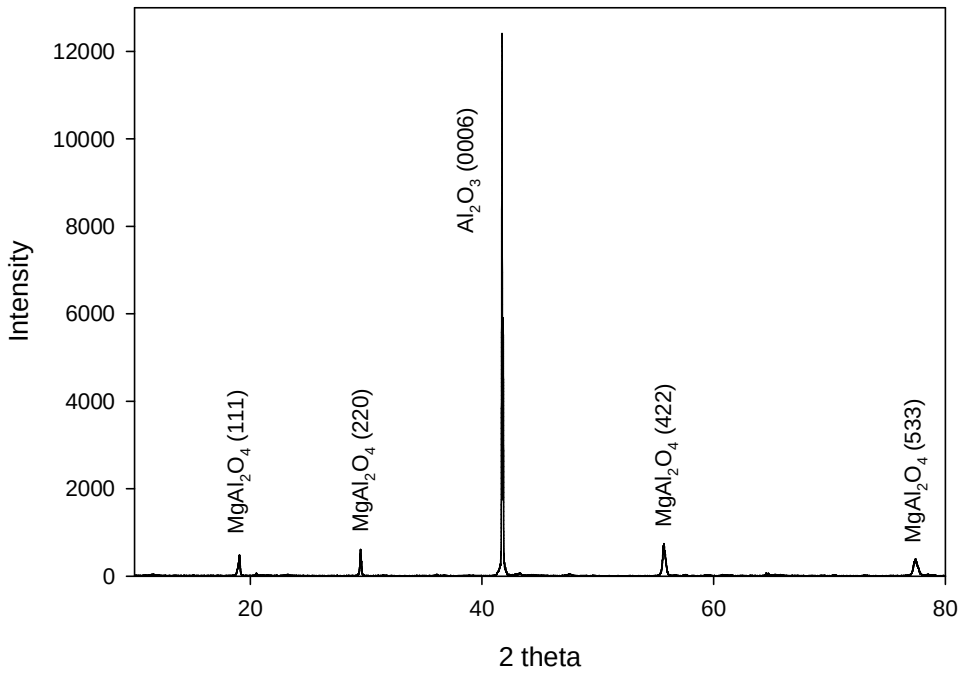

Fig. 5.5 The XRD pattern of the (0001) sapphire wafer reacted at 1100°C for 4.5 hours

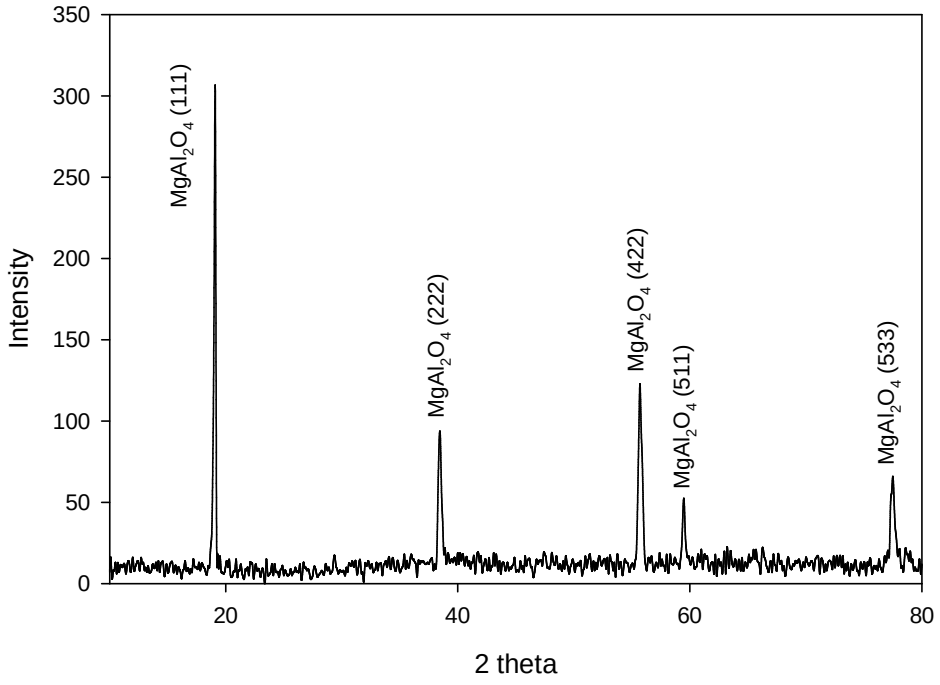

Fig. 5.6 The XRD pattern of the $(01\bar{1}2)$ sapphire wafer reacted at 1100°C for 4.5 hours

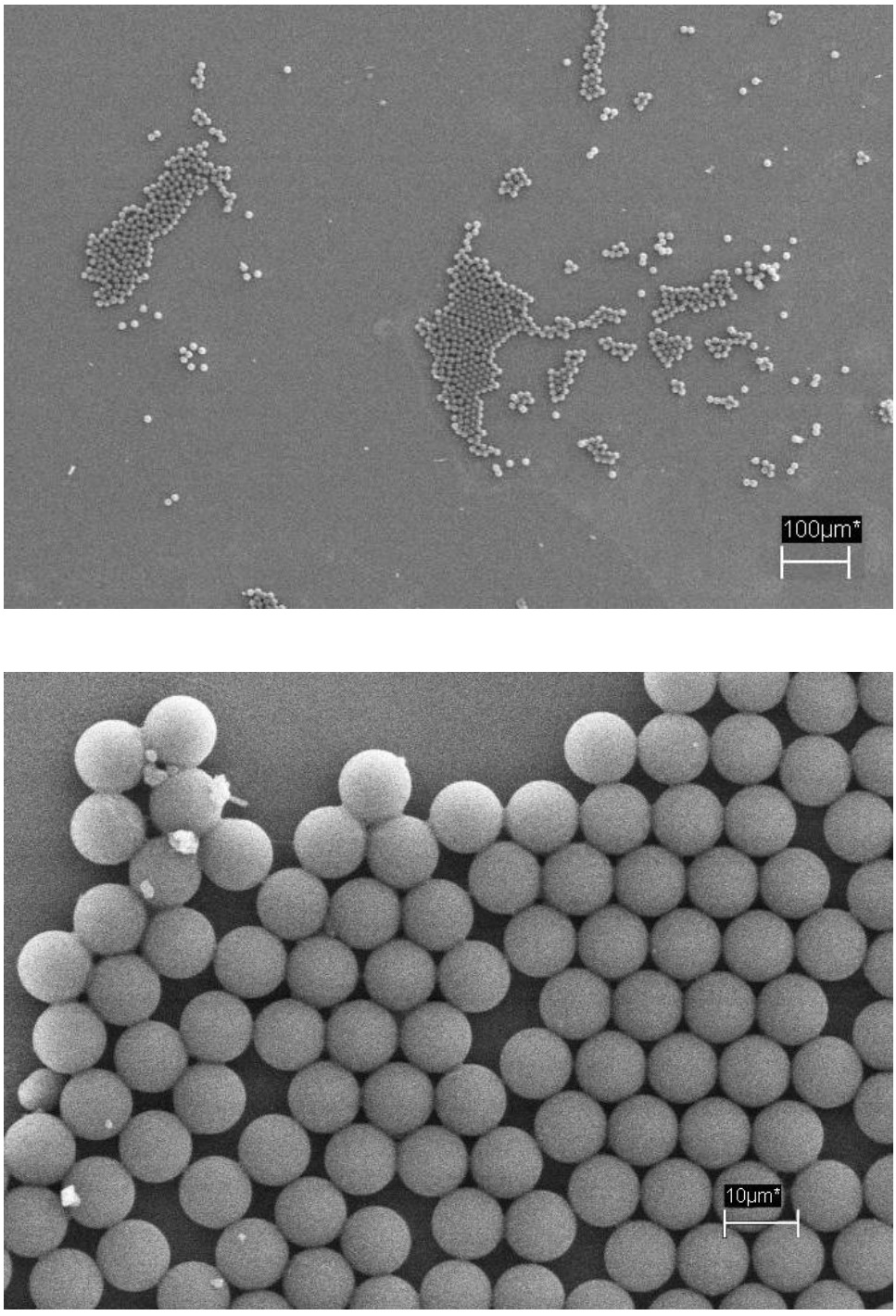

Fig. 5.7 The SEM images of polystyrene spheres used as the SEM standard

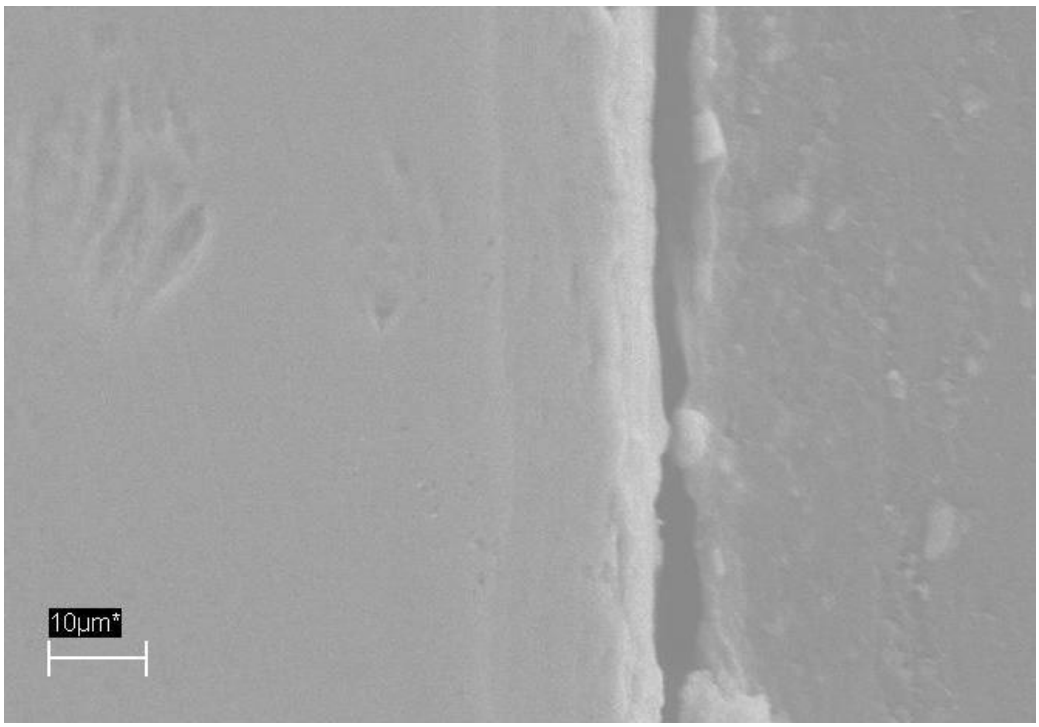

Fig. 5.8 The BSE image illustrating the spinel layer on the $(01\bar{1}2)$ sapphire wafer reacted at 1100°C for 62 hours

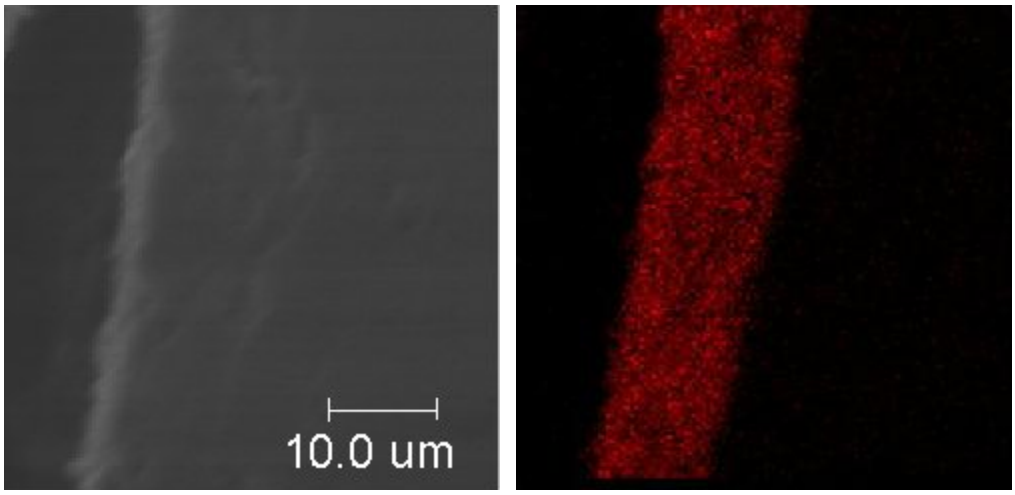

a) BSE image of a cross-section b) Mg X-ray map for the spinel layer

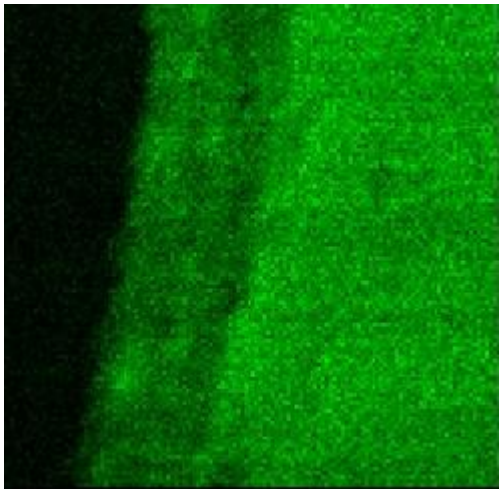

c) Al X-ray map for the spinel layer

Fig. 5.9 The SEM micrographs for the $(01\bar{1}2)$ sapphire wafer reacted at 1100°C for 62 hours

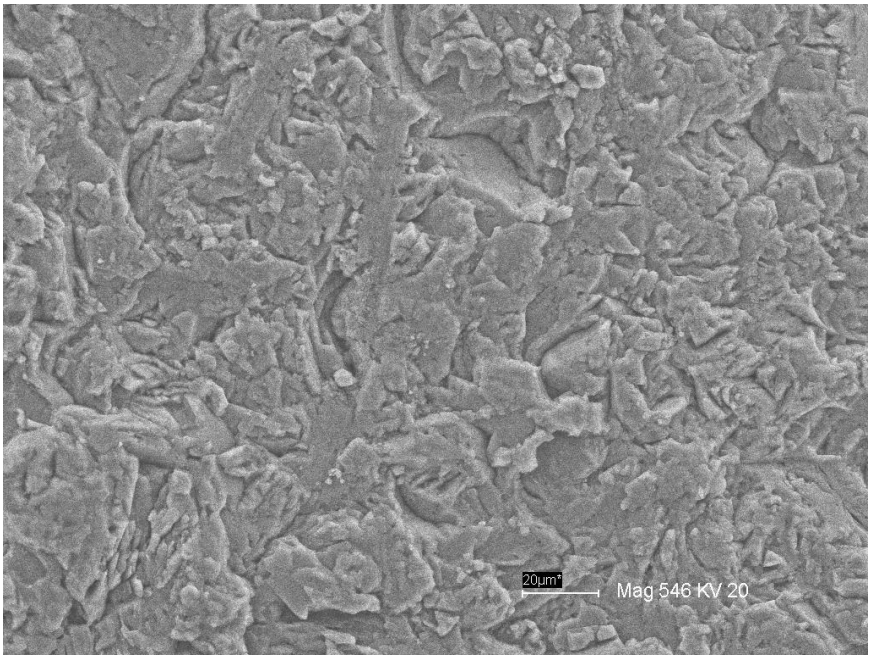

a:) (0001) sapphire wafer

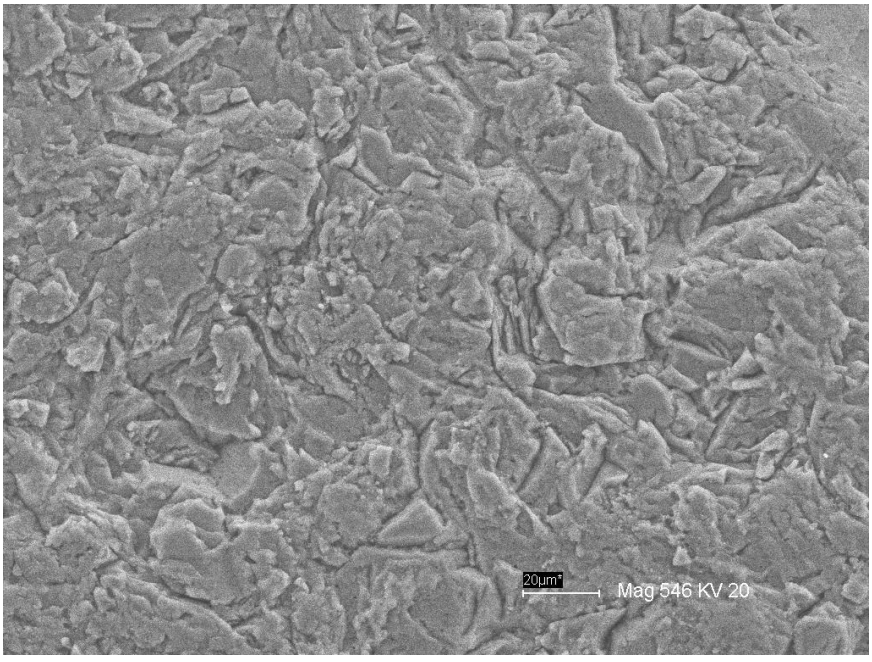

b:) $(01\bar{1}2)$ sapphire wafer

Fig.5.10 The surface morphologies of sapphire wafers reacted at 1100°C for 62 hours

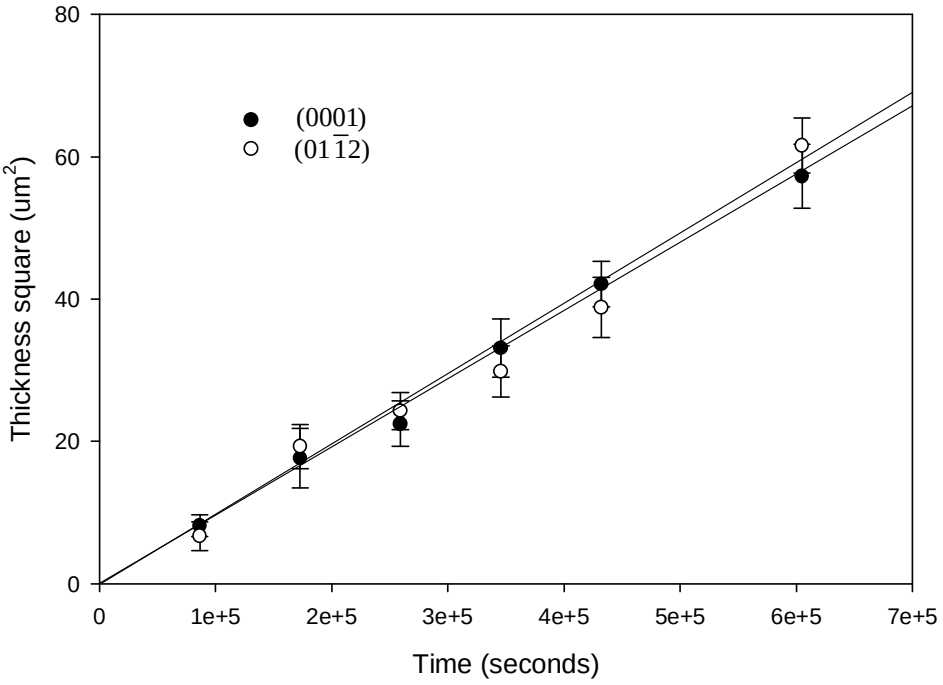

Fig. 5.11 A plot of square of spinel layer thickness with respect to time at 1000°C for two sapphire orientations.

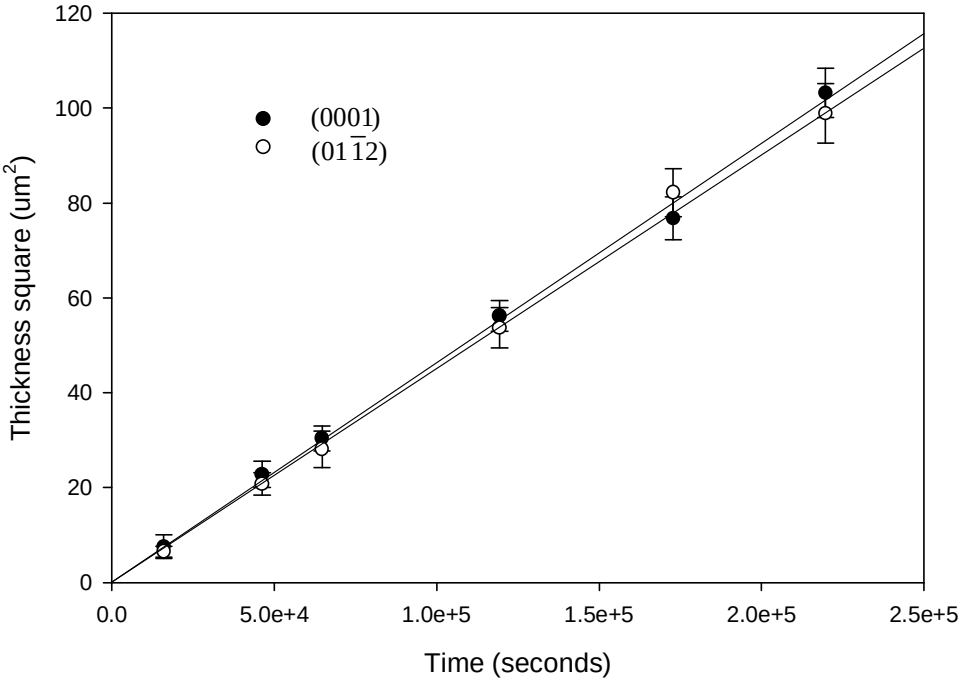

Fig. 5.12 A plot of square of spinel layer thickness with respect to time at 1100°C for two sapphire orientations.

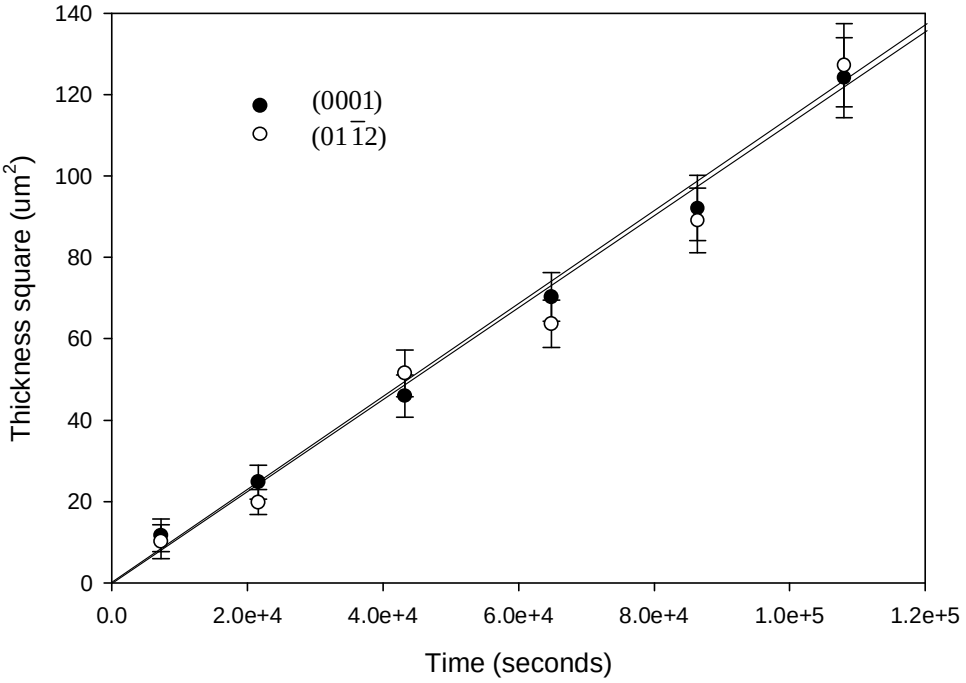

Fig. 5.13 A plot of square of spinel layer thickness with respect to time at 1200°C for two sapphire orientations.

Table 5.7 The experimental parabolic constants obtained by least square regression

Temperature (°C)	Parabolic constant (m^2/s)	
	(0001)	$(10\bar{1}2)$
1000	9.76e-17	9.62e-17
1100	4.71e-16	4.50e-16
1200	7.61e-16	7.58e-16

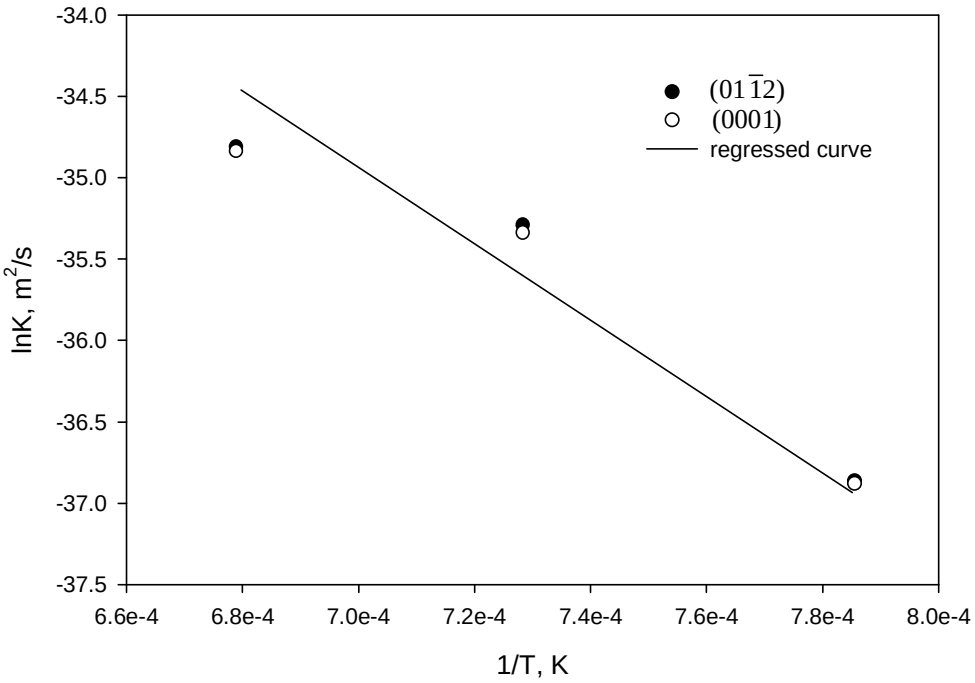

Fig. 5.14 A plot of ln(k) with respect to 1/T

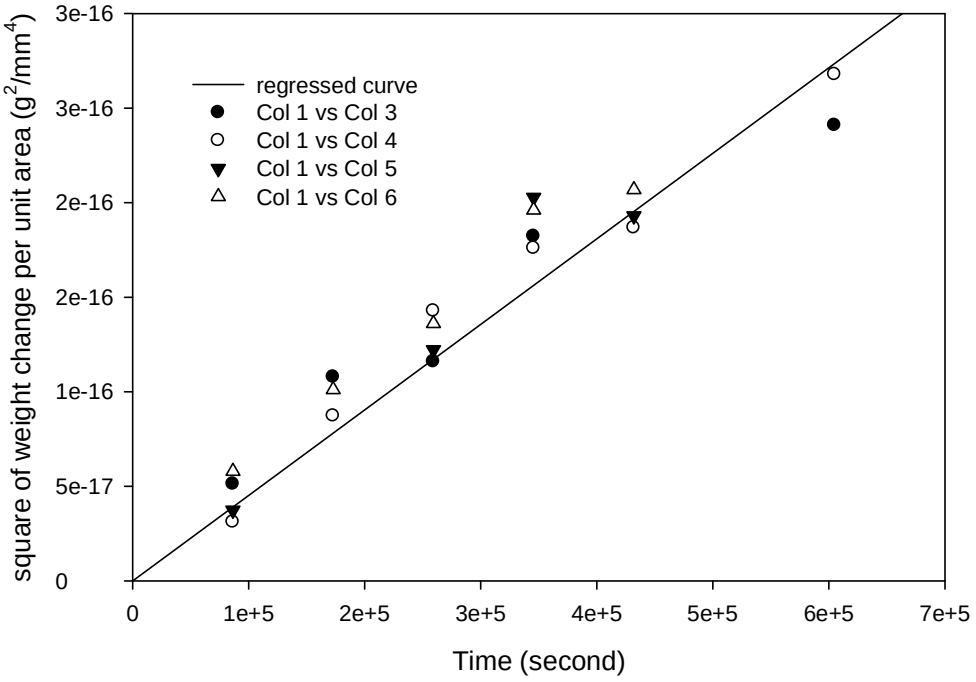

Fig. 5.15 A plot of square of weight change per unit area as a function of time at 1000°C

(Samples showing weight loss are not included in this plot)

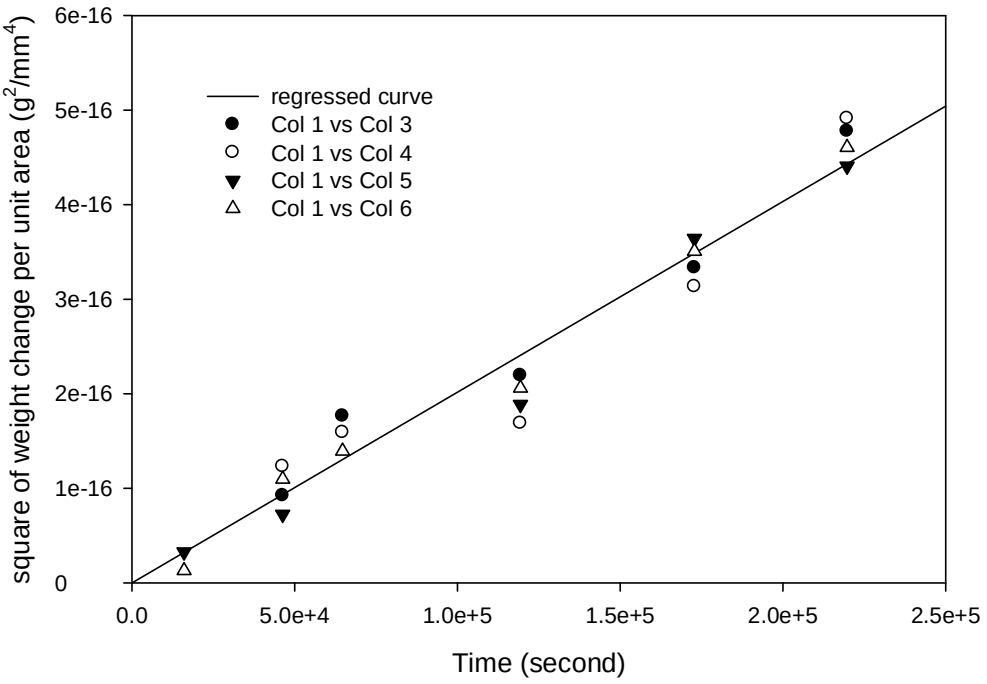

Fig. 5.16 A plot of square of weight change per unit area as a function of time at 1100°C

(Samples showing weight loss are not included in this plot)

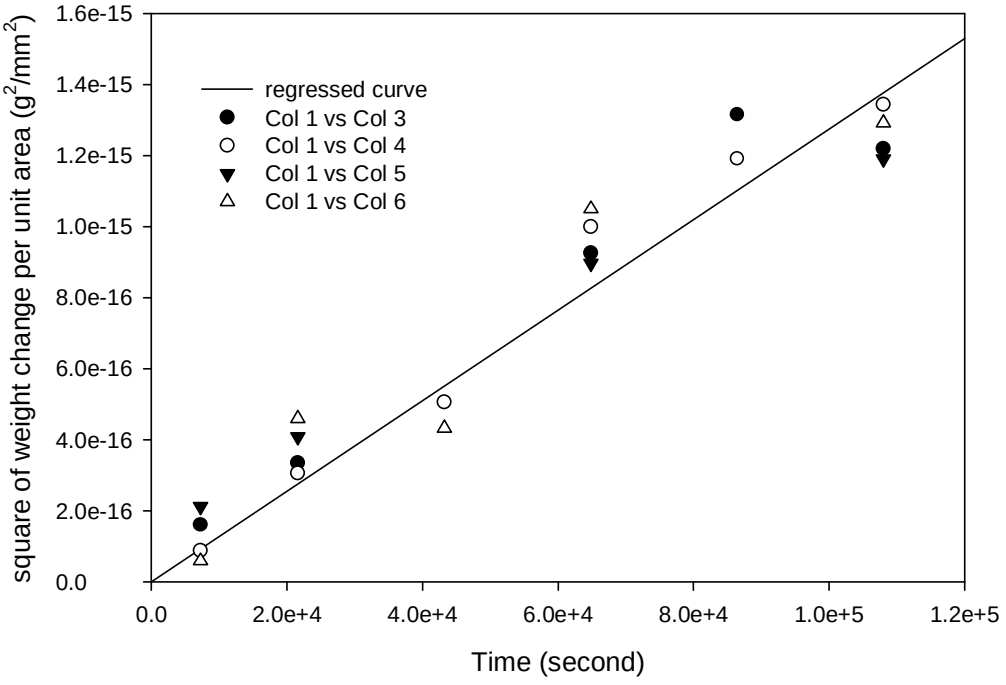

Fig. 5.17 A plot of square of weight change per unit area as a function of time at 1200℃

(Samples showing weight loss are not included in this plot)

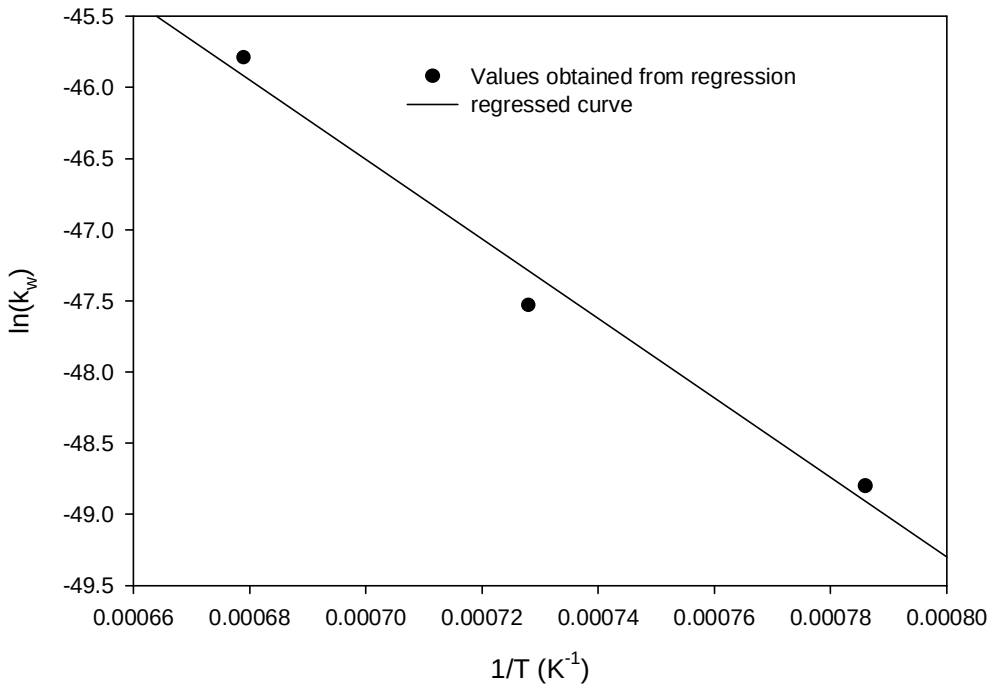

Fig. 5.18 A plot of $\ln(k_w)$ with respect to 1/T

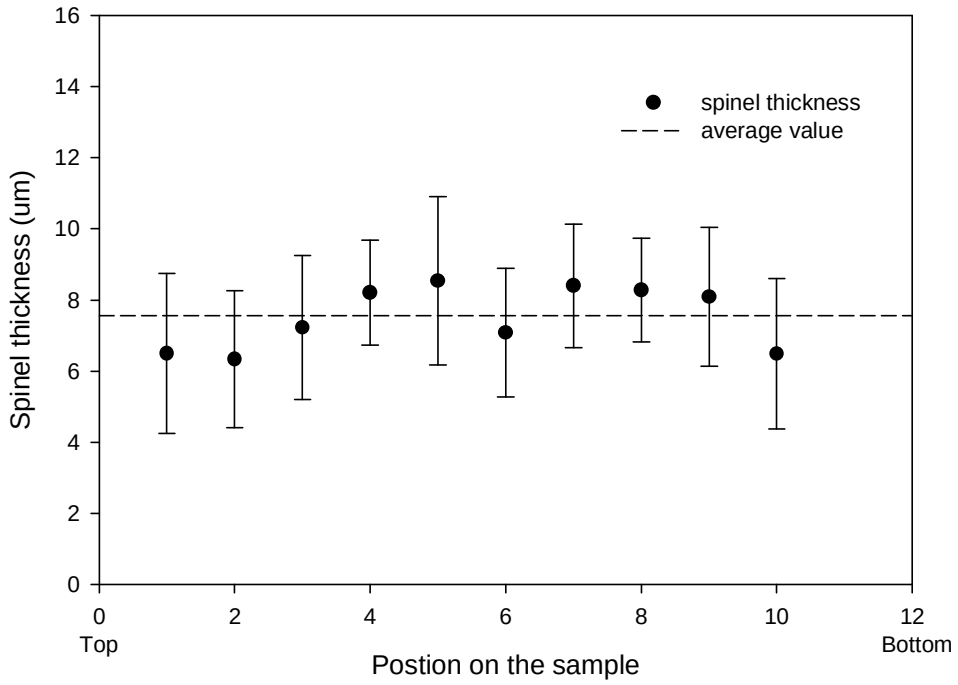

Fig. 5.19 A plot of spinel layer thickness on the (0001) sapphire wafer reacted at 1000°C for 168 hours as a function of position

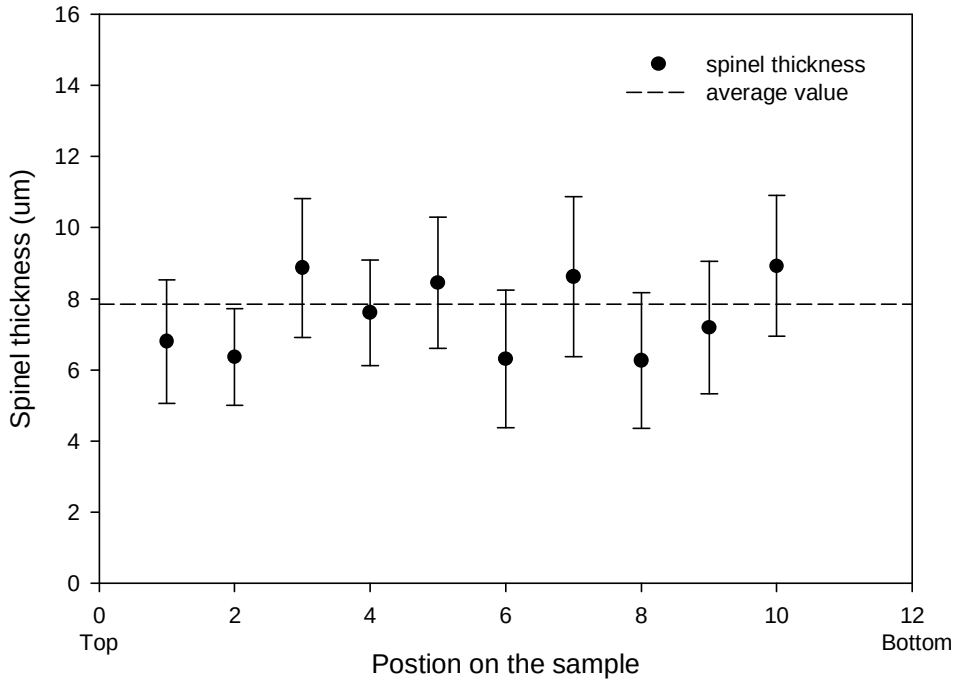

Fig. 5.20 A plot of spinel layer thickness on the $(01\bar{1}2)$ sapphire wafer reacted at 1000°C for 168 hours as a function of position

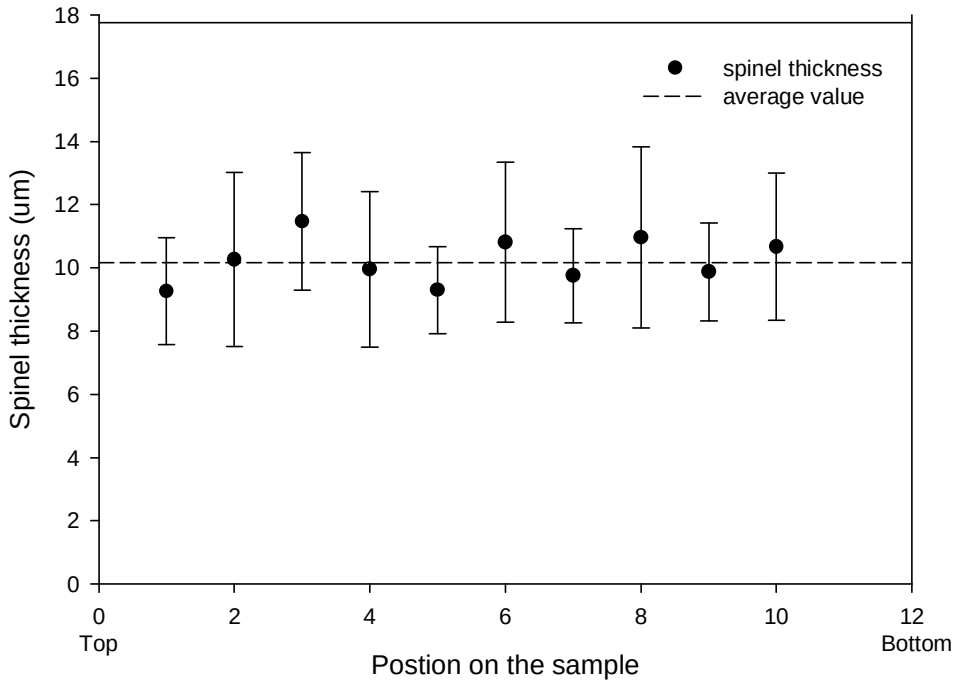

Fig. 5.21 A plot of spinel layer thickness on the (0001) sapphire wafer reacted at 1100°C for 62 hours as a function of position

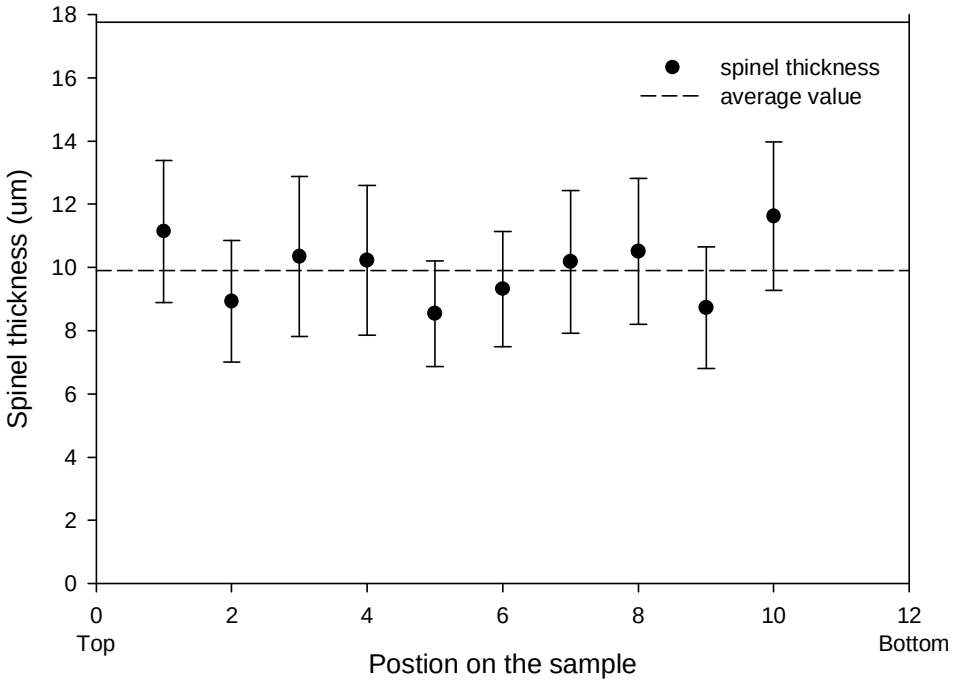

Fig. 5.22 A plot of spinel layer thickness on the $(01\bar{1}2)$ sapphire wafer reacted at 1100°C for 62 hours as a function of position

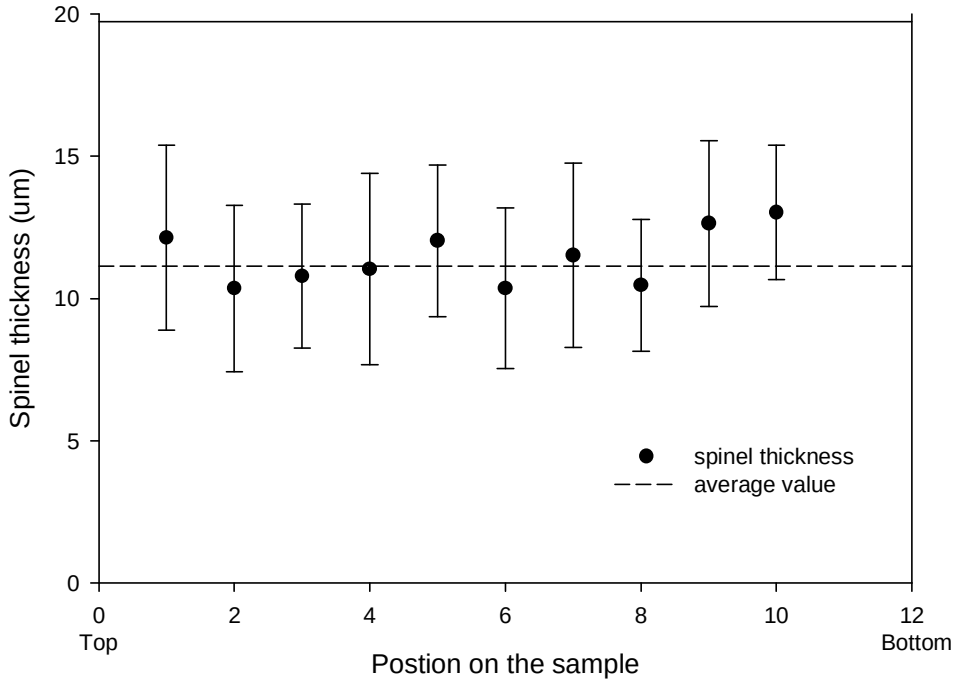

Fig. 5.23 A plot of spinel layer thickness on the (0001) sapphire wafer reacted at 1200°C for 30 hours as a function of position

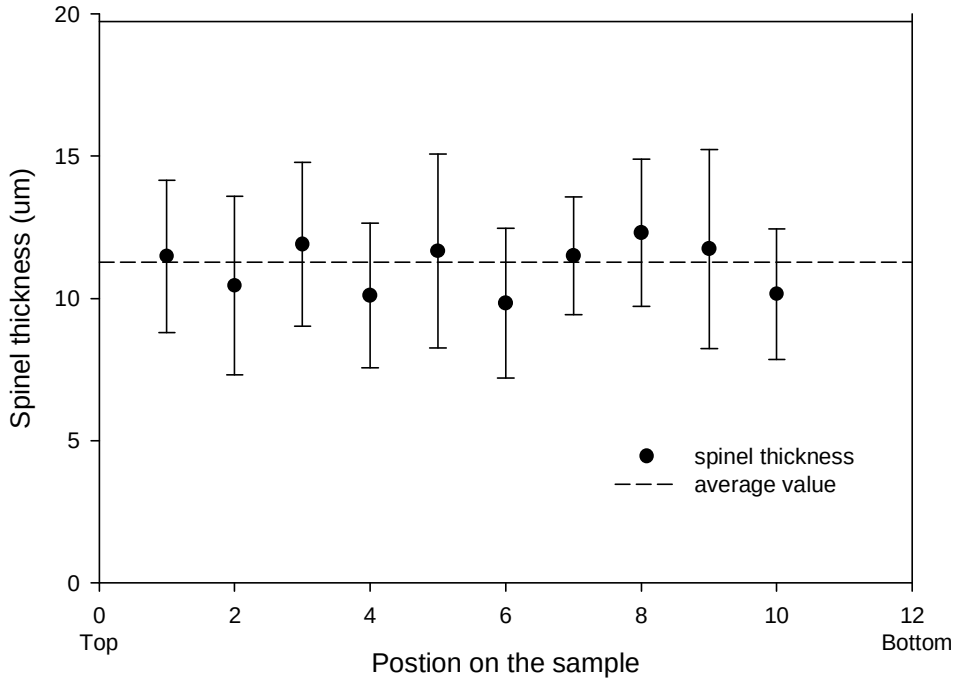

Fig. 5.24 A plot of spinel layer thickness on the $(01\bar{1}2)$ sapphire wafer reacted at 1200°C for 30 hours as a function of position

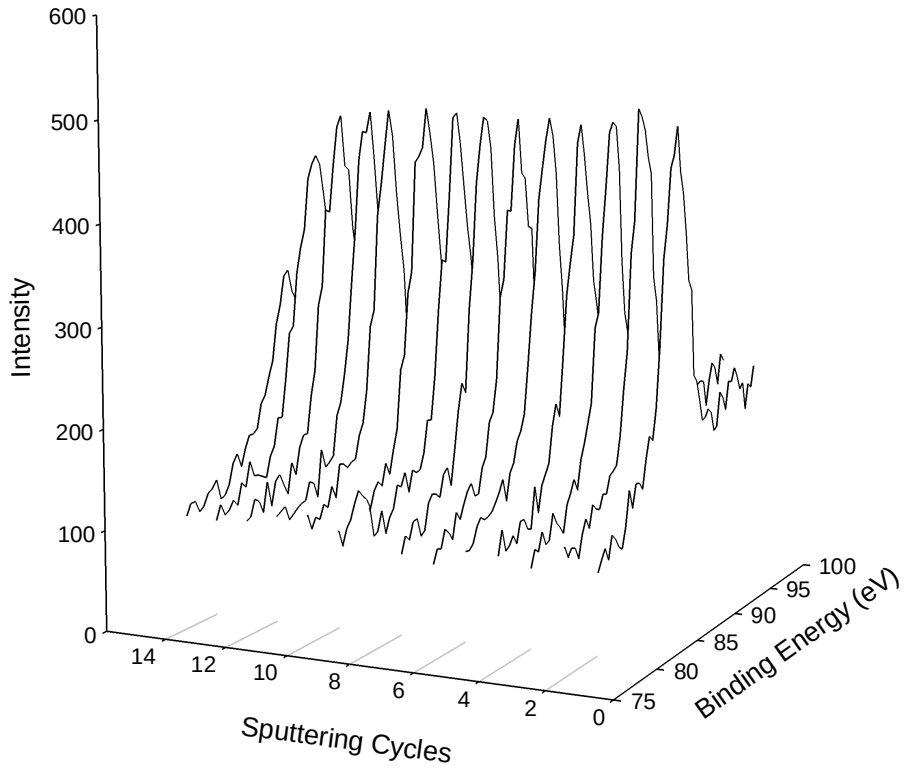

Fig. 5.25 The intensity of Mg in the $MgAl_2O_4$ layer as a function of sputtering cycles

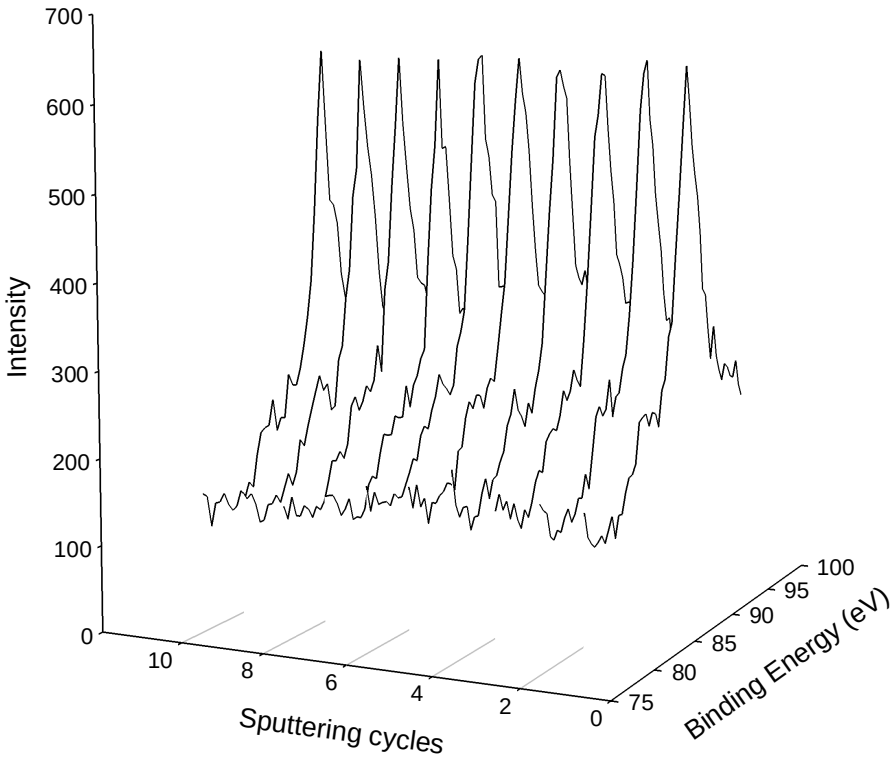

Fig. 5.26 The intensity of Mg in the Mg-Al film as a function of sputtering cycles

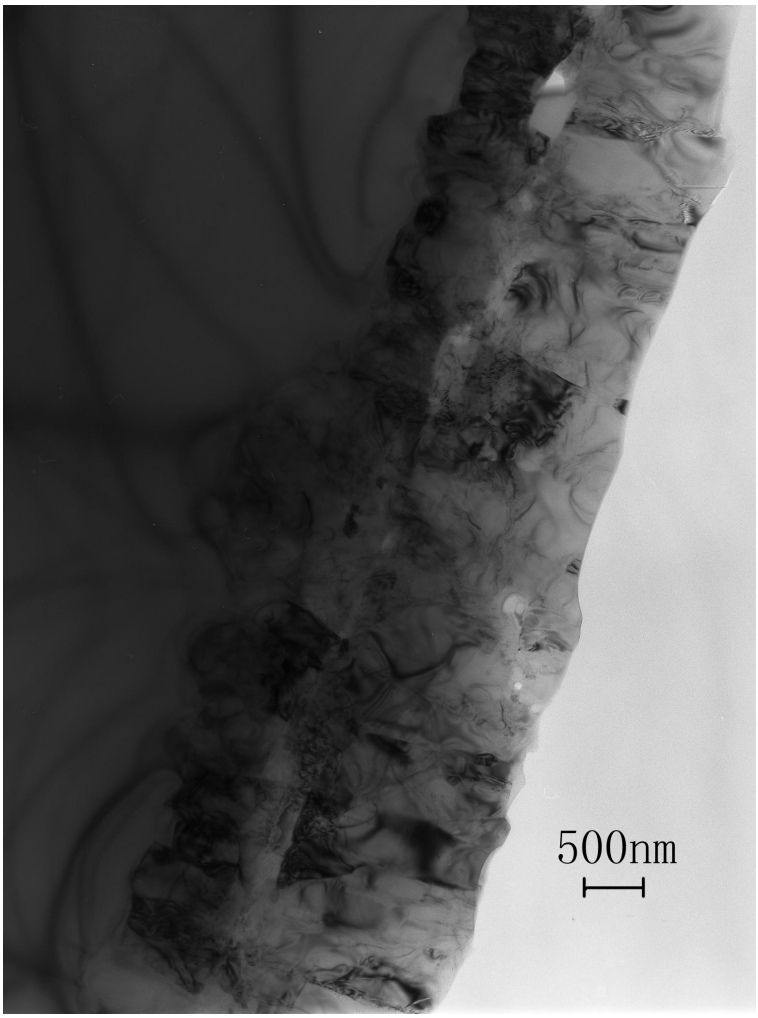

Fig. 5.27 A TEM image of the $MgAl_2O_4$ layer on the (0001) sapphire wafer reacted at 1000℃ for 7 days

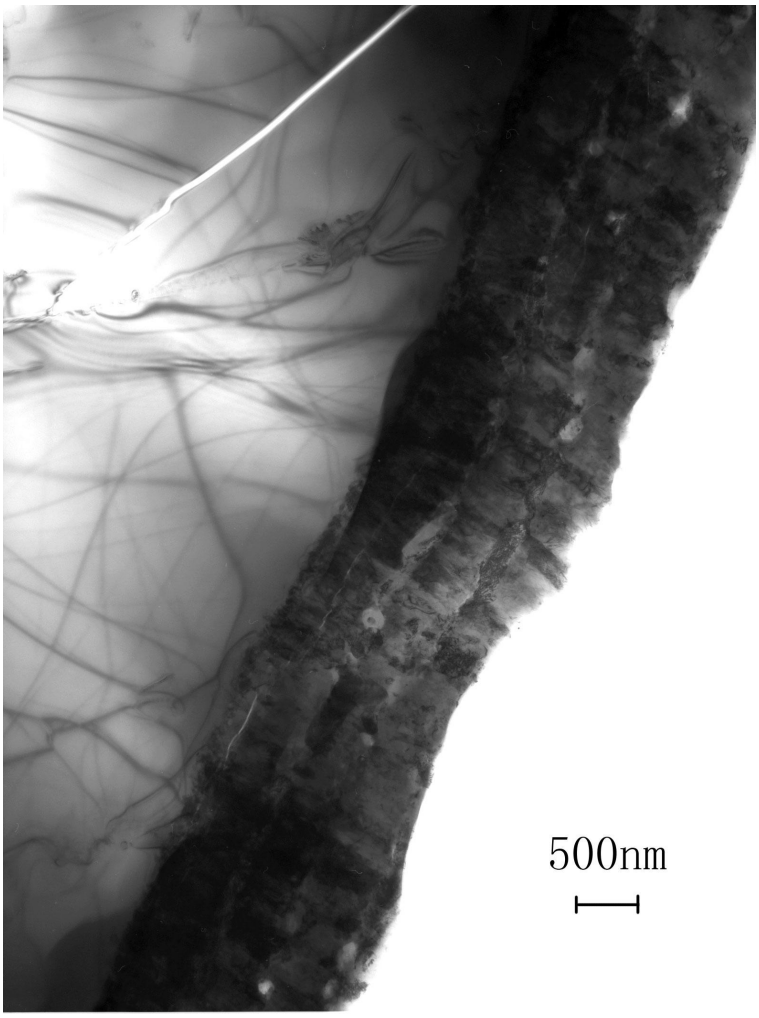

Fig. 5.28 A TEM image of the $MgAl_2O_4$ layer on the $(01\bar{1}2)$ sapphire wafer reacted at 1000°C for 7 days

5.4 Discussion

5.4.1 The Formation of a Single Product Layer

When alumina is immersed into Mg-Al melts, MgO and $MgAl_2O_4$ can be formed under appropriate conditions by the following reactions:

$$4Al_2O_3+3\{Mg\}=3MgAl_2O_4+2\{Al\} \quad (5\text{-}2)$$

$$Al_2O_3+3\{Mg\}=3MgO+2\{Al\} \quad (5\text{-}3)$$

where {} denotes species that are present in the liquid state.

The system being considered here is ternary, and the isothermal section of its phase diagram is helpful in the discussion of the chemical interaction between relevant species. For clarity, an exaggerated and schematic drawing is shown in Fig. 5.29. The point A, which corresponds to the Mg concentration of the melt in equilibrium with alumina and spinel, and the point B, which corresponds to the Mg concentration of the melt in equilibrium with magnesia and spinel, can be readily calculated with the thermodynamic data presented in Chapter II. We can classify Mg-Al alloys into three types according to their reactivity with Al_2O_3:

- Type I ($x_B<x_{Mg}<1$)

These kind of alloys are expected to form two layers (MgO and $MgAl_2O_4$) when they are in contact with alumina.

- Type II ($x_A<x_{Mg}<x_B$)

These kind of alloys are expected to form only one layer ($MgAl_2O_4$) when they are in contact with alumina.

- Type III ($0<x_{Mg}<x_A$)

These kind of alloys are expected not to react with alumina to form a new solid oxide.

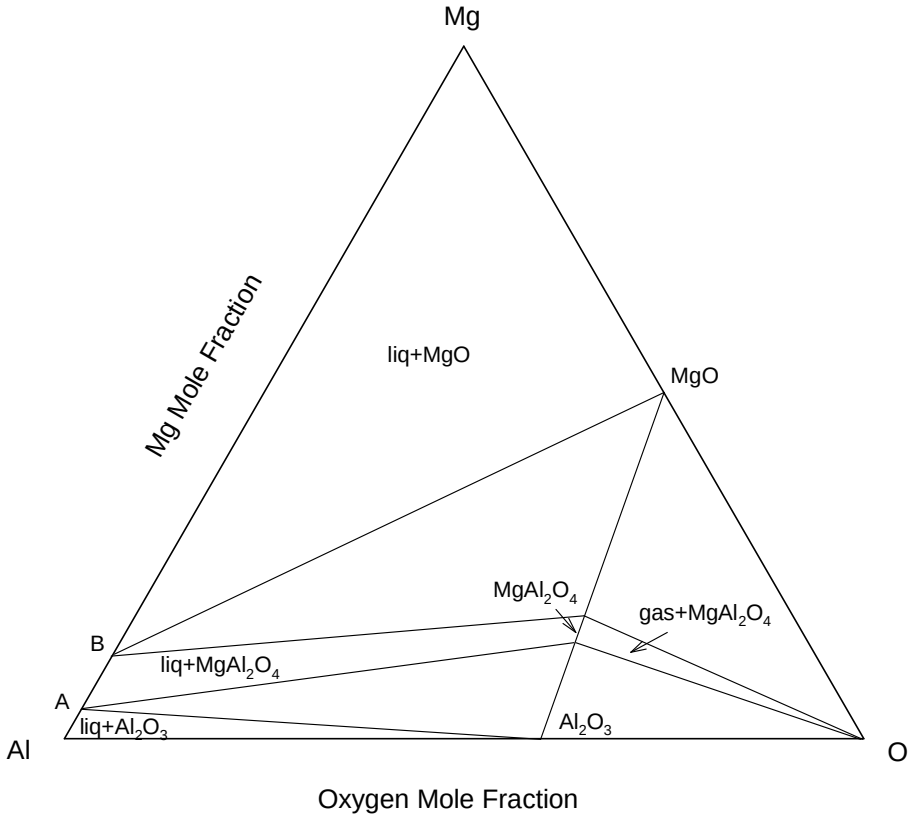

Fig. 5.29 A schematic drawing of the isothermal section of Mg-Al-O ternary phase diagram

The aim of this project was to determine the kinetic behavior for the spinel formation during incongruent reduction of sapphire in Mg-Al melts. As can be expected from thermodynamic considerations, a single phase oxide product ($MgAl_2O_4$) can be obtained if the oxygen-controlled alloys prepared at 900°C, 1000°C and 1100°C are subjected to chemical reaction with Al_2O_3 at 1000°C, 1100°C, and 1200°C, respectively.

To illustrate this idea more clearly, the position of Mg concentration in the oxygen-controlled alloy prepared at 1000°C is marked as a black point in the isothermal section of the Mg-Al-O ternary phase diagram at 1000°C in Fig. 30(a). This concentration position in the 1100°C isothermal section of the ternary system is located in the type II alloy composition range, as shown in Fig. 30(b).

However, the above discussion is based on thermodynamic calculations. There is not any restriction imposed on the formation of metastable phase MgO. Of course, the metastable phases would disappear eventually, but their temporary presence would affect the kinetic behavior. Fortunately, the consumption rate of MgO by Mg-Al melts to form $MgAl_2O_4$ is several orders of magnitude larger than the rate of $MgAl_2O_4$ growth [109]. Therefore, even if there is temporary presence of MgO in the nucleation stage, it will be accompanied with the rapid consumption to form $MgAl_2O_4$. That is to say, the conclusion that $MgAl_2O_4$ is the only reaction product under current experimental conditions is backed by both thermodynamic and kinetic factors. This kind of experimental design is also supported by the available literature information [108]. For example, V. Gabis et al. [106] observed the formation of $MgAl_2O_4$ only when Al_2O_3 was in contact with 0.3% Mg-Al alloy at 800°C and 1000°C, but no reaction product was detected when $MgAl_2O_4$ was placed in contact with the same kind of alloy at the same temperatures. D. Weirauch

[109] found that a 6 at% Mg-Al alloy could react with sapphire to form $MgAl_2O_4$ only at 800°C, and that a 3 at% Mg-Al alloy could react with MgO to form $MgAl_2O_4$ at 800°C.

As expected, only spinel was detected from XRD results shown in Fig. 5.5-5.6, which indicates that well-controlled experimental conditions were achieved for the investigation of the kinetics of spinel formation.

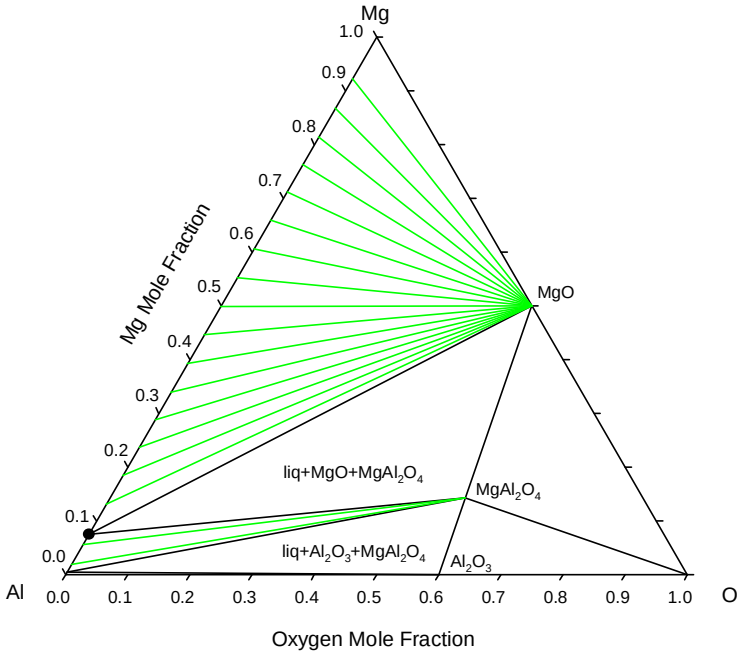

(a) The Mg composition in the oxygen-controlled alloys at 1000°C

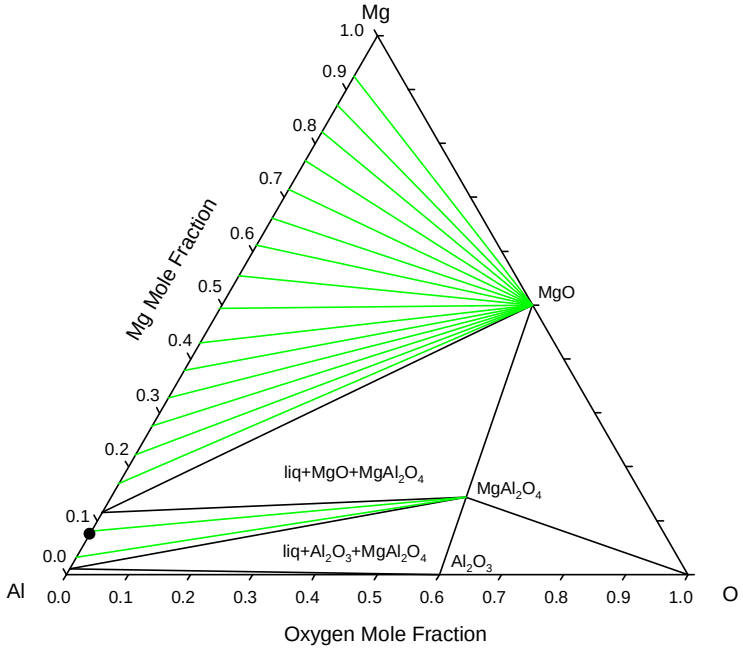

(b) The Mg composition of oxygen-controlled alloys at 1100°C

Fig. 5.30 The experimental design for forming only one oxide compound layer

5.4.2 Proposed Spinel Formation Mechanism

The mechanism of spinel formation by the solid-solid reaction between Al_2O_3 and MgO has been extensively studied as a model system for evaluation of heterogeneous solid-state reactions [68,110]. The results reveal that spinel formation occurs at the MgO-$MgAl_2O_4$ and the Al_2O_3-$MgAl_2O_4$ interfaces by the counter diffusion of Mg^{2+} and Al^{3+} through the rigid oxygen lattice of spinel. In order to meet the requirement of local electroeutrality, the cation fluxes are coupled such that for every mole of spinel forming at the MgO-$MgAl_2O_4$ interface, three moles of spinel have to form at the Al_2O_3-$MgAl_2O_4$ interface. The spinel formation reaction at the Al_2O_3-$MgAl_2O_4$ interface can be written as:

$$4Al_2O_3 + 3Mg^{2+} = 3MgAl_2O_4 + 2Al^{3+} \quad (5\text{-}4)$$

and the spinel formation occurring at the $MgAl_2O_4$-MgO interface can be expressed as:

$$2Al^{3+} + 4MgO = 3Mg^{2+} + MgAl_2O_4 \quad (5\text{-}5)$$

The combination of Equation (5-4) and (5-5) gives the following overall reaction:

$$4Al_2O_3 + 4MgO = 4MgAl_2O_4 \quad (5\text{-}6)$$

The formation of spinel by the solid-liquid reaction between Al_2O_3 and Mg-Al melts shares the same counter diffusion mechanism for cation diffusion in spinel, but involves the metal oxidation and cation reduction processes at the spinel-melt interface [106]. As soon as a continuous layer of the new spinel phase is formed, the direct contact between the molten alloy and alumina is lost and the growth of the spinel layer can only proceed by means of diffusion through the spinel phase, which may become one of the rate-limiting steps.

The oxidation and reduction processes occurring at the spinel-melt interface are based on the following reactions:

$$\{Mg\} - 2e = Mg^{2+} \tag{5-7}$$

$$Al^{3+} + 3e = \{Al\} \tag{5-8}$$

where {} denotes species present in the liquid state. The spinel formation process at the $Al_2O_3/MgAl_2O_4$ interface can also be written by Equation (5-4). Combining Equation (5-4), (5-7) and (5-8) results in the overall reaction:

$$4Al_2O_3 + 3\{Mg\} = 3MgAl_2O_4 + 2\{Al\} \tag{5-9}$$

Unless the melt is saturated with spinel, a dissolution process appearing at the $MgAl_2O_4$-melt interface is always coupled with the spinel formation process, whose reaction can be illustrated as:

$$MgAl_2O_4 = \{Mg\} + 2\{Al\} + 4\{O\} \tag{5-10}$$

A comparison of the two mechanisms for spinel formation is schematically illustrated in Fig. 5.31.

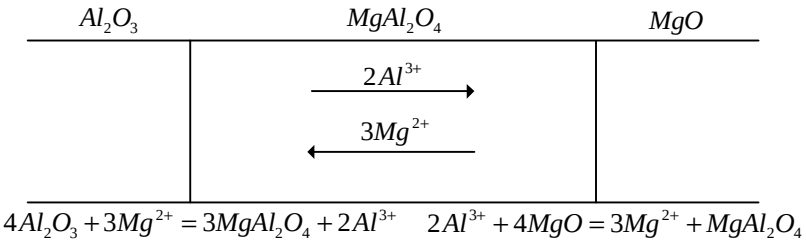

(*a*)

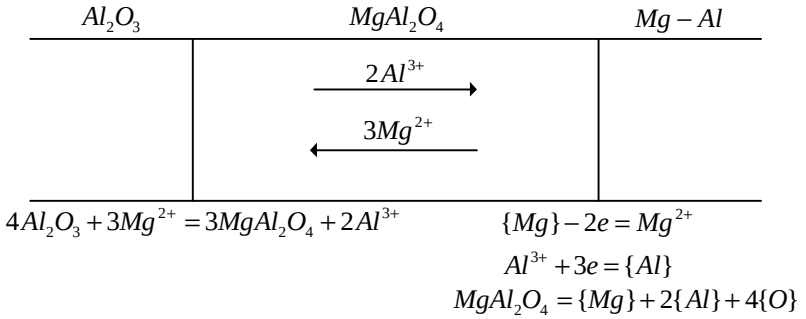

(*b*)

Fig. 5.31 Schematic diagram representing the spinel formation mechanism for: a) solid-solid reaction between Al_2O_3 and MgO, b) solid-liquid reaction between Al_2O_3 and Mg-Al melts

5.4.3 Dissolution of $MgAl_2O_4$ into Mg-Al Melts

As mentioned above, $MgAl_2O_4$ can dissociate into Mg, Al and O, which can then diffuse away from the $MgAl_2O_4$-melt interface into the melt, according to the following reaction:

$$MgAl_2O_4 = \{Mg\} + 2\{Al\} + 4\{O\} \quad (5\text{-}10)$$

Because of the high reactivity of Mg and Al with O, and therefore the low oxygen solubility in the melt, the dissolution of $MgAl_2O_4$ into Mg-Al melts can not proceed as freely as it does in oxide melts. In this section, some theoretical calculations are made to estimate the extent to which thermodynamics can allow $MgAl_2O_4$ to dissolve in the Mg-Al melt at different temperatures.

The calculations are based on the thermodynamic parameters presented in chapter II. Because MgO/$MgAl_2O_4$ crucibles were used for the incongruent reduction experiments, and a continuous $MgAl_2O_4$ layer was formed on sapphire, the maximum solubility of oxygen in the melt at the incongruent reduction temperatures was again determined by the three-phase equilibrium between MgO, $MgAl_2O_4$ and Mg-Al melts. To make this point clear, a schematic drawing of the dissolution process is illustrated in Fig. 5.32. It should be noted that the super-saturated oxygen in the Mg-Al melt caused by the dissolution process would result in the simultaneous formation of MgO or $MgAl_2O_4$ particles in the melt, whose surface would increase the total system energy. Consequently, super-saturated oxygen caused by dissolution is not likely, and thermodynamic constraints should be applied to the $MgAl_2O_4$ dissolution.

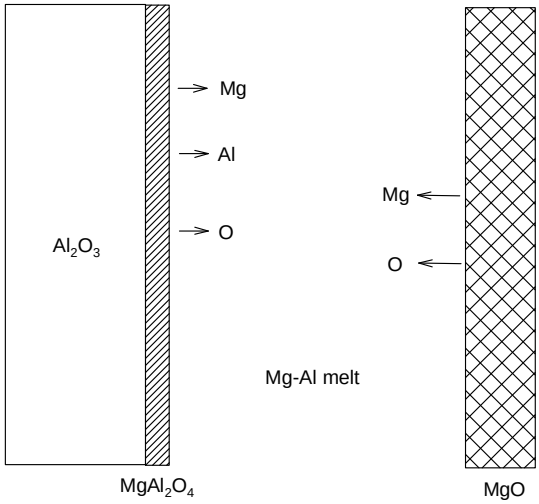

Fig. 5.32 A schematic drawing to illustrate the maximum oxygen solubility determined by the MgO-$MgAl_2O_4$-melt equilibrium

To a first-order approximation, the total amount of $MgAl_2O_4$ dissolved into the Mg-Al melt can be directly determined from the amount of oxygen change in the Mg-Al melt:

$$n_{MgAl_2O_4} = n_{total} \cdot \frac{[x_O - x_O^*]}{4} \tag{5-11}$$

where $n_{MgAl_2O_4}$ is the molar amount of dissolved $MgAl_2O_4$, n_{total} is the molar amount of oxygen-controlled Mg-Al alloy used for each run, x_O is the oxygen mole fraction in the Mg-Al melt which is equilibrated with MgO and $MgAl_2O_4$ at the incongruent reaction temperature, and x_O^* is the oxygen mole fraction in the oxygen-controlled alloy.

Sapphire wafers used for incongruent reduction are about 10 mm long, 5 mm wide, and 0.5 mm thick with two sides polished, and two wafers were tested in one MgO crucible. With this information, $n_{MgAl_2O_4}$ can now be converted into $MgAl_2O_4$ layer thickness by:

$$h = \frac{n_{MgAl_2O_4} \cdot W_{MgAl_2O_4}}{4 \cdot \rho_{MgAl_2O_4} \cdot l \cdot w} \tag{5-12}$$

where $W_{MgAl_2O_4}$ is the molecular weight of $MgAl_2O_4$, which is taken as 142.27 g/mol, $\rho_{MgAl_2O_4}$ is the $MgAl_2O_4$ density, which is taken as 3.55 g/cm^3, l and w are the length and width of the sapphire wafer, respectively.

With x_O and x_O^* obtained from thermodynamic calculations, the values of h at 1000°C, 1100°C, and 1200°C can be obtained from Equation (5-11) and Equation (5-12), and the results are listed in Table 5.8. The thickness change of $MgAl_2O_4$ layer caused by dissolution at different temperatures is smaller than the resolution of the micrometer (1 micron) used for this study, and its magnitude is within the experimental error, as clearly

seen in the spinel layer thickness plots in Fig. 5.11-5.13 from SEM results. Consequently, the dissolution effect is too small to be considered in the current experiments.

For comparison, the maximum solubility of oxygen in the melt determined by the three-phase equilibrium between MgO, Al_2O_3 and melts at the incongruent reduction temperatures were also calculated. The calculated results as well as the oxygen concentration in the oxygen-controlled alloys were used to estimate the thickness change of sapphire wafers caused by dissolution. Equations used were exactly the same as Equation (5-11) and (5-12) except that the factor 4 in Equation (5-11) was replaced by 3 and the molecular weight and the density of $MgAl_2O_4$ were replace by those of Al_2O_3. It was found that the h values were 0.466 microns, 0.850 microns and 1.141 microns for 1000°C, 1100°C, and 1200°C, respectively.

In fact, the above calculation overestimates the dissolution of $MgAl_2O_4$. In the presence of MgO in the crucible, the increase of oxygen in the melt caused by $MgAl_2O_4$ dissolution is much smaller than the values presented in Table 5.8. This conclusion will be confirmed by the following theoretical calculations.

Table 5.8 The calculated parameters for the dissolution of $MgAl_2O_4$ into Mg-Al melts

Temperature	n_{total}	x_O	x_O^*	h
°C	mole			micron
1000	0.8	5.53e-6	2.46e-6	0.123
1100	0.8	1.15e-5	5.53e-6	0.239
1200	0.8	2.05e-5	1.15e-5	0.361

5.4.4 Natural Convection Simulation

In the quasi-binary system of Al_2O_3-MgO at a given arbitrary temperature and arbitrary pressure, the number of degrees of freedom is zero at a two-phase equilibrium. Therefore, the compositions of the phases at the interface between Al_2O_3 and $MgAl_2O_4$ are given by the tie-line of the two phase equilibrium. Because of the local equilibrium assumption on the moving interface, the compositions at the Al_2O_3-$MgAl_2O_4$ interface can be directly obtained from the Al_2O_3-MgO binary phase diagram. However, since the Mg-Al melt and $MgAl_2O_4$ are ternary solutions when equilibrated with each other at a given temperature and pressure, the boundary between Mg-Al melt and $MgAl_2O_4$ is not invariant, which is a consequence of the Gibbs phase rule. Therefore, there remains one more degree of freedom and the operating tie-line is determined by the condition in which the mass balance of every diffusing element gives the same interface velocity [111]. That is to say, the tie-line selection is totally determined by the kinetic process which can not be determined from thermodynamic information alone.

Theoretically, the Mg concentration at the $MgAl_2O_4$-melt interface can be obtained by one of the following methods:

- Determine the lattice parameters of $MgAl_2O_4$ so that the composition can be obtained from the relationship between lattice parameter and composition.
- Determine the surface composition of $MgAl_2O_4$ directly by XPS.

In practice, the first method does not work. According to the work of Yet-Ming Chiang [112], the lattice parameters of Mg-rich $MgAl_2O_4$ were found to be essentially independent of composition. That is to say, the density of $MgAl_2O_4$ remained constant when more Mg cations entered the spinel crystal structure. Efforts have been made to

conduct the second method. $MgAl_2O_4$ and MgO wafers with (111) and (100) orientations were purchased and employed as standards, and then analyzed by ICP and XPS. Due to the high precision requirement in this work, the ICP and XPS results were far from satisfactory. Consequently, the second method was also abandon.

Due to the lack of an accurate method for the determination of Mg concentrations at the $MgAl_2O_4$-melt interface at different temperatures, and also due to the importance of the Mg concentration values for calculations, there is a considerable need to predict these values from the kinetic properties of the whole system. In this study, a numerical simulation was performed to simulate metallic fluids flowing past a vertical sapphire wafer which was undergoing incongruent reduction.

The following assumptions were made:

- The spinel formation reaction takes place only at the Al_2O_3-$MgAl_2O_4$ interface, and the products of chemical reaction and dissolution are emitted into the melt from the $MgAl_2O_4$-melt interface. Because the fluid adjacent to the vertical surface receives Al and becomes denser, the concentration buoyancy always acts in the vertically downward direction.
- The fluid is Newtonian, and the viscosity is assumed to be independent of composition.
- The density of the Mg-Al melt is a function of temperature and composition, and the experimental data from the literature can be fitted to a regular-solution type equation.

For the model which is simplified so that all the assumptions mentioned above are satisfied, the governing PDEs for natural convection driven by the concentration gradient

near a vertical flat plate can be obtained from the principles of mass conservation and momentum conservation, which are written below [92]:

$$\nabla \cdot \vec{u} = 0 \tag{5-13}$$

$$\frac{\partial \vec{u}}{\partial t} + (\vec{u} \cdot \nabla)\vec{u} = -\frac{1}{\rho_0}\nabla p + \nu \nabla^2 \vec{u} + \frac{\rho - \rho_0}{\rho_0} g \tag{5-14}$$

$$\frac{\partial x_{Mg}}{\partial t} + (\vec{u} \cdot \nabla) x_{Mg} = D \nabla^2 x_{Mg} \tag{5-15}$$

where $\vec{u}$ is the velocity vector whose components are u and v, x_{Mg} is the Mg molar fraction of the melt, t is time, g is the gravitation acceleration vector, ν is the kinematic viscosity, ρ is the fluid density, ρ_0 is the initial fluid density, and D is the chemical diffusivity of Mg in Mg-Al melt.

The physical model under consideration is illustrated in Fig. 5.33, which represents a vertical sapphire wafer of 10 mm length and 0.5 mm thickness in the Mg-Al melt. For simplicity, only half of the geometry was modeled due to symmetry. The schematic drawing of the model domain with each boundary assigned by an identification number is shown in Fig. 5.34, where boundary 5 is the place where the sapphire wafer is located, boundaries 2 and 3 are the crucible walls, and boundary 1 is the free surface of the Mg-Al melt.

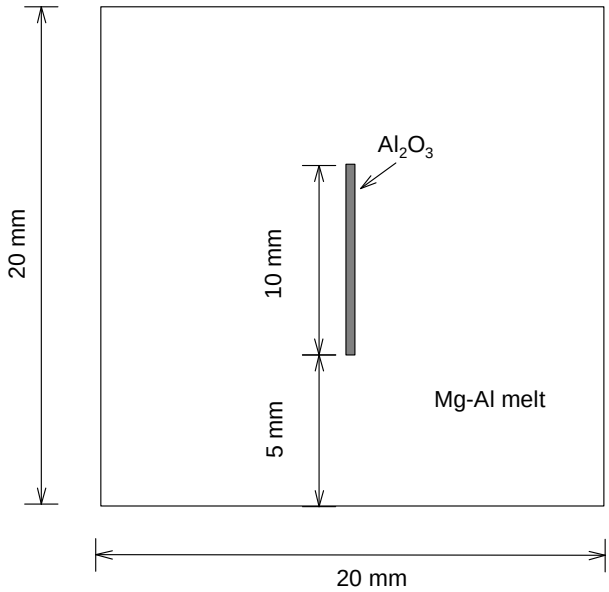

Fig. 5.33 The schematic drawing for model setup

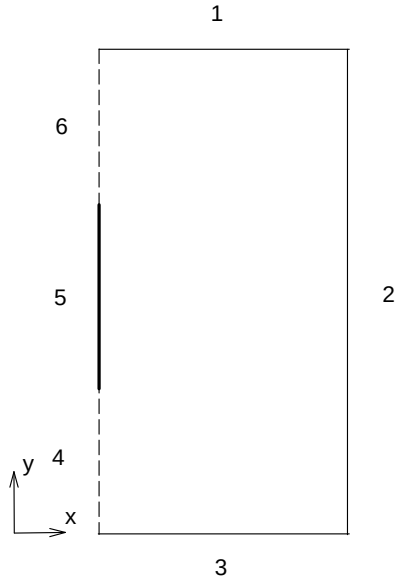

Fig. 5.34 The half geometry used for simulation

To solve the governing PDEs, the following initial conditions and boundary conditions are used:

1) Initial Conditions:

For the Naiver-Stokes equation, the fluid is at rest so that the velocity is zero within the whole domain.

For the diffusion equation, the concentration of the melt is at the same level everywhere, and it is determined by the composition of the oxygen-controlled alloy used for the incongruent reduction.

2) Boundary Conditions:

For the Naiver-Stokes equation, the symmetric boundary condition is chosen for boundaries 4 and 6. On boundaries 1, 2, 3 and 5, non-slip boundary conditions are applied.

For the diffusion equation, boundaries 1, 2, 3, 4 and 6 are set as insulation boundary conditions. A flux of Mg is consumed by the sapphire wafer at boundary 5. Therefore, boundary 5 is set as the Neumann boundary condition, whose flux expression can be directly obtained from experimental results in this work.

The flux expression for boundary 5 can be written as:

$$\begin{aligned} J &= -\frac{dn'_{MgAl_2O_4}}{A \cdot dt} = -\frac{\rho_{MgAl_2O_4} \cdot l \cdot w \cdot dx}{W_{MgAl_2O_4} \cdot l \cdot w \cdot dt} \\ &= -\frac{\rho_{MgAl_2O_4}}{W_{MgAl_2O_4}} \cdot \frac{dx}{dt} = -\frac{\rho_{MgAl_2O_4}}{W_{MgAl_2O_4}} \cdot \frac{1}{2} \cdot \sqrt{\frac{k}{t}} \end{aligned} \tag{5-16}$$

where l is the sapphire wafer length, w is its width, $n'_{MgAl_2O_4}$ is the molar amount of $MgAl_2O_4$ on the sapphire wafer, t is time, $\rho_{MgAl_2O_4}$ is the spinel density, $W_{MgAl_2O_4}$ is the

molecular weight of spinel, and k is the parabolic constant of spinel growth at a certain temperature which can be taken from current experimental results.

It should be noted that the unknown for the diffusion Equation (5-15) is the mole fraction of Mg, not the molar concentration or molar density of Mg. In order to utilize the flux equation derived above, a term V_m must be multiplied, which leads to:

$$J = -\frac{V_m \cdot \rho_{MgAl_2O_4}}{M_{MgAl_2O_4}} \cdot \frac{1}{2} \cdot \sqrt{\frac{k}{t}} \tag{5-17}$$

where V_m is the molar volume of Mg-Al melts, which can be expressed as a function of melt density ρ and Mg molar fraction x_{Mg} as below: (the density unit is g/cm^3)

$$V_m = \frac{x_{Mg} \cdot 24.305 + (1 - x_{Mg}) \cdot 26.981}{\rho} \cdot 10^{-6} \quad \text{m}^3/\text{mol} \tag{5-18}$$

In this simulation, the parabolic constants of spinel growth on (0001) sapphire wafers at different temperatures were adopted. The calculated flux expressions for boundary 5 are listed in Table 5.9, where the negative sign of each flux indicates the flux of Mg was going out of the simulation domain across boundary 5.

In summary, all the boundary conditions used for the Naiver-Stokes equation and diffusion equation are presented in Fig. 5.35 and 5.36 for clarity.

Table 5.9 The Mg flux equation used on boundary 5 for the diffusion equation at different temperatures

Temperature	J (mol/m^2·s)
1000°C	$-1.23\cdot10^{-4}\cdot V_m\cdot t^{-1}$
1100°C	$-2.71\cdot10^{-4}\cdot V_m\cdot t^{-1}$
1200°C	$-3.44\cdot10^{-4}\cdot V_m\cdot t^{-1}$

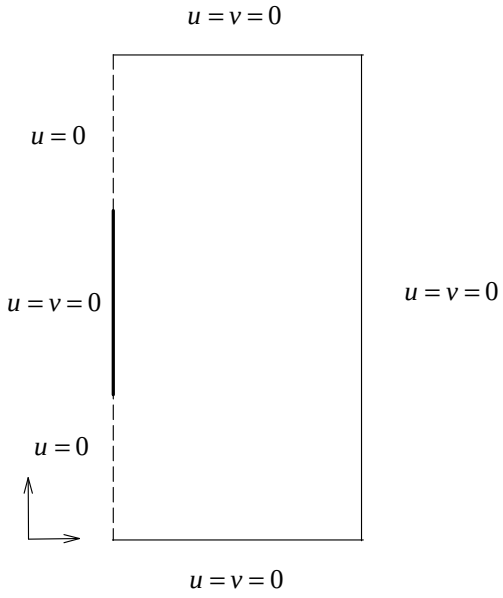

Fig. 5.35 The boundary conditions for the Navier-Stokes equation

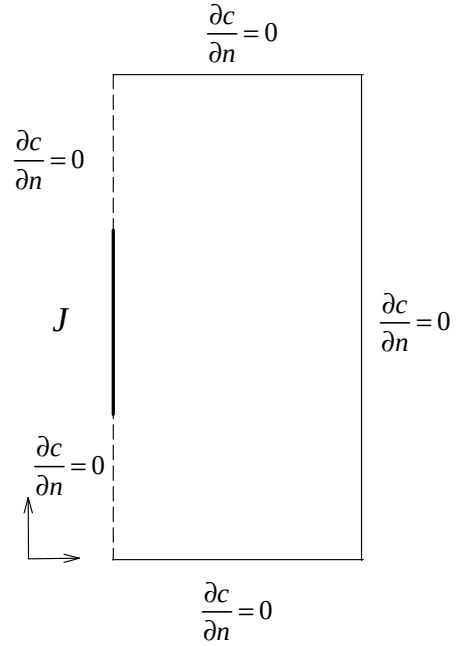

Fig. 5.36 The boundary conditions for the diffusion equation

The density of Mg-Al melt as a function of temperature and composition is still rare in the literature. P. Erich [113] measured the density of Mg-Al melt as a function of concentration at 500°C, 600°C, 700°C and 800°C. If the density of pure liquid Al and Mg can be described as a linear function of temperature T, and the density of Mg-Al melt can be expressed by a regular-solution-type equation to express the contribution of the interaction between Mg and Al, then the density of Mg-Al melts as a function of temperature and Mg concentration can be written as:

$$\begin{aligned}\rho &= x_{Mg}\cdot\rho_{Mg}^{0} + x_{Al}\cdot\rho_{Al}^{0} + \rho^{ex} \\ &= x_{Mg}\cdot(a - b\cdot T) + x_{Al}\cdot(c - d\cdot T) + x_{Mg}\cdot x_{Al}\cdot(e + f\cdot T)\end{aligned} \tag{5-19}$$

where ρ_{Mg}^{0} and ρ_{Al}^{0} are the density of pure Mg and Al, respectively. a, b, c, d, e and f are constants obtained by applying least square regression to P. Erich's experimental results. The values for those parameters are listed in Table 5.10, where a, c and e have the density unit, while b, d and f have the same unit as the derivative of density with respect to temperature. The calculated densities with those parameters as well as the original data of P. Erich are plotted in Fig. 5.37 for comparison.

For simplicity, the viscosity of the Mg-Al melt is chosen as the value of pure Al melt, which can be expressed as [114]:

$$\mu_{Al} = 2.45\cdot10^{-5}\cdot\exp(\frac{30500}{R\cdot T}) \quad \text{Pa}\cdot\text{s} \tag{5-20}$$

The diffusion coefficient of Mg in molten Mg-Al has been critically reviewed by Y. Du [115], and the proposed diffusion coefficient as a function of temperature can be written as:

$$D = 9.9\cdot10^{-5}\exp(-\frac{71600}{R\cdot T}) \quad \text{m}^2/\text{s} \tag{5-21}$$

where R is the gas constant, and T is the absolute temperature.

Table 5.10 The parameters for Mg-Al melt density

Parameter	Value	Units
a	1.71809324	g/cm^3
b	0.000202847192	$g/cm^3 \cdot K$
c	2.59409471	g/cm^3
b	0.000305520349	$g/cm^3 \cdot K$
e	-0.254315925	g/cm^3
f	0.000324294118	$g/cm^3 \cdot K$

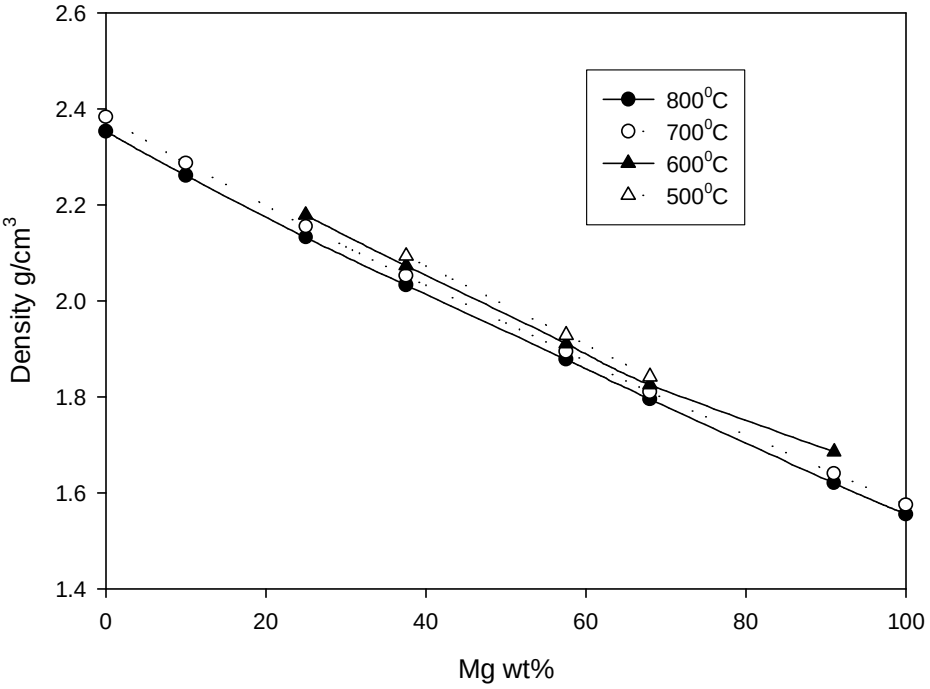

Fig. 5.37 A plot of the regressed and experimental Mg-Al melt density at different temperatures [113]

The simulation was performed with Femlab, which is a commercial finite-element-method package. The size of the mesh was gradually adjusted so that any further increase in the mesh density would not change the solution. The velocity field and concentration field simulated at 1200°C for 30 hours are plotted in Fig. 5.38, with the arrow indicating the velocity direction and concentration gradient, respectively.

As can be seen from the velocity plot, the fluid reacted with the sapphire wafer on boundary 5 and moved downward due to buoyancy changes. That is to say, the Mg-rich fluid was brought into contact with the sapphire wafer with a subsequent downward movement of Mg-rich fluid above the sapphire wafer surface to replace the Al-rich fluid. In addition to this downward movement near the sapphire wafer surface, fluid near the crucible wall continuously moved upward to supply Mg-rich melts for the incongruent reduction at boundary 5.

The velocity field was observed to have a minimum point near the middle of the domain, across which the flow changed direction. As can be seen from the color bar, the maximum velocity in the domain used for simulation was around 3.804e-9 m/s, indicating the flow velocity induced by the natural convection was extremely slow. The negligible flow rate could also be reflected from the concentration plot in Fig. 5.38, where the concentration field was symmetric with respect to the horizontal line of y=0.01.

To have a better understanding of the concentration and velocity evolution under the simulation conditions mentioned above, the fluid velocity profile at the line y=0.01 as a function of distance from the sapphire surface and time is presented in Fig. 5.39. Two local velocity maxima were observed whose peaks increased first and then decreased with time.

The concentration of Mg in the fluid that was adjacent to the sapphire surface is plotted in Fig. 5.40 as a function of distance from the sample top and time. As can be seen, the Mg distribution was very uniform along the sapphire wafer except for the time at 100 seconds, which was caused by the flux expression (the flux is infinite at t=0) . The Mg concentration profile in the melt at the horizontal line y=0.01 is also presented in Fig. 5.41 as a function of the distance from the sample surface, and the results clearly indicated that the concentration gradient of Mg did not develop in the melt in that the diffusion coefficient of Mg in the melt is much faster than the interdiffusion coefficient in spinel.

Similar results were obtained from the simulation at 1000°C and 1100°C. For simplicity, only the Mg concentrations of the fluids at the middle point of sapphire surface as a function of time are presented. Those values were then used to calculate the theoretical parabolic constants. Consequently, the Mg concentrations of the melt at the middle position of sapphire surface are plotted as a function of time in Fig. 5.42, 5.43 and 5.44 for the temperature of 1200°C, 1100°C, and 1000°C, respectively. As can be seen, those curves gradually decreased on a very small scale so that the Mg concentration changes at the middle position of sapphire wafer were only on the order of 1e-4, which was too small to be detectable. For comparison, the maximum velocities developed in the melt at different temperatures are presented in Fig. 5.45.

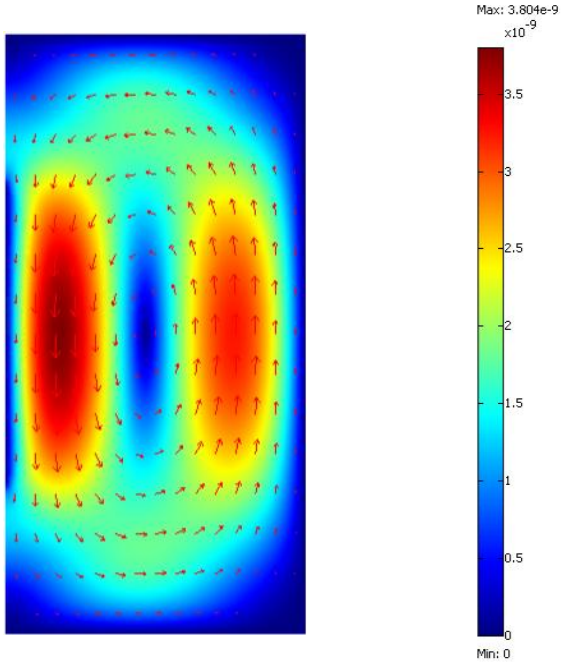

a:) The velocity profile with velocity direction superimposed

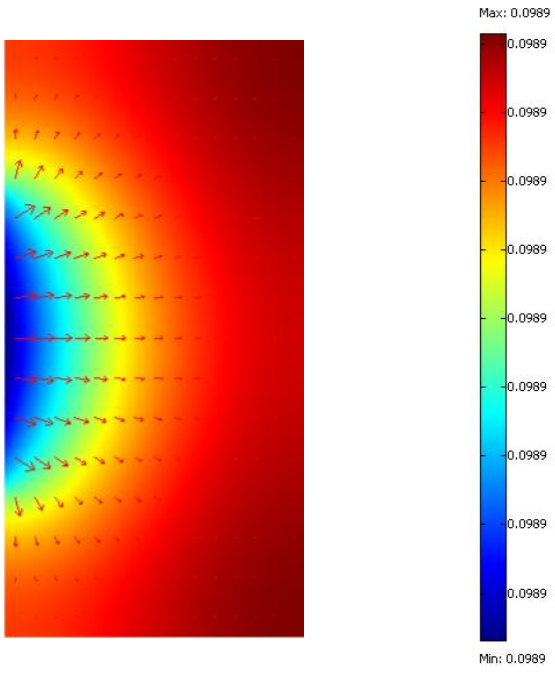

b:) The concentration profile with concentration gradient superimposed

Fig. 5.38 The simulation results at 1200°C for 30 hours

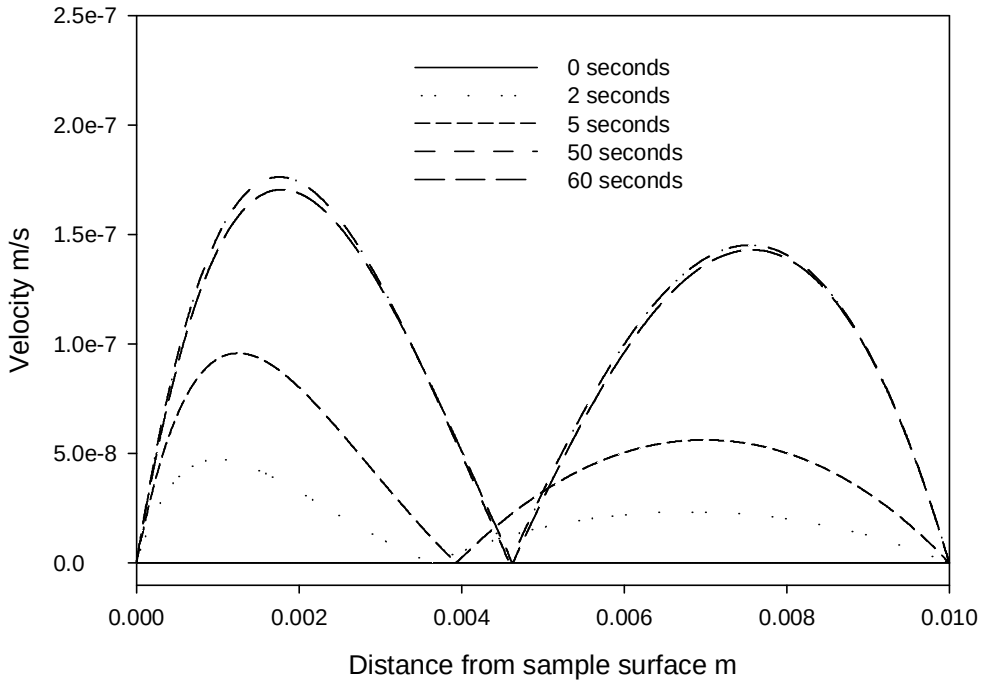

Fig 5.39 The velocity profile on the cross section as a function of time at 1200℃

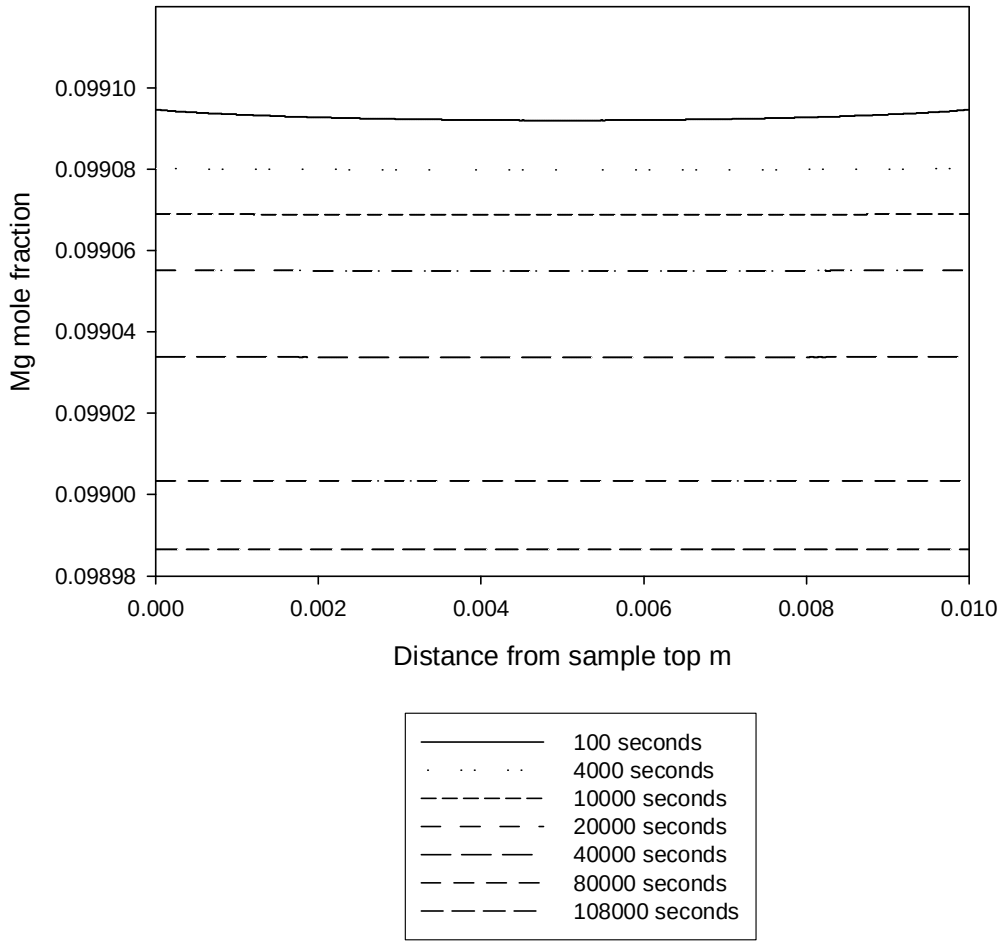

Fig 5.40 The Mg concentration of the melt on the sapphire surface as a function of distance from sample top at 1200°C

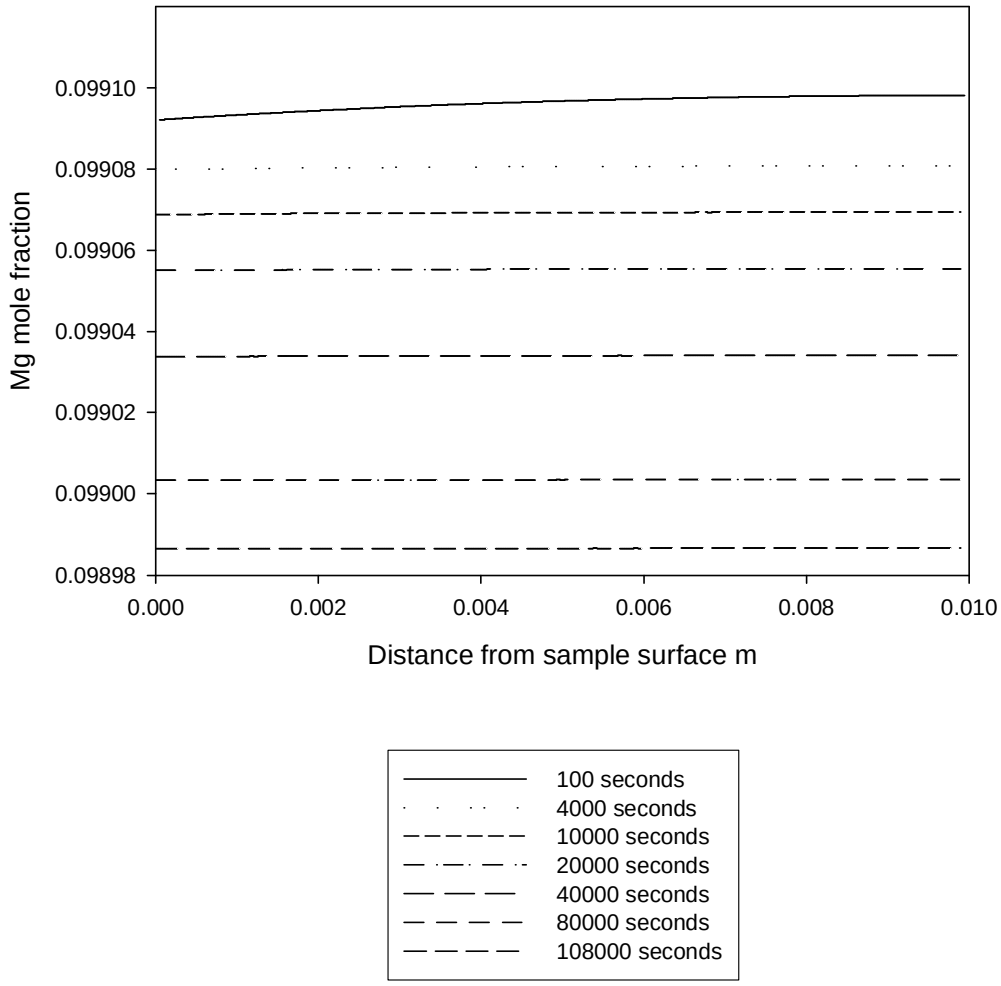

Fig 5.41 The Mg concentration on the line of y=0.01 in the Mg-Al melts as a function of time at 1200°C

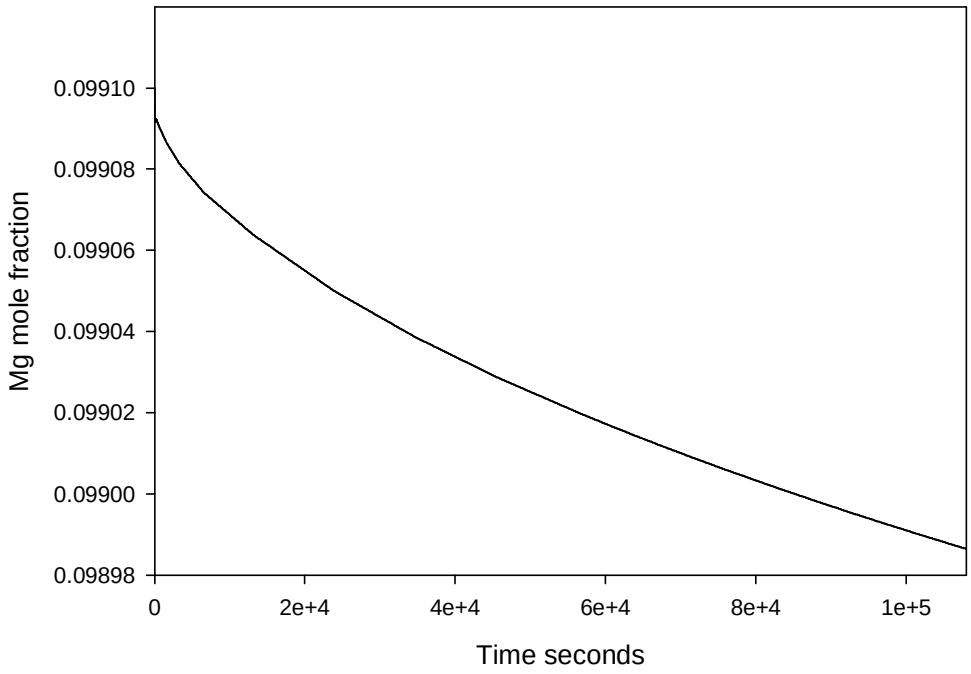

Fig 5.42 The Mg concentration of the melt at the middle position of sapphire surface as a function of time at 1200°C

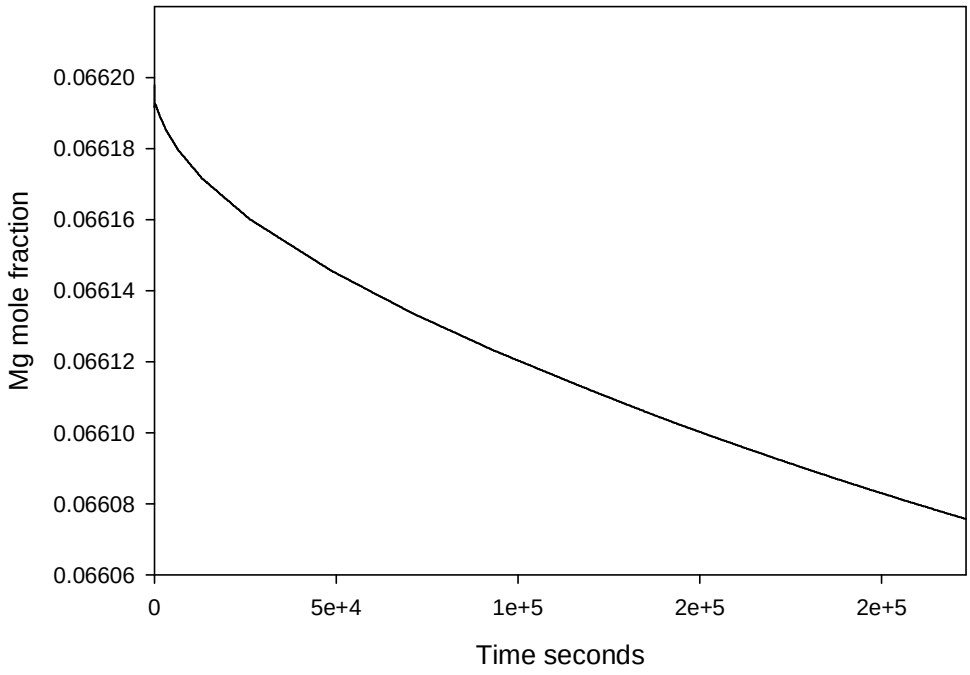

Fig 5.43 The Mg concentration at the middle position of sapphire surface as a function of time at 1100°C

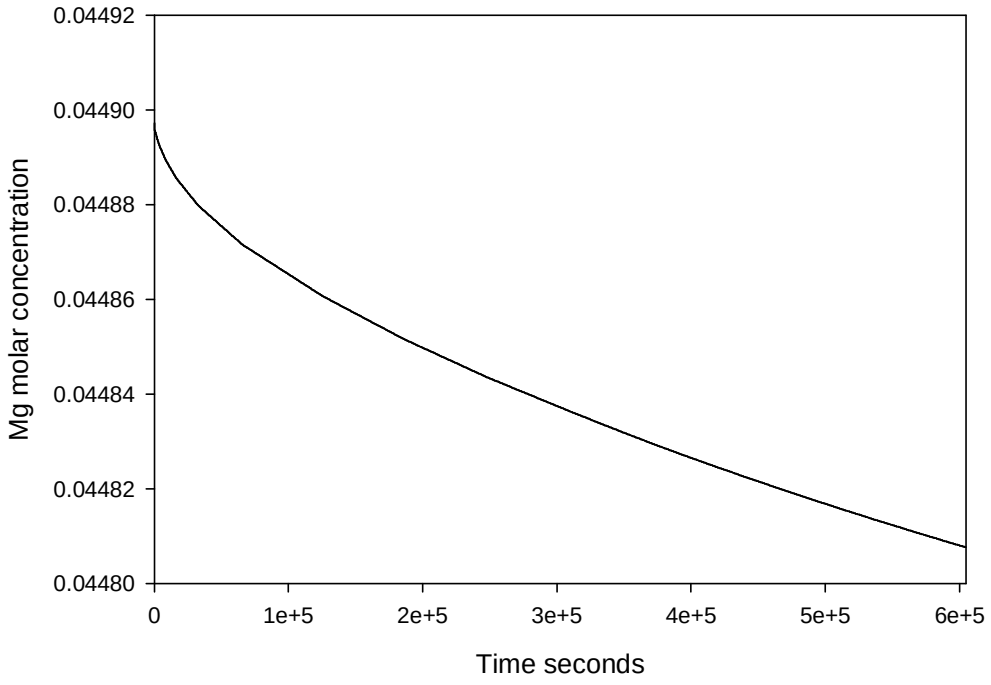

Fig 5.44 The Mg concentration at the middle position of sapphire surface as a function of time at 1000°C

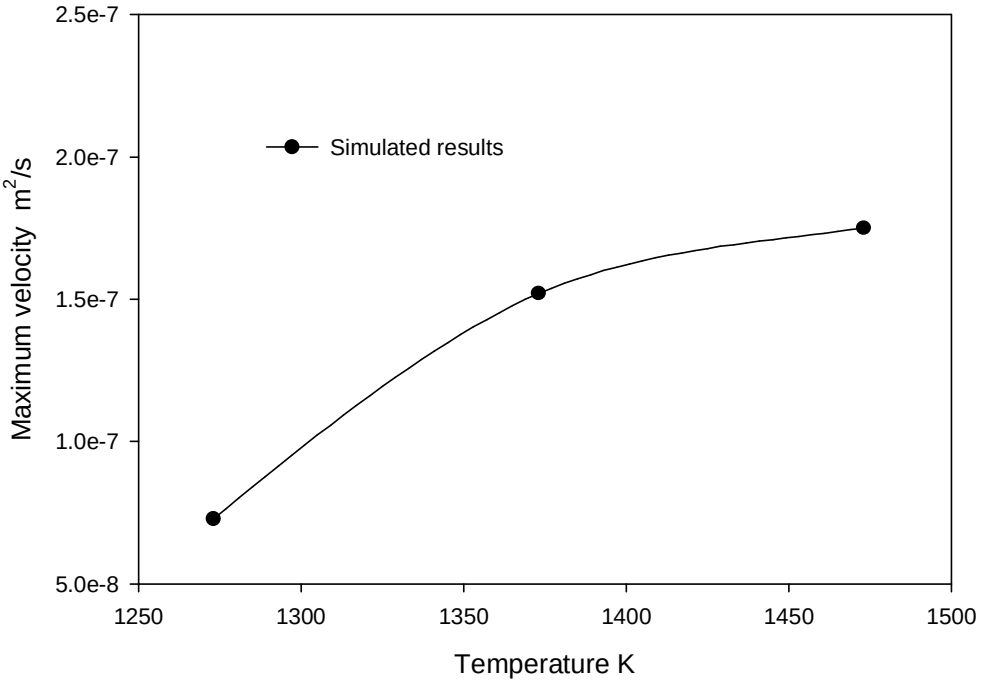

Fig 5.45 The maximum velocity developed in the Mg-Al melts at different temperatures

5.4.5 Kinetic Calculations

The parabolic relationship between the spinel layer thickness and time was seen over the whole reaction period at different temperatures. The parabolic rate constants evaluated by a least-square regression for (0001) and $(01\bar{1}2)$ sapphire wafers have already been presented in Table 5.7. The kinetics for the two sapphire orientations showed almost the same reaction rate, indicating no effect of sapphire orientations on the kinetics under current experimental conditions. Although similar results were obtained by R. C. Rossi [116] for the spinel formation between MgO and Al_2O_3, no explanation has ever been made since then.

It can be proved that as long as the spinel formation is rate-limited by the diffusion process in spinel, the kinetics should be independent of the sapphire orientation. This is attributed to the cubic crystal structure of spinel whose diffusivity tensor can be reduced to the diagonal form as below [117]:

$$D_{ij} = \begin{bmatrix} D_{11} & 0 & 0 \\ 0 & D_{11} & 0 \\ 0 & 0 & D_{11} \end{bmatrix}$$

where D_{11} is the diffusivity in <100> directions. It can be seen that all the diagonal elements of this diffusion tensor are identical, indicating the diffusion property in the cubic crystal is identical for isotropic materials, and therefore the diffusion coefficient and the kinetics are independent of crystal orientations.

Based on the following assumptions, a simple model is presented here to calculate the theoretical parabolic constants for spinel formation at different temperatures:

1) The O^{2-} diffusion in $MgAl_2O_4$ is very slow compared to the diffusion of Mg^{2+} and Al^{3+}. Consequently, the oxide layer can only grow into the alumina side, requiring only cation diffusion and not O^{2-} diffusion.
2) The local equilibrium is maintained at the interfaces, although the whole system is far from equilibrium.
3) The interfacial reactions are very rapid, and the diffusion through $MgAl_2O_4$ is the only rate-limiting step. This is reasonable because the diffusion coefficient in the Mg-Al melt is several orders of magnitude larger than that in solid oxides. Therefore, the Mg concentration gradient in the liquid phase is neglected. This assumption is consistent with the simulation results where the concentration gradient in the melt is too small to be detectable.

The schematic drawing of the Mg concentration profile with the diffusion in spinel being the only rate-limiting step is presented in Fig. 5.46. When the diffusion in spinel is the only rate-limiting step and the dissolution rate of spinel into the melt is too small to be important, the parabolic growth rate of spinel formation derived by E. Bruce [26] for describing the reaction between Al_2O_3 and MgO can be modified and directly applied to the reaction between Al_2O_3 and Mg-Al melts due to the same diffusion mechanism. The growth of spinel by the consumption of alumina at the spinel-alumina interface is determined by the supply rate of Mg cation via the diffusion through spinel, whose rate can be given by:

$$J_{Mg}^{spinel} - J_{Mg}^{sapphire} = \dot{x} \cdot (C_{Mg}^{2} - C_{Mg}^{3}) \tag{5-22}$$

where $\dot{x}$ is the growth rate of spinel, C_{Mg}^{2} and C_{Mg}^{3} are the Mg concentrations at the $MgAl_2O_4$-Al_2O_3 interface in spinel and in Al_2O_3, respectively. Recognizing that C_{Mg}^{3} is

very small within the temperature range of these experiments in Fig. 2.10, and $J_{Mg}^{sapphire}$ can be ignored, Equation (5-22) is simplified to:

$$J_{Mg}^{spinel} = x \cdot C_{Mg}^{2} \tag{5-23}$$

The linear concentration profile of Al and Mg in spinel was observed by E. Bruce [26] for the spinel formation between Al_2O_3 and MgO. If such a tendency can be assumed in the present work, the flux of Mg in spinel can be expressed by:

$$J_{Mg}^{spinel} = -\tilde{D}\frac{C_{Mg}^{1} - C_{Mg}^{2}}{x} \tag{5-24}$$

where $\tilde{D}$ is the interdiffusion coefficient in spinel and C_{Mg}^{1} is the Mg concentration of spinel at the spinel-melt interface . The parabolic growth equation is expressed as:

$$x^2 = k \cdot t \tag{5-25}$$

Taking the derivative of both sides with respect to time t and combining Equations (5-22), (5-23) and (5-24) lead to an expression for the theoretical parabolic constant in the absence of dissolution process:

$$k = 2\tilde{D}\frac{C_{Mg}^{1} - C_{Mg}^{2}}{C_{Mg}^{1}} \tag{5-26}$$

As discussed in the previous section, C_{Mg}^{4} can be obtained from the kinetic simulation which is presented in Fig. 5.42-5.44. The corresponding C_{Mg}^{1} which is in equilibrium with the melt having the composition of C_{Mg}^{4} can be obtained from thermodynamic calculations.

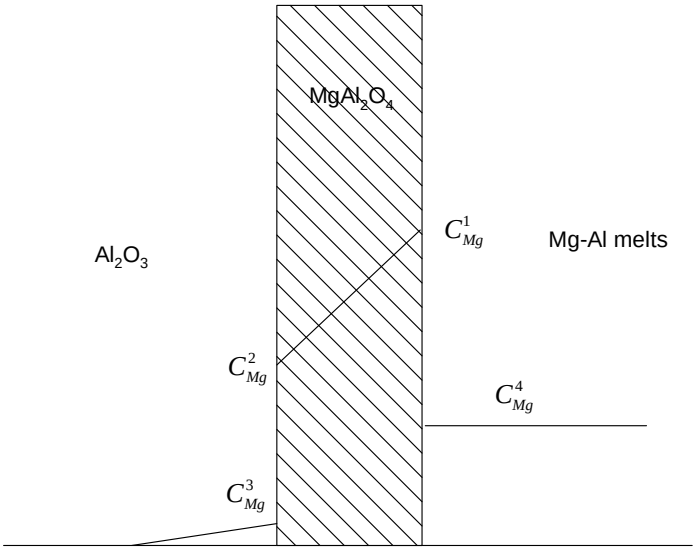

Fig. 5.46 The Mg concentration profile with the diffusion in spinel being the only rate-limiting step.

Fig. 5.47 is the amplified $MgAl_2O_4$ corner of the isothermal section of the ternary Mg-Al-O phase diagram at 1100°C. A careful investigation of this figure shows that for the equilibrated $MgAl_2O_4$-melt mixture, the Mg concentration in $MgAl_2O_4$ is not strongly sensitive to the Mg concentration in the melts.

To illustrate this tendency more clearly, plots of Mg concentrations in the Mg-Al melt against those in $MgAl_2O_4$ at different temperatures are presented in Fig. 5.48-5.50. The ranges of the horizontal coordinate are carefully chosen such that they can reflect the Mg concentrations in the Mg-Al melt during the incongruent reduction at different temperatures. That is to say, the lower limit of the horizontal axis corresponds to the compositions of the starting oxygen-controlled alloys and the upper limit denotes the compositions of the melts with the longest reaction time at a certain temperature. As can be seen from Figs. 5.48-5.50, C_{Mg}^{1} differs slightly with respect to the Mg concentration in the melt, making it reasonable to treat C_{Mg}^{1} as constants in the calculation of the parabolic constants by Equation (5-25) at a given temperature.

Inserting those data into Equation (5-25) and adopting the interdiffusion coefficient of Mg in spinel by E. Bruce [26] as below:

$$\widetilde{D} = 2.5\times10^{-6}\exp(-28200/T) \qquad \mathrm{m^2/s} \tag{5-27}$$

, one can directly calculate the theoretical parabolic constants, and the results are presented in Table 5.11. A careful comparison of the theoretical (Table 5.11) and the experimental (Table 5.7) parabolic constants reveals that they both have the same magnitude, but the latter are somewhat larger that the former ones.

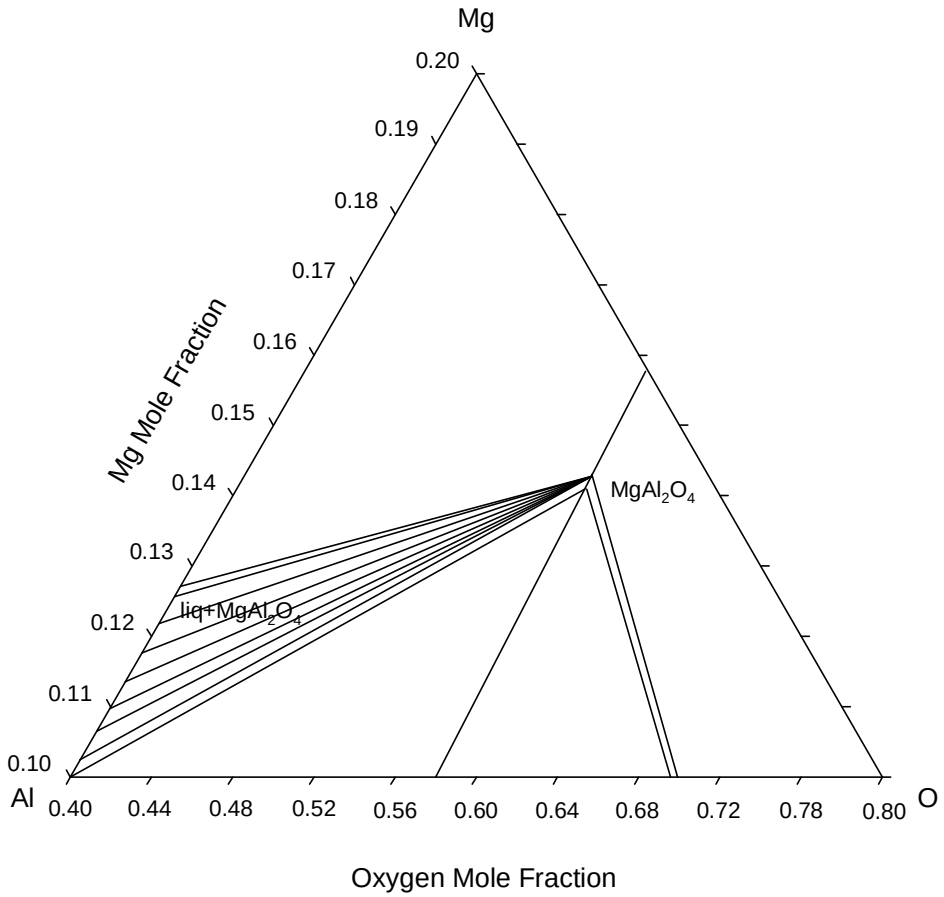

Fig. 5.47 The $MgAl_2O_4$ corner of the Mg-Al-O system at 1100°C

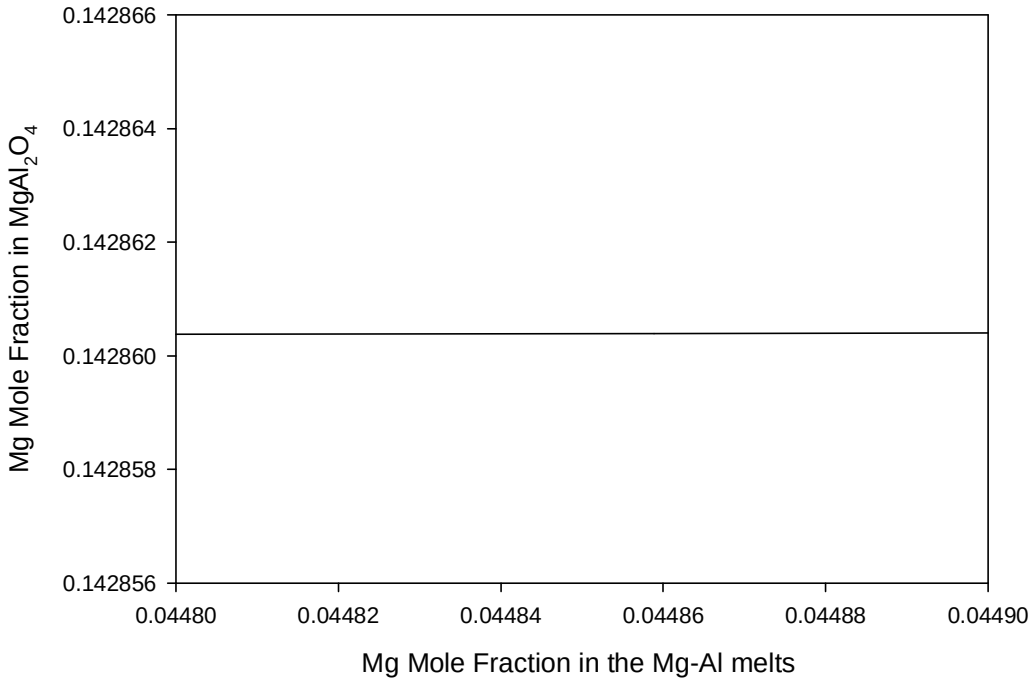

Fig. 5.48 The equilibrium relationship between Mg-Al melts and Spinel at 1000°C

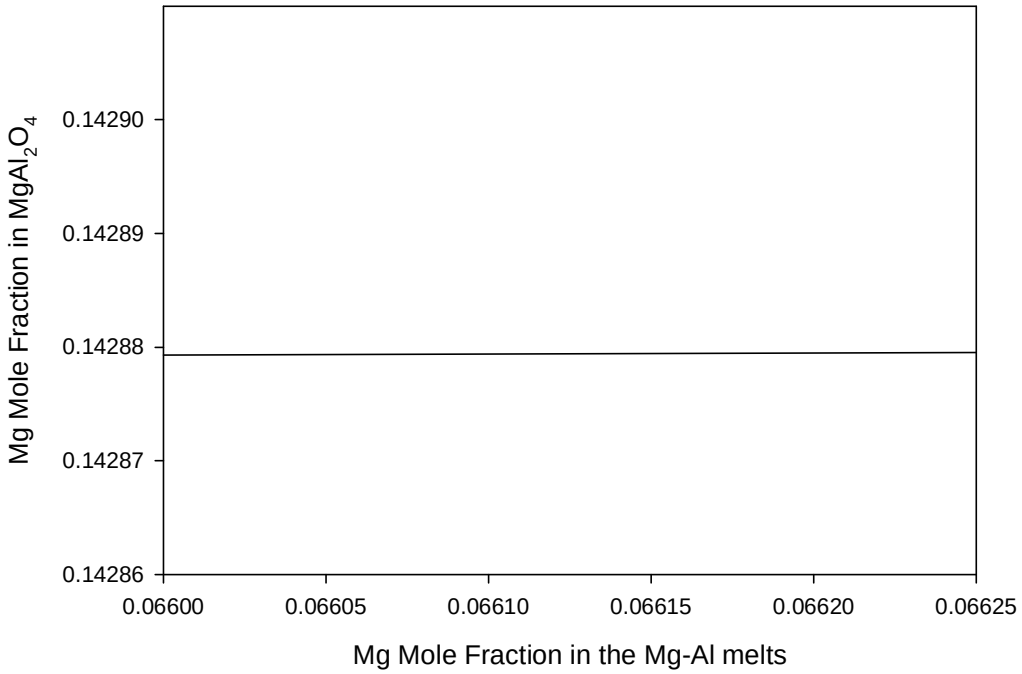

Fig 5.49 The equilibrium relationship between Mg-Al melts and Spinel at 1100°C

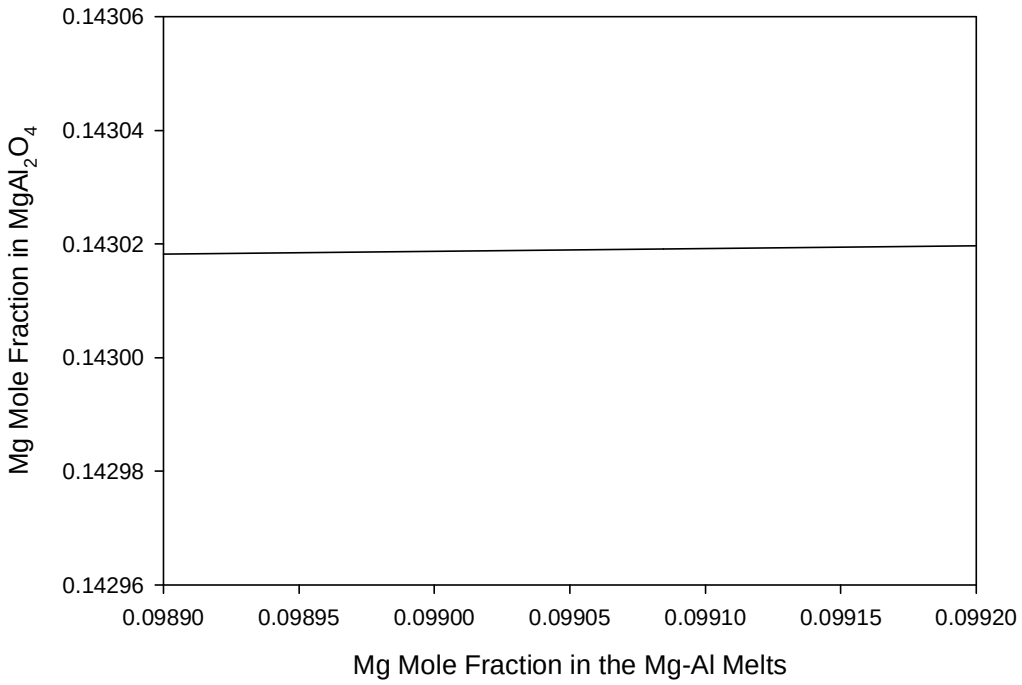

Fig 5.50 The equilibrium relationship between Mg-Al melts and Spinel at 1200°C

Table 5.11 The calculated theoretical parabolic constants at different temperatures

Temperature	C_{Mg}^{1}	C_{Mg}^{2}	k^{*}
1000°C	0.33334	0.33114	7.89e-18
1100°C	0.33340	0.32756	1.05e-16
1200°C	0.33359	0.31957	1.02e-15

From the above derivation and calculations, the parabolic constants obtained in the present study are found to be somewhat higher at 1000°C and 1100°C than these theoretical values. This may be caused by the difference in the experimental conditions. In the solid-solid reaction, the true contact area at the interface between MgO and $MgAl_2O_4$ is much smaller than the sample area due to the surface roughness. Even fine polishing cannot give a really smooth surface on the atomic scale. As for the solid-liquid reaction, the contact area at the interface is maximized due to the deformable nature of the Mg-Al melt. Consequently, the parabolic constants obtained in the current experiments are expected to be larger than the values predicted from the diffusion coefficients measured by solid-solid reactions.

In addition, grain boundary diffusion at 1000°C may play an important role, making the experimental parabolic constant much larger than the theoretical value predicted from lattice diffusion coefficient.

CHAPTER VI

THE INITIAL STAGE OF SPINEL FORMATION

6.1 Introduction

The growth of a new phase on a reactive substrate usually involves nucleation and growth. In addition, the reaction may include a coarsening stage when large particles grow at the expense of small ones to decrease the interfacial energy.

The interfacial energy and strain energy associated with the formation of critical nuclei act as barriers to nucleation. Both energies are generally functions of the nucleus shape. To find the nucleus with minimum energy, it is necessary to find the shape that minimizes the sum of these energies. Unlike the solid-solid transformation such as precipitation, the strain energy is generally present and plays an important role. For the current case where spinel is formed by the solid-liquid reaction, the nucleus shape is given by the Wulff's law with the interfacial energy dominating.

The formation of discrete spinel particles may be rate-limited by the rate at which atoms can be absorbed or emitted at the solid-liquid interface, thus making the transformation rate-limited by the interface reaction. On the other hand, the atomic transfer across the solid-liquid interface may be so fast that the concentrations in the adjoining phases at the solid-liquid interface are maintained in local equilibrium, making the transformation rate-limited by the diffusion in the system.

Although the kinetics for the spinel formation as discrete particles on the sapphire surface is of theoretical and practical importance, the preliminary study described in this

section was focused on the morphology and distribution of $MgAl_2O_4$ particles before a continuous $MgAl_2O_4$ layer was formed on the sapphire surface.

6.2 Experimental Procedure

The experimental procedure and sample preparation were the same as those used in Chapter V except the heating rate. In order to investigate the initial stage of $MgAl_2O_4$ formation, the assembly illustrated in Fig. 5.1 was initially placed at the top of the furnace. When the temperature of the furnace had reached the desired value, this assembly was then pushed smoothly and slowly into the isothermal zone of the vertical furnace in 20 minutes.

The experiments were conducted only at 1200°C for (0001) and $(01\bar{1}2)$ sapphire wafers. The reaction time ranged from 10 minutes to 2 hours. Upon reaction within a short time, $MgAl_2O_4$ was formed as discrete particles on the sapphire surface. To characterize sample morphology by SEM, the steel pipe assemble was taken out of the furnace and inverted quickly at 1200°C. The steel pipe was then cut by a handsaw to obtain the reacted samples. As mentioned before, the reacted samples were immersed in a 10 wt% NaOH aqueous solution to dissolve the residual alloy on the sample surface. The reacted samples were then coated with Au for SEM observation.

6.3 Results

The SEM images of reacted (0001) sapphire wafers are illustrated in Figs. 6.1-6.4 for different reaction times, and the results for reacted $(01\bar{1}2)$ sapphire wafers are presented in Figs. 6.5-6.8, respectively. Fig. 6.3 and Fig. 6.4 are from the same sample. Fig. 6.7 is from a reacted sample that was not totally immersed in the Mg-Al melts.

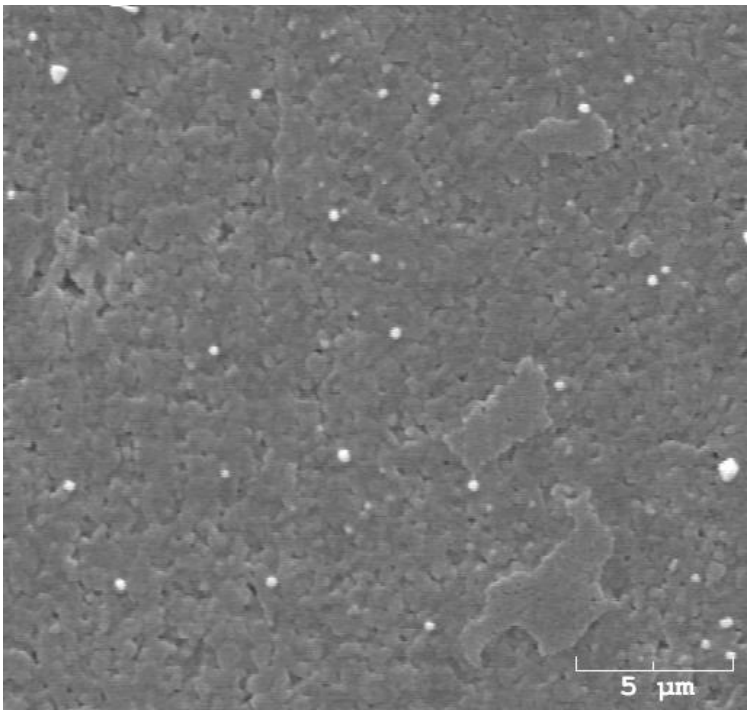

Fig. 6.1 $MgAl_2O_4$ nuclei on the (0001) sapphire wafer reacted at 1200°C for 10 minutes

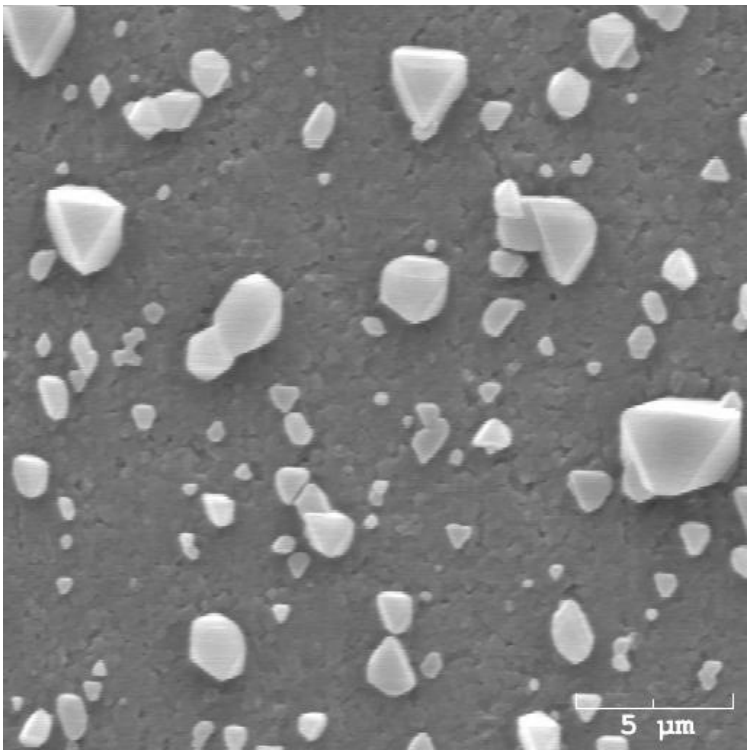

Fig. 6.2 $MgAl_2O_4$ particles on the (0001) sapphire wafer reacted at 1200°C for 30 minutes

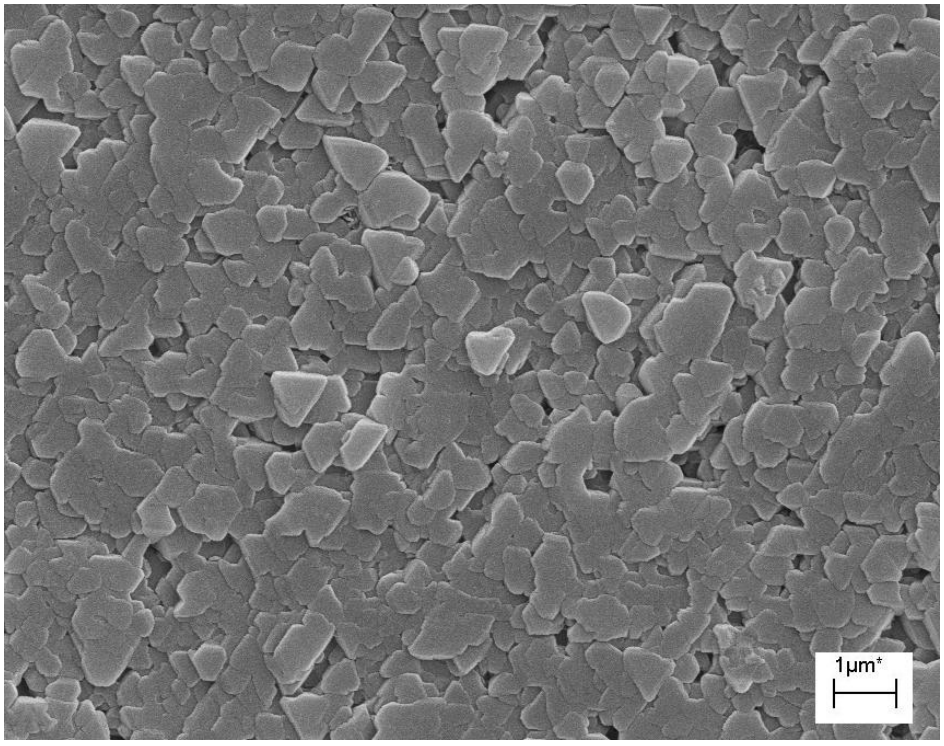

Fig. 6.3 $MgAl_2O_4$ particles on the (0001) sapphire wafer reacted at 1200°C for 90 minutes

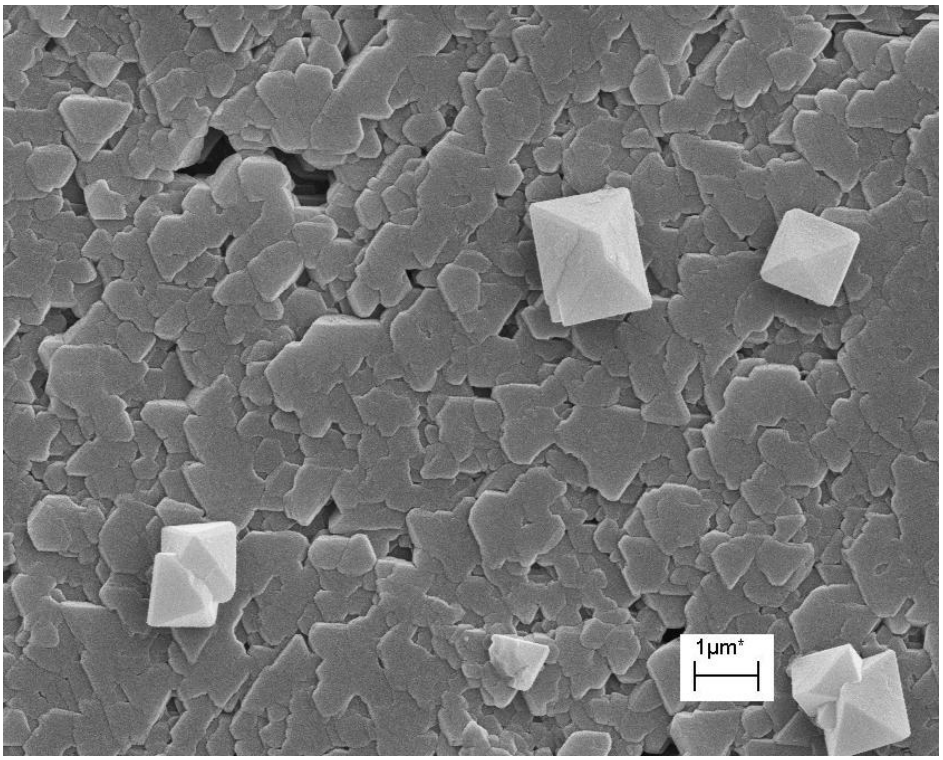

Fig. 6.4 $MgAl_2O_4$ particles on the (0001) sapphire wafer reacted at 1200°C for 90 minutes

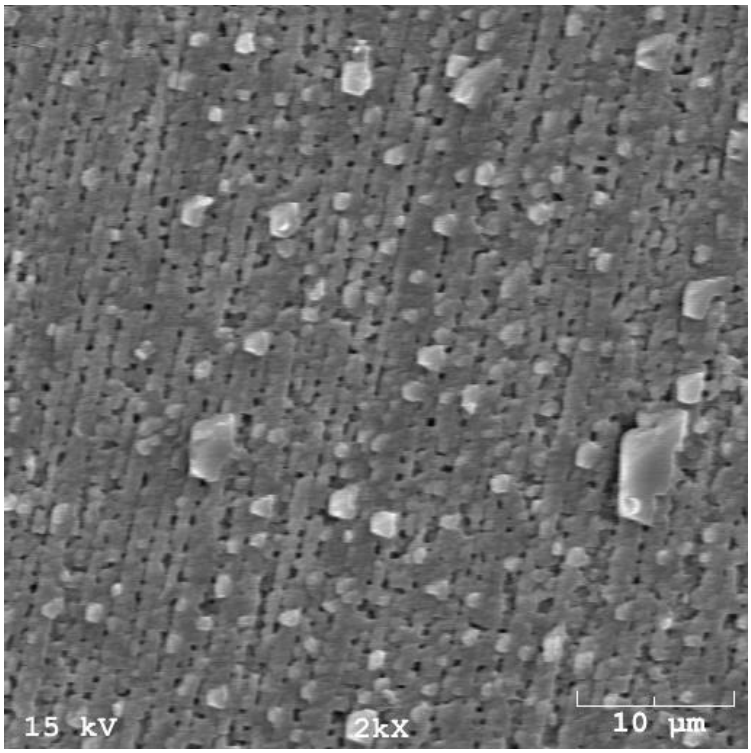

Fig. 6.5 $MgAl_2O_4$ nuclei on the $(01\bar{1}2)$ sapphire wafer reacted at 1200°C for 10 minutes

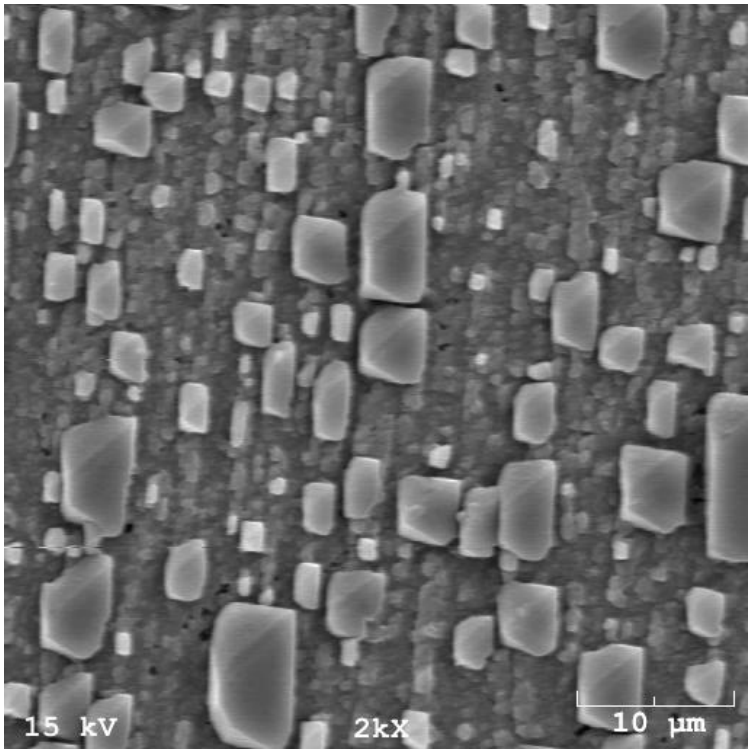

Fig. 6.6 $MgAl_2O_4$ particles on the $(01\bar{1}2)$ sapphire wafer reacted at 1200°C for 30 minutes

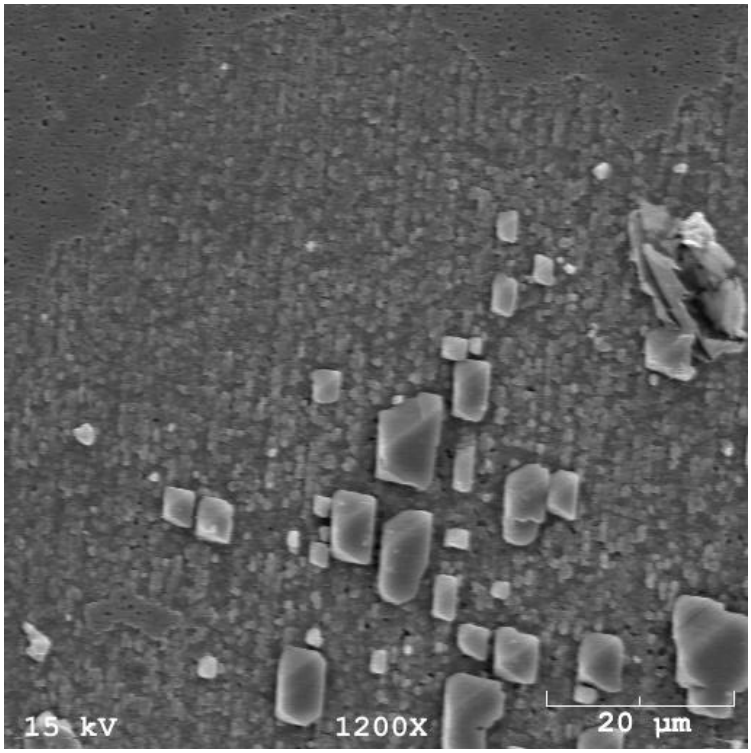

Fig. 6.7 $MgAl_2O_4$ particles on the $(01\bar{1}2)$ sapphire wafer reacted at 1200°C for 30 minutes

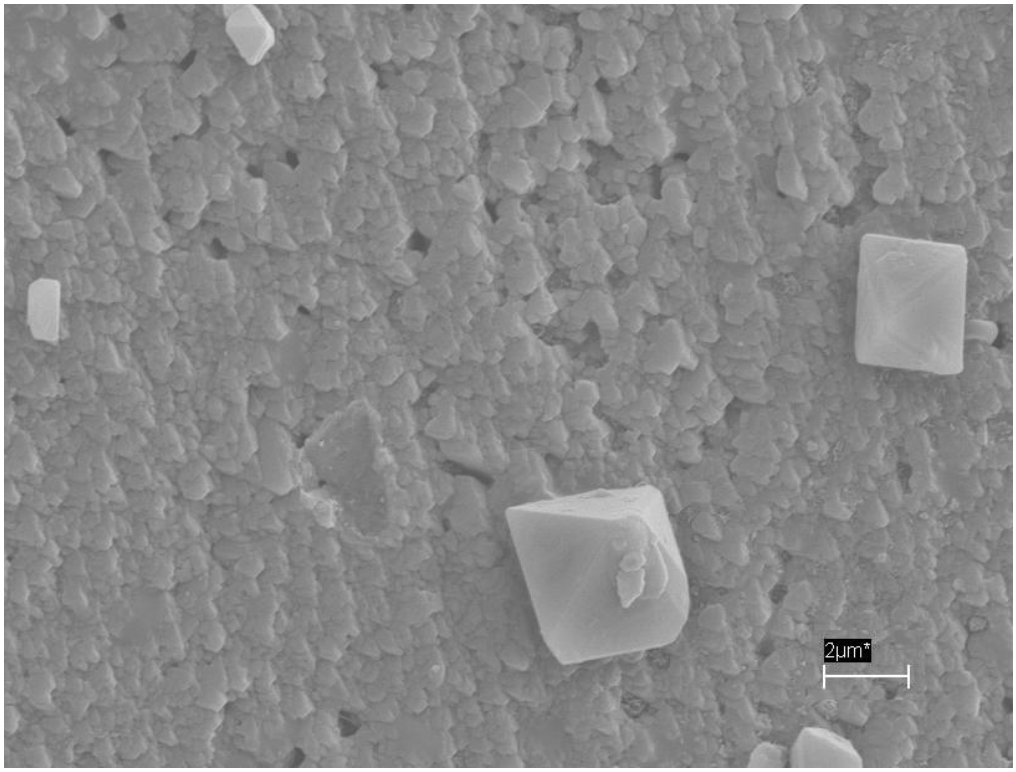

Fig. 6.8 $MgAl_2O_4$ particles on the $(01\bar{1}2)$ sapphire wafer reacted at 1200°C for 90 minutes

6.3 Discussion

If the surface energy of the reaction product is isotropic, then the surface energy is simply proportional to surface area, and the nuclei should have a spherical cap shape. However, when the surface energy is anisotropic, two additional degrees of freedom emerge which correspond to the two parameters required to specify surface orientations. Therefore, an anisotropic surface energy depends on spatial orientations, and therefore it can decrease by developing in the low energy directions, which leads to faceted surfaces.

For the spinel growth on a (0001) sapphire wafer, as seen in Fig. 6.1, the nuclei decorated the sapphire surface at a very low coverage. At a higher coverage, as shown in Fig. 6.2, spinel particles with triangular {111} faces parallel to the substrate (0001) surface were observed with a certain size distribution. The product shape was consistent with a tetrahedron composed of {111} faces. The SEM results indicated that the {0001} planes of sapphire were parallel to the {111} planes of spinel, which is consistent with the following orientation relationship in the literature for the spinel formation between Al_2O_3 and MgO.

$$\{0001\}_{sapphire} // \{111\}_{spinel}$$

$$<10\bar{1}0>_{sapphire} // <1\bar{1}0>_{spinel}$$

The rims of the triangles were aligned with the closed-packed directions in spinel parallel to the closed-packed directions in sapphire. The SEM images illustrating the reacted samples with the surface almost covered by spinel are also presented in Fig. 6.3, where triangular surfaces with the threefold symmetry could be clearly seen. Although tetrahedron-shaped spinel was the main product, some octahedron-shaped spinel could also be observed, as shown in Fig. 6.4.

The surface morphology of spinel on $(01\bar{1}2)$ sapphire substrates was more complicated because the substrate surface is not the closed-packed plane. To maintain the orientation relationship that the closed-packed planes in sapphire should be parallel to the close-packed planes in spinel, triangular {111} surfaces in spinel had to be inclined at a certain angle to the substrate, as seen from Figs. 6.5 and 6.6. The direction of the stripes in these two figures is believed to be the closed-packed directions in sapphire, namely $<10\bar{1}0>$. To exclude the possibility that those stripes were caused by corrosion in NaOH aqueous solution, a SEM image illustrating the boundary between reacted and unreacted zones is shown in Fig. 6.7. The SEM morphology of a reacted $(01\bar{1}2)$ sapphire wafer with the surface almost covered by $MgAl_2O_4$ is shown in Fig. 6.8, where the texture of aligned products and some big octahedron-shaped spinel particles can be clearly seen.

APPENDIX 1

SAPPHIRE WAFER PREPARATION

Sapphire is an ideal material because of its excellent optical and mechanical properties. However, the desirable properties of sapphire also make it difficult to grind and polish. In this section, a procedure is proposed to lap and polish sapphire wafers.

Sample Cutting:

Sapphire, received in the form of rods with 1 inch OD and 3 inch length, was first subjected to cutting by a diamond saw. The diamond saw cut sapphire with an abrasive action that cleaved, chipped and shattered the material, leaving small cracks on the material surface. The wafers obtained should have a sufficient thickness for the subsequent grinding and flattening to remove these cracks and the finial fine polishing. Accordingly, the sapphire wafer cut by the diamond saw should have a dimension of about 1.5mm thick, 15 mm long, and 8mm wide.

Sample Grinding and Flattening:

Grinding and flattening of the wafers cut by the diamond saw was carried out on a series of diamond grinding disks with the particle size ranging from 110 to 30 microns (His Glassworks Inc, NC). These disks, which can provide a roughly flat surface, were selected for aggressive removal of wafer material. The removal rate depends on the pressure applied and the rotation rate of the grinding machine.

A piece of double-side sticky tape was initially put on a piece of rectangular Al Alloy (40mm-10mm-10mm), and then one piece of roughly-polished sapphire wafer was carefully placed on the tape. The subsequent grinding and flattening was performed by

hand on a grinding wheel to eliminate the uneven areas of the sapphire surface. The grinding disks were used from the coarse diamond size to the small one. Water served as lubricant to cool the sample being polished in this study. Once one side was ground, the sapphire wafer was taken out by putting the whole assembly into acetone. The other side of the sapphire wafer was ground in the same way. When the two surfaces were relatively flat (5-micron deviation), the wafer, about 0.8mm thick, 15 mm long, and 8mm wide, was left undergo the following fine polishing.

Sample Polishing:

The preparation of sapphire wafer with a uniform thickness is very important because the sample thickness should be examined as a function of position and time. The sapphire wafer cut by a diamond saw was around 1.5 mm thick. After grinding and flattening, the thickness was reduced to 0.8 mm. There was still 0.3 mm to be removed by fine polishing by which two relative parallel surfaces were obtained.

The schematic drawing to illustrate the preparation of epoxy holder for the fine polishing is shown in Fig. a-1. In order to get a flat surface for the sample holder, three small pieces of glass (10mm-30mm-1mm) were put on a larger piece of glass, and then a piece of plastic tube (60mm OD) was placed on the large glass to hold epoxy (Leco Corporation, Stock Number 811-189). The connection part between the plastic tube and glass was sealed by glue to prevent the epoxy from leaking. A suitable amount of epoxy with catalyst was poured into this assembly. After cold-curing at room temperature, the epoxy holder with three small pieces of glass inside was separated from the plastic tube and the larger piece of glass.

To get a well-controlled sapphire surface, the crystal bond or glue, which was used to fix sapphire wafers during polishing procedure, could not be applied directly on the three small pieces of glass. A small portion of epoxy between two adjoining pieces of glass was removed to make room for crystal bond or glue, as shown in Fig. a-2. Under this condition, the error introduced by the non-uniform thickness of crystal bond or glue could be avoided.

The schematic drawing to show the arrangement of sapphire wafers on the epoxy holder is shown in Fig. a-3, where two small pieces of glass were used to increase contact surface. Diamond pastes with the particle size ranging from 10 microns to 0.5 microns were used, and the polishing cloth was from Leco Corporation with the stock number 812-351. During the fine polishing process, sapphire wafers were removed and cleaned by acetone frequently so that their thickness could be measured by micrometers.

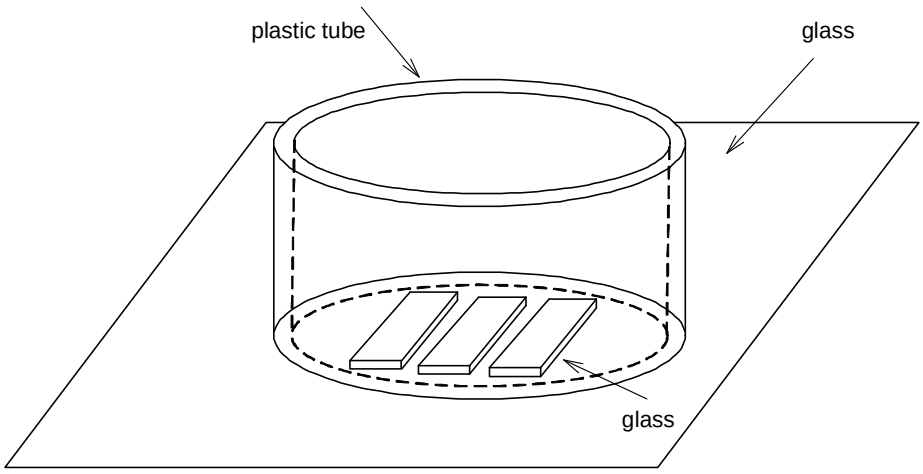

Fig. a1-1 The schematic drawing for the preparation of epoxy holder

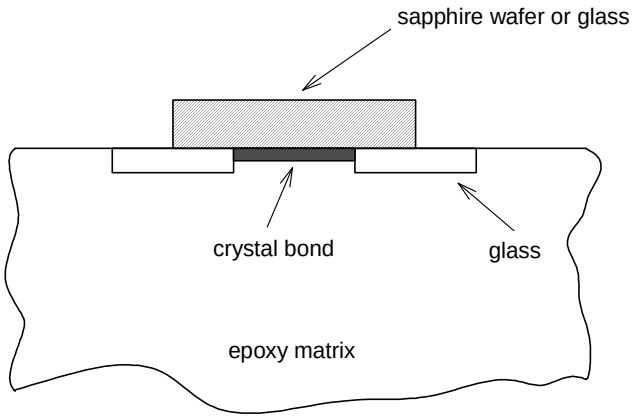

Fig. a1-2 The enlarged illustration to show the position of crystal bond

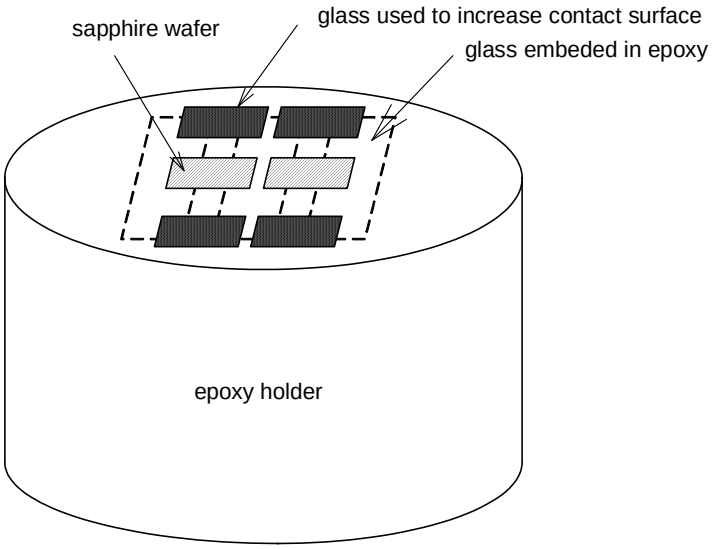

Fig. a1-3 The arrangement of sapphire wafers and glass on the surface of the epoxy holder

APPENDIX 2

PHASE EQUILIBIRUM CALCULATION

Consider a closed system where there is no work involved other than that related to volume change. The determination of chemical equilibrium in such a system at constant temperature T and pressure P is equivalent to finding the global minimum of the total Gibbs free energy G:

$$G = \sum_{i=1}^{N} f_i G_i$$

where N is the number of phases in the system, f_i, which must be nonnegative, is the number of moles of the ith phase, and G_i is the Gibbs free energy of the ith phase. The whole system must be subjected to the constraints of mass conservation.

More specifically, for the Al-Mg-O system containing liquid, spinel, MgO, Al_2O_3 and O_2, the Gibbs free energy of the whole system can be written as:

$$G=f_{Al_2O_3}\cdot G_{Al_2O_3}+f_{MgO}\cdot G_{MgO}+f_{spinel}\cdot G_{spinel}+f_{liquid}\cdot G_{liquid}+f_{O_2}\cdot G_{O2}$$

The constraints imposed by mass conservation can be written as:

$$f_{Al_2O_3}\cdot 2+f_{MgO}\cdot 0+f_{spinel}\cdot(yat\cdot 1+yao\cdot 2)+f_{liquid}\cdot p\cdot ya+f_{O_2}\cdot 0=n_{Al}$$

$$f_{Al_2O_3}\cdot 0+f_{MgO}\cdot 1+f_{spinel}\cdot(ymt\cdot 1+ymo\cdot 2+ymi\cdot 2)+f_{liquid}\cdot p\cdot ym+f_{O_2}\cdot 0=n_{Mg}$$

$$f_{Al_2O_3}\cdot 3+f_{MgO}\cdot 1+f_{spinel}\cdot 4+f_{liquid}\cdot q\cdot yo+f_{O_2}\cdot 2=n_{O}$$

where n_{Al}, n_{Mg} and n_O are the total molar amount of Al, Mg and O, yat is the site fraction of Al^{+3} on the tetragonal sublattice in spinel, yao and ymo are the site fraction of

Al^{+3} and Mg^{+2} on the octahedral sublattice in spinel, ya, ym and yo are the site fraction of Al^{+3}, Mg^{+2} and O^{2-} on the cation and anion sublattice of the melt, respectively.

The Gibbs free energy for the spinel phase has already been introduced in Chapter II. As mentioned before, the formula for the melt can be written as:

$$(Al^{+3}, Mg^{+2})_p (O^{-2}, Va^{-q})_q$$

The Gibbs free energy function is then given as:

$$\begin{aligned}
&G_{spinel} = y_{Al^{+3}} y_{O^{2-}} G_{Al_2O_3} + y_{Mg^{+2}} y_{O^{2-}} G_{Mg_2O_2} + q \cdot (y_{Al^{+3}} y_{Va} G_{Al} + y_{Mg^{+2}} y_{Va} G_{Mg}) \\
&+PRT \cdot (y_{Al^{+3}} \ln y_{Al^{+3}} + y_{Mg^{+2}} \ln y_{Mg^{+2}}) \\
&+qRT \cdot (y_{O^{2-}} \ln y_{O^{2-}} + y_{Va} \ln y_{Va}) \\
&+\mathrm{q} \cdot \mathrm{y}_{\mathrm{Va}}{}^{2} \cdot \mathrm{y}_{\mathrm{Al}^{+3}} \cdot \mathrm{y}_{\mathrm{Mg}^{+2}} \cdot (-11200+9.578 \cdot \mathrm{T}) \\
&+\mathrm{y}_{\mathrm{va}} \cdot \mathrm{y}_{\mathrm{Al}^{+3}} \cdot y_{O^{2-}} \cdot (171042+106*\mathrm{T}) \\
&+\mathrm{y}_{\mathrm{va}} \cdot \mathrm{y}_{\mathrm{Mg}^{+2}} \cdot y_{O^{2-}} \cdot (182000+26.8*\mathrm{T})
\end{aligned}$$

where $G_{Al_2O_3}$, $G_{Mg_2O_2}$, G_{Al}, and G_{Mg} are the Gibbs free energy for Al_2O_3, Mg_2O_2, Al and Mg in the liquid state, respectively.

The Gibbs free energy minimization for the whole system was performed with the optimization toolbox in Matlab. Some user-defined functions were made for providing the Gibbs free energy of each phase. The script written to call the fmincon function for the constrained optimization was also used. The matlab codes used are presented below.

% The Gibbs free energy of spinel as a function of composition and temperature

```
function G=Gspinel(yat,yao,ymo,ymi,T)
ymt=1-yat;
yvo=1-yao-ymo;
yvi=1-ymi;
P=1e5;
R=8.31451;
GCORUND=-1724886.06+754.856573*T-116.258*T*log(T)-
0.0072257*T^2+2.78532E-07*T^3+2120700*T^(-1);
GPERICLA=-619428.502+298.253571*T-47.4817*T*log(T)-
0.00232681*T^2+4.5043E-8*T^3+516900*T^(-1);
GGAMMA=-1708389.72+791.591946*T-121.754*T*log(T)-
0.0075467*T^2+2.89573E-7*T^3+2222750*T^(-1);
NSPINEL=GPERICLA+GCORUND-27600-62*T+9*T*log(T);
MSPINEL=GPERICLA+58000-18*T;
ISPINEL=NSPINEL+51600-39*T;
REC=108000;
GAAV=0;
GMAV=NSPINEL;
GAMV=2*ISPINEL+23.05130263670154*T;
GAVV=8*GGAMMA+44.95159068617350*T;
GMVV=8*GGAMMA+NSPINEL+44.95159068617350*T+REC;
GMMV=NSPINEL+2*ISPINEL+23.05130263670154*T;
GMMM=8*MSPINEL-NSPINEL-2*ISPINEL;
GMAM=8*MSPINEL-NSPINEL-4*ISPINEL-23.05130263670154*T;
GMVM=8*GGAMMA+8*MSPINEL-NSPINEL-4*ISPINEL+21.90028804947196*T+REC;
GAAM=8*MSPINEL-2*NSPINEL-4*ISPINEL-23.05130263670154*T;
GAVM=8*GGAMMA+8*MSPINEL-2*NSPINEL-4*ISPINEL+21.90028804947196*T;
GAMM=8*MSPINEL-2*NSPINEL-2*ISPINEL;
G=ymt*ymo*yvi*GMMV+ymt*ymo*ymi*GMMM+ymt*yao*yvi*GMAV+ymt*yao*ymi*GMAM+y
mt*yvo*yvi*GMVV+ymt*yvo*ymi*GMVM+yat*ymo*yvi*GAMV+yat*ymo*ymi*GAMM+yat*
yao*yvi*GAAV+yat*yao*ymi*GAAM+yat*yvo*yvi*GAVV+yat*yvo*ymi*GAVM+R*T*(ym
t*log(ymt)+yat*log(yat)+2*(ymo*log(ymo)+yao*log(yao)+yvo*log(yvo)+yvi*l
og(yvi)+ymi*log(ymi)));
```

% The Gibbs free energy of liquid as a function of composition and temperature

```
function G=Gliquid(ya,yo,T)
ym=1-ya;
yv=1-yo;
R=8.31451;
gal2o3=-1625385.57+712.394972*T-116.258*T*log(T)-
0.0072257*T^2+2.78532*10^(-7)*T^3+2120700*T^(-1);
gmgo=-549098.33+275.72463*T-47.4817*T*log(T)-
0.00232681*T^2+4.5043*10^(-8)*T^3+516900*T^(-1);
gal=-795.996+177.430178*T-31.748192*T*log(T);
gmg=-5439.869+195.324057*T-34.3088*T*log(T);
q=3*ya+2*ym;
p=2*yo+q*yv;
s1=R*T*(ya*log(ya)+ym*log(ym));
s2=R*T*(yo*log(yo)+yv*log(yv));
ge=q*yv^2*ya*ym*(-
11200+9.578*T)+yv*ya*yo*(171042+106*T)+yv*ym*yo*(182000+26.8*T);
gref=ya*yo*gal2o3+ym*yo*2*gmgo+q*yv*ya*gal+q*yv*ym*gmg;
G=gref+p*s1+q*s2+ge;
```

% The Gibbs free energy of MgO as a function of temperature

```
function G=GMgO(T)
R=8.31451;
G=-619428.502+298.253571*T-47.4817*T*log(T)-0.00232681*T^2+4.5043E-
8*T^3+516900*T^(-1);
```

% The Gibbs free energy of Al_2O_3 as a function of temperature

```
function G=GAl2O3(T)
R=8.31451;
G=-1724886.06+754.856573*T-116.258*T*log(T)-0.0072257*T^2+2.78532E-
07*T^3+2120700*T^(-1);
```

% The Gibbs free energy of O_2 as a function of temperature

```
function G=GO2(T)
R=8.31451;
GO=-6568.763+12.659879*T-16.8138*T*log(T)-0.5957975E-3*T^2+0.006781E-
6*T^3+262905*T^(-1);
G=2*GO;
```

% The Gibbs free energy of the whole system to be optimized

```
function G=mysystem(x)
yat=x(1);
yao=x(2);
ymo=x(3);
ymi=x(4);
ya=x(5);
yo=x(6);
f_Al2O3=x(7);
f_MgO=x(8);
f_spinel=x(9);
f_liquid=x(10);
f_O2=x(11);
T=1200;
G=f_Al2O3*GAl2O3(T)+f_MgO*GMgO(T)+f_spinel*Gspinel(yat,yao,ymo,ymi,T)+f
_liquid*Gliquid(ya,yo,T)+f_O2*GO2(T);
```

% The constraints imposed by the mass conservation
(nAl, nMg, and nO are the molar amount of each element in the system, and these values can be changed to calculate equilibrium at other compositon points)

```
function [c,ceq]=myconstraint(x)
nAl=0.2;
nMg=0.6;
nO=0.2;
yat=x(1);
yao=x(2);
ymo=x(3);
ymi=x(4);
ya=x(5);
yo=x(6);
f_Al2O3=x(7);
f_MgO=x(8);
f_spinel=x(9);
f_liquid=x(10);
f_O2=x(11);
ym=1-ya;
yv=1-yo;
ymt=1-yat;
q=3*ya+2*ym;
p=2*yo+q*yv;
T=1200;
ceq(1)=f_Al2O3*2+f_MgO*0+f_spinel*(yat*1+yao*2)+f_liquid*p*ya+f_O2*0-
nAl;
ceq(2)=f_Al2O3*0+f_MgO*1+f_spinel*(ymt*1+ymo*2+ymi*2)+f_liquid*p*ym+f_O
2*0-nMg;
ceq(3)=f_Al2O3*3+f_MgO*1+f_spinel*4+f_liquid*q*yo+f_O2*2-nO;
c=[];
```

%Matlab Script used to perform constrained optimization

```
x0=[0.2,0.2,0.2,0.2,0.2,0.2,0.2,0,0.2,0,0.2]+eps;
lb=[0,0,0,0,0,0,0,0,0,0,0]+eps;
ub=[1,1,1,1,1,1,0,10,0,10,0]+eps;
options=optimset('largescale','off','MaxFunEvals',200000,'MaxIter',2000
0,'display','iter','tolx',1e-20,'tolfun',1e-10);
[x,fval,exitflag,output]=fmincon(@mysystem,x0,[],[],[],[],lb,ub,@mycons
traint,options)
```

REFERENCES

[1]K. Sandhage, Mechanism of Incongruent Reduction (Proposal), 2001

[2]C. Wagner, Corro. Sci. 1965, 5, 751-764

[3]E. T. Turkdogan, P. Grieveson, L. S. Darken, J. Phys. Chem. 1963, 67, 1647-1649

[4]M. J. McNallan, W. W. Liang, J. Am. Ceram. Soc. 1981, 64(5), 302-307

[5]Y. Oishi, A. R. Cooper, W. D. Kingery, J. Am. Ceram. Soc. 1965, 48, 88-92

[6]K. Sandhage, G. J. Yuerk, J. Am. Ceram. Soc. 1988, 71(6),478-489

[7]P. Kumar, S. A. Dregia, K. Sandhage, J. Mater. Res. 1999, 14(8), 3312-3318

[8]C. A. Eckert, R. B. Irwin, C. W. Graves, Ind. Eng. Chem. Process Dev. 1984, 23, 210-217

[9]A. K. Kaw, Mechanics of Composite Materials, CRC press, 1997, 2-49

[10]I. Lemay, Principles of Mechanical Metallurgy, Elsevier North-Holland, 1981, 215-236

[11]S. Schicker, J. Am. Ceram. Soc. 1997, 80(9), 2294-2300

[12]W. G. Fahrenholtz, J. Am. Cerac. Soc. 1996, 79(9), 2497-2499

[13]M. Dickson, B. Snyder, K. Sandhage, J. Am. Ceram. Soc. 2002, 85(3), 730-732

[14] K. A. Rogers, K. Sandhage, J. Am. Ceram. Soc. 1999, 82(3), 757-760

[15]R. E. Loehman, K. Eqsuk, J. Am. Ceram. Soc. 1996, 79(1), 27-32

[16]P. Kumar, K. Sandhage, J. Am. Ceram. Soc. 1999, 34(23), 5757-5769

[17] S. Kramp, M. Febri, J. C. Joubert, J. Solid State chem. 1997, 133, 145-151

[18]M. Dickson, R. Snyder, K. Sandhage, J. Am, Ceram. Soc. 2002, 85(3),730-732

[19]G. Zbigniew, M. Dickson, K. Sandhage, J. Mat. Res. 2003, 18(9), 2135-2140

[20] N. N. Greenwood, Ionic Crystals Lattice Defects and Nonstoichiometry, Butterworths, 1968, 92-97

[21] G. S. Rohrer, Structure and Bonding in Crystalline Materials, Cambridge University Press, 2001, 162-169

[22] F. R. Nabarro, Dislocations in Solids, North-Holland, 1996, 405-407

[23]A. Kelly, Crystallography and Crystal Defects, John Wiley & Sons, 2000, 112-113

[24] R. E. Carter, J. Am. Ceram. Soc. 1961, 44(3), 116-120

[25] D. Hess, Inter. Sci. 1994, 2, 221-237

[26] E. Bruce, Geochi. Cosmochi. Acta. 2002, 66(12), 2123-2138

[27] D. W. Susnitzky, Script. Metall. 1988, 22, 1149-1154

[28] B. K. Kad, Mat. Res. Soc. Symp. Proc. 1994, 319, 331-315

[29] C. B. Carter, Phil. Mag. A, 1985, 52(2), 207-224

[30] Y. K. Simpson, C. B. Carter, Proc. of the 45th annual meeting of the electron microscop society of American, 1987, 294-295

[31] D. X. Li, P. Pirouz, A. H. Heuer, Phil. Mag. A, 1992, 65(2), 403-425

[32] B. Hallstedt, Calphad, 1993, 17(3), 281-286

[33] K. Fitzner, Thermochi. Acta. 1982, 52, 103-105

[34] M. Hillert, Metall. Trans. A, 1985, 16A, 261-264

[35] J. R. Taylor, Calphad, 1992, 16(2), 173-179

[36] M. Hansen, K. Anderko, Constitution of Binary Alloys, McGraw-Hill, 1958

[37] S. Otsuka, Z. Kozuka, Trans. Japan. Inst. Met. 1981, 22(8), 558-566

[38] J. Murry, Bull. Alloy Phase Dia. 1982, 3(1), 60-73

[39] D. Ludecke, K. Hack, Z. Metallkde, 1985, 20, 145-151

[40] N. Saunders, Calphad, 1990, 14(1), 61-70

[41] Y. Zuo, Y. A. Chang, Calphad, 1993, 17(2), 161-174

[42] Z. Moser, J. Phase Equilib. 1998, 19(1), 38-47

[43] B. Tiwari, Metall. Trans. 1987, 18A, 1645-1651

[44] G. R. Belton, Y. K. Rao, Trans. Metall. Soci. AIME, 1969, 245, 2189-2193

[45] Y. J. Bhatt, S. P. Garg, Metall. Trans. B, 1976, 7B, 271-275

[46] B. Hallstedt, J. Am. Ceram. Soc. 1992, 75(6), 1497-1507

[47] M. Avrami, J. Chem. Phys. 1939, 7, 1103-1107

[48] M. Avrami, J. Chem. Phys. 1941, 9,177-180

[49] M. Avrami, J. Chem. Phys. 1940, 8, 212-216

[50] J. W. Christian, The Theory of Transformations in Metals and Alloys, Pergamon, 1981

[51] M. C. Weinberg, J. Non-Crystalline Solids, 1997, 219, 89-99

[52] K. A. Jackson, Kinetic Processes, John Wiley & Son, 2004

[53] V. Erukhimovitch, J. Baram, Physical Review B, 1995, 51, 6221-6230

[54] M. T. Todinov, Acta Mater. 1996, 44(12), 4697-4703

[55] M. T. Todinov, Acta Mater. 2000, 48, 4217-4224

[56] G. Carter, Phil. Mag. A, 1999, 79(11), 2773-2784

[57] M. J. Starink, A. M. Zahra, Thermochi. Acta. 1997, 292, 159-168

[58] O. Kayacan, H. Cetinel, Physica A, 2005, 348, 223-235

[59] J. Malek, Thermochi. Acta. 1995, 267, 61-73

[60] S. S. Sahay, K. Krishnan, Physica B, 2004, 348, 310-316

[61] G. Carter, Vacuum, 1999, 53, 389-397

[62] E. B. Naim, P. L. Krapivsky, Physical Review E, 1996, 54(4), 3562-3568

[63] M. J. Starink, J. Mat. Sci. 2001, 36, 4433-4441

[64] M. J. Starink, J. Mat. Sci. 1997, 32, 4061-4070

[65] M. J. Starink, A. M. Zahra, Phil. Mag. A, 1998, 77(1), 187-199

[66] M. J. Starink, P. Wang, Acta Mater. 1999, 47(14), 3841-3853

[67] M. J. Starink, A. M. Zahra, Acta Mater. 1998, 46(10), 3381-3397

[68] D. Hess, Appl. Phys. 1993, A57, 415-425

[69] V. I. Dybkov, Growth Kinetics of Chemical Compound Layers, Cambridge International Science Publishing, 1997, 20-22

[70] V. I. Dybkov, Defect and diffusion forum, 2001, 194-199, 1503-1522

[71] P. G. Kotula, C. B. Cater, Physical Review Letters, 77(16), 3367-3370

[72] Y. Kouh, J. Am. Ceram. Soc. 1987, 70(7), C-149-151

[73] R. W. Balluffi, Kinetics of Materials, John Willey & Son, 2005

[74] F. S. Pettie, J. Am. Ceram. Soc. 1966, 49(4), 199-203

[75] W. J. Minford, V. S. Stubican, J. Am. Ceram. Soc. 1974, 57(80), 363-376

[76] L. Navas, J. Am. Ceram. Soc. 1961, 44(9), 434-446

[77] R. C. Rossi, R. M. Fulrath, J. Am. Ceram. Soc. 1963, 46(3), 145-149

[78] P. G. Kotula, C. B. Carter, J. Am . Ceram. Soc. 1998, 81(11), 2877-2884

[79] K. H. Prakash, T. Sritharan, Acta Mater. 2001, 49, 2481-2489

[80] V. N. Yermenko, Y. V. Natanzon, V. I. Dybkov, J. Mat. Sci. 1981, 16, 1748-1756

[81] N. Tunca, R. W. Smith, Metal. Trans. A, 1989, 20A, 825-836

[82] C. R. Thornber, J. S. Huebner, Am. Mineralogist, 1985, 70, 934-945

[83] R. Zhang, Q. Cao, Sci. Tech. Adv. Mater. 2001, 2, 3-5

[84] Y. Zhang, D. Walker, C. E. Lesher, Contrib. Mineral. Petrol. 1989, 102, 492-513

[85] B. N. Samaddar, W. D. Kingery, A. R. Cooper, J. Am. Ceram. Soc. 1964, 47(5), 249-254

[86] K. H. Sandhage, G. J. Yurek, J. Am. Ceram. Soc. 1990, 73(12), 3633-3642

[87] K. Bouche, F. barbier, A. Coulet, Mat. Sci. Eng. 1998, A249, 167-175

[88] H. R. Shahverdi, J. Mat. Sci. 2002, 37, 1061-1066

[89] F. J. Higuera, P. D. Weidman, J. Fluid Mech. 1998, 361, 25-39

[90] I. G. Hwang, C. K. Choi, J. Crystal Growth, 1996, 162, 182-189

[91] M. Sheintuch, Y. Smagina, O. Nekhamkina, Ind. Eng. Chem. Res. 2002, 41, 2136-2146

[92] M. Rahman, I. Mulodani, Theoret. Comput. Fluid Dynamics, 2000, 13, 291-304

[93] P. Ganesan, H. P. rani, Chem. Eng. Proc. 2000, 39, 93-105

[94] J. K. Basird, L. Guo, J. Chem. Phys. 1998, 109(6), 8-12

[95] G. H. Kaiura, J. M. Toguri, Metall. Trans. B, 1979, 10(B), 595-605

[96] C. Kleinstreuer, Engineering Fluid Dynamics, Cambridge University Press, 1997

[97] C. Wagner, J. Phys Colloid. Chem. 1949, 53, 1030-1033

[98] L. C. Burmeister, Convective Heat Transfer, Wiley-Interscience, 1993

[99] S. Kaka, W. Aung, R. Viskanata, Natural Convection: Fundamentals and Applications, Hemisphere Pub, 1985

[100] S. Pushpavanam, R. Narayanan, Int. J. Heat Mass Transfer, 1990, 33(9), 2056-2059

[101]H. Jynge, K. Motzfeldt, Electrochi. Acta. 1980, 25, 139-143

[102]B. Hallstedt, Mat. Sci. Eng. 1990, A129, 135-145

[103]E. Saiz, A. P. Tomsai, J. Am. Ceram. Soc. 1998, 81(9), 2381-2393

[104]K. J. Brondyke, J. Am. Ceram. Soc. 1953, 36(5), 171-174

[105]A. E. Standage, M. S. Gani, J. Am. Ceram. Soc, 1967, 50(2), 101-105

[106]V. Gabis, Key Eng. Mater. 1997, 132-136, 1653-1656

[107]S. Dhara, R. K. Kamboj, Bull. Mater. Sci. 2002, 25(6), 565-568

[108]F. Hodaj, Defect and Diffusion Forum, 2001, 194-199, 1599-1606

[109] D. A. Weirauch, J. Mater. Res. 1988, 3(4), 729-739

[110] R. Carter, J. Am. Ceram. Soc. 1961, 44(4), 116-120

[111] A. Schneider, G. Inden, Acta Mater. 2005, 53, 519-531

[112] Y Chiang, K. W. David, J. Am. Ceram. Soc. 1989, 72(2), 271-277

[113] P. Erich, Z. Metallkde. 1940, 32, 7-9

[114] I. Barin, Thermochemical Data of Pure Substances, Wiley-VCH Verlag GmbH, 1989

[115] Y. Du, Mat. Sci. Eng. A, 2003, 363, 140-151

[116] R. C. Rossi, R. M. Fulrath, J. Am. Ceram. Soc. 1963, 46(3), 145-149

[117] R. Hempelmann, Diffusion in Solids, Oxford University Press, 2000